

This is to certify that the

dissertation entitled

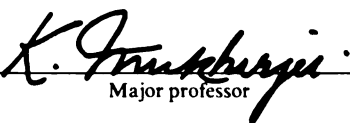
STRUCTURE AND PROPERTY CHANGES IN METGLAS® 2605SC
INDUCED BY PULSE LASER INTERACTION.

presented by

Chandrashekhar G. Wakade

has been accepted towards fulfillment
of the requirements for

Doctor of Philosophy degree in Materials Science.


Major professor

Date June 27, 1985



RETURNING MATERIALS:
Place in book drop to
remove this checkout from
your record. FINES will
be charged if book is
returned after the date
stamped below.

--	--	--

STRUCTURE AND PROPERTY CHANGES IN METGLAS® 2605SC INDUCED BY PULSE
LASER INTERACTION

BY

Chandrashekhar G. Wakade

A DISSERTATION

Submitted to
Michigan State University
in partial fulfillment of the requirements
for the degree of

DOCTOR OF PHILOSOPHY

Department of Metallurgy, Mechanics, and Materials Science

1985

ABSTRACT

STRUCTURE AND PROPERTY CHANGES IN METGLAS® 2605SC INDUCED BY PULSE LASER INTERACTION.

By

Chandrashekhar G. Wakade

Metglas 2605SC foils were subjected to a high energy ruby laser irradiation to investigate the spot-welding characteristics and associated microstructural changes. Laser fluences ranging from $\approx 10^5$ W/cm² to $\approx 10^7$ W/cm² were used for this study. The inherent rapid cooling, associated with pulse laser interaction, preserves the primary amorphous structure of the resolidified metallic glass. However, even at power levels insufficient to produce substantial melting, spherulitic surface crystals were observed to grow. These spherulites upon coalescence form a network-type microstructure. Crystallization products of laser irradiated Metglas 2605SC are α -Fe, Fe₃B and Fe₂B. Pulse duration, repetition and energy input determine the nature and formation sequence of these stable and metastable crystalline phases. Laser welding of two foils of the metallic glass is possible, however, it is accompanied by some embrittlement and crack formation in the heat affected zone. The nature of these deformations depends on the sample geometry and the boundary conditions associated with the hold-down device. For the

first time, a direct experimental mapping of a crack-tip nonlinearity, in the form of a shear band zone, has been recorded. A theoretical model, which predicts such a shear band zone at the crack-tip, is used to discuss the elastic-plastic response of the metallic glass.

Metglas® is a trademark of Allied Chemical Corporation.

To Bharati and Govind, my mother and my father,
who have been ideal parents to me throughout my life
and
to Pranjali who has been an ideal wife.

ACKNOWLEDGEMENTS

I would like to express my appreciation and gratitude to Dr. Kali Mukherjee, my major advisor, for his constant support, encouragement, patience, guidance and friendship, and especially invaluable assistance in the preparation of this thesis.

Dr. Gary Cloud, Dr. C.-M. Hwang, and Dr. Jack Bass, my thesis committee members, for their support, suggestions and understanding.

Dr. Rohan Abeyaratne, for introducing me to the theoretical aspects of nonlinear crack problems and for his useful comments and discussions.

Dr. H. H. Liebermann of Allied Chemical Corporation, for providing Metglas 2605SC and the useful technical data on the metallic glass.

The Division of Engineering Research (DER) of the Michigan State University, for partial support of this research.

Mr. Leo Szafranski, Ms. Michelle Ward, and Ms. Arlene Klingbiel, for their technical assistance.

Mr. Narendra Dahotre, Mr. Subhasish Sircar, and Mr. Krishnan Narashimhan, my colleagues, for their technical assistance and help whenever needed.

Mr. Saeid Niroumand and Mrs. Grace Niroumand, my friends, for their assistance and help in preparing this manuscript.

Mrs. Pat Mukherjee for proof-reading this manuscript.

Metallurgy, Mechanics, and Materials Science Faculty and Staff members for their help and cooperation.

My daughter, Zuie, whose early arrival in this world, gave me a new burst of energy and desire to work harder.

Finally, to my friends and family, for their love, encouragement, and support, and especially to my mother-in-law, Mrs. Pramila M. Thote, for coming all the way from India to help my wife with our new born daughter, so that I could devote my time to complete this dissertation.

TABLE OF CONTENTS

	Page
LIST OF TABLES	VI
LIST OF FIGURES	VII
I INTRODUCTION	1
II BACKGROUND	3
2.1 Nature of Glassy State	3
2.1.1 Liquid-Glass Transition	5
2.1.2 Structural Relaxation	8
2.1.3 Kinetics of Structural Relaxation	10
2.1.4 The Glassy-to-Crystalline Transformation ...	12
2.2 Glass Formation	15
2.2.1 Kinetic Criteria	16
2.2.2 Methods of Preparation	18
2.2.3 Solidification Processes and Quenching Rates	26
2.2.4 Glass-Forming Alloys	30
2.2.5 Factors Affecting Glass Formation	33
2.3 Structure	35
2.4 Corrosion Behaviour	37
2.5 Magnetic Properties	39
2.5.1 Effect of Deformation and Magnetic Annealing	45
2.6 Mechanical Properties	49
2.6.1 Density and Thermal Expansion	50
2.6.2 Elastic Constants	50
2.6.3 Anelasticity	51

	Page
2.6.4 Strength and Hardness	55
2.6.5 Fatigue Behaviour and Toughness	57
2.6.6 Creep	58
2.6.7 Effect of Deformation	60
2.6.8 Annealing Embrittlement without Crystallization	62
2.6.9 Stress-Strain Behaviour	63
2.6.10 Deformation Characteristics	68
2.6.11 Deformation Mechanism	70
III EXPERIMENTAL PROCEDURE	75
IV RESULTS AND DISCUSSION	78
4.1 Laser Melting and Microstructural Characteristics of the Metallic Glass	78
4.2 Spot-Welding Characteristics	82
4.3 Crystallization Behaviour of Metglas 2605SC	85
4.4 Crack Formation in the Metallic Glass	91
4.5 Wavy Deformation and Shear Band Formation	95
4.6 High Temperature Mechanical Testing	99
4.7 Crack-Tip Nonlinearity	102
V CONCLUSIONS	109
APPENDIXES	110
LIST OF REFERENCES	112

LIST OF TABLES

	Page
1. Magnetic properties of $\text{Fe}_{80}\text{B}_{20}$ glass and comparable commercial materials	41
2. Maximum saturation magnetization obtained in various amorphous alloy systems	44
3. Mechanical properties of metallic glasses: Vicker's hardness H_v (kg mm^{-2}), fracture strength σ_f (kg mm^{-2}), Young's modulus E (10^3 kg mm^{-2})	56
4. Nominal composition and properties of Metglas 2605SC ...	75
5. Comparison of measured and calculated θ_o values	107

LIST OF FIGURES

	Page
1. Temperature dependence of viscosities η and time constant τ for structural relaxation in a Pd-Cu-Si alloy	5
2. The specific volume V of a Pd-Cu-Si alloy	8
3. Time-temperature-transformation (TTT) curves of metals	18
4. Single foil quenching technique	22
5. Piston and anvil technique	22
6. Continuous casting processes: a) twin-roller quenching; b) melt-spinning (outside); c) rotating crucible spinning; d) melt-spinning (inner); and e) melt-extraction method ...	25
7. Predicted cooling rate q as a function of section thickness t , and heat transfer coefficient h ($W\ m^{-2}\ s^{-1}$)	29
8. Representative phase diagrams of glass-forming alloy systems	31
9. Bernal's idealized holes describing the topology of dense random packing: a) tetrahedron; b) octahedron; c) trigonal prism capped with three half-octahedra; d) Archimedean anti-prism capped with two half-octahedra; and e) tetragonal dodecahedron	36
10. Moment per Fe atom in amorphous $Fe_{80}B_{20}$ alloys as B is replaced by C, Si, P or Ge	42
11. Temperature dependences of apparent yield and tensile strengths for amorphous Fe-P-C alloy	54
12. Relationship between the strain rate and the strength properties of amorphous Pd-Si alloy	54
13. Effect of strain rate on the fracture stress at various temperatures	55
14. Effect of stress on the start of crystallization in an amorphous Pd-Si alloy	59
15. Effect of cold rolling on diffraction patterns of an amorphous Pd-Si alloy	61
16. Effect of cold rolling on hardness and tensile properties of the Pd-Si alloy	61

	Page
17. Representative stress-strain curves of a Pd-Si alloy	65
18. Stress-strain curves of a Pd-Si alloy as a function of temperature	65
19. Compression stress-strain curves for a Pd-Cu-Si alloy	67
20. Schematic diagram of the experimental set-up	76
21. SEM picture of a hole drilled in Metglas 2605SC. Laser fluence $\approx 10^7$ W/cm ²	79
22. Laser damage in Al foil. Laser fluence $\approx 10^7$ W/cm ²	79
23. Dendritic resolidification structure at the lip of a laser induced hole. Laser fluence $\approx 10^7$ W/cm ²	81
24. a) SEM micrograph showing distribution of spherulites in the HAZ, b) An enlarged view of the selected area in (a) ..	81
25. Dendritic resolidification structure at the center of the laser irradiated spot. Laser fluence $\approx 10^6$ W/cm ²	83
26. a) Circumferential cracks in spot-welded region; b) transverse cracks across spot-welded region; c) Laser spot welded region showing surface rippling and crack formation; d) magnified view of region in (c) showing recrystallized polygonal domains; and e) intergranular crack along crystallized zone	84
27. XRD results from as-received and isothermally annealed Metglas 2605SC	86
28. XRD results of various isothermal annealing treatments on the metallic glass showing α -Fe and Fe ₃ B peaks	86
29. A comparison of x-ray diffraction intensity profile from an as-received sample and a laser annealed foil	88
30. A comparison of x-ray diffraction intensity profile from an as-received sample and a laser annealed foil	88
31. a) SEM picture showing crack formation; b) magnified view of selected region from (a) showing concentric bands	93
32. SEM picture showing tearing steps	94
33. a) SEM micrograph showing tearing steps and a crack-tip shear band zone induced by laser irradiation in Metglas 2605SC when covered with a transparent overlay; b) magnified view of the crack-tip shear band zone seen in (a)	94

	Page
34. SEM micrograph showing wavy deformation bands	96
35. Coarse ($\sim 3 \mu\text{m}$) shear bands seen on the fracture surface near the hole	97
36. Finer ($\sim 0.05 \mu\text{m}$) shear band spacing observed on the crack surface away from the laser irradiated zone	97
37. Shear bands in Metglas 2605SC produced by mechanical tearing at ambient temperature	98
38. Crack-tip shear band zone induced by laser damage in the metallic glass. Angle of tilt 30°	98
39. Stress-strain response curves of the metallic glass as a function of temperature	100
40. Tensile fracture surface showing characteristic vein pattern	100
41. Response curve in simple shear for a power-law material ...	104
42. Cauchy shear stress-strain curve assumed by Knowles and Sternburg for a special class of materials	104
43. Crack-tip shear band zone predicted corresponding to the response curve shown in Figure 42	106
44. SEM picture showing evidence of normal surface displacement in the laser irradiated metallic glass specimen	106

I INTRODUCTION

In practical applications involving metallic glasses it may become necessary to join two foils by using a welding technique. Unfortunately at elevated temperatures ($T \geq T_g$, the glass transition temperature) the physical and mechanical properties of metallic glasses are degraded (1-9). The mechanical properties of metallic glasses are extremely sensitive to the degree of crystallinity. The onset of crystallization causes a number of structural changes in metallic glasses due to the formation of various stable and metastable phases. It is well known (4,10,11,12,13,14) that the crystallization mechanism in metallic glasses is of nucleation and growth type. In certain metallic glasses, the crystallization process is very sensitive to the precise initial composition of the material, temperature, and the heating rate (15,16).

In conventional welding techniques, such as resistance spot-welding for example, the heat affected zone (HAZ) is relatively large, and the heating cycle lasts for several seconds. Morris (14) has shown that a heating cycle as short as half-second, can cause crystallization in Metglas 2826. Thus, a successful spot-welding of such a material may only be possible when the heating and cooling cycles are much shorter. A pulse laser might be a suitable candidate for such a purpose for the following reasons: i) the heat affected zone would be quite narrow, ii) energy input to the welding region could be precisely controlled, and iii) cooling rate of the molten pool could be comparable to or greater

than the cooling rate in melt spinning and thus the amorphous structure could be preserved.

Interaction of a high energy laser pulse with a solid produces two nearly simultaneous effects: (i) a temperature spike within the irradiated volume and (ii) an elastic/plastic deformation front which propagates through the solid. The nature and magnitude of these two events depend on the thermophysical properties of the solid, input energy, spot size and energy-time profile of the laser pulse (17). Highly localized thermal expansion, in the wake of a rapid heating pulse at the surface of an elastic solid, promotes a stress wave which propagates into the interior of the solid. The magnitude of the peak stress is a strong function of the pulse duration, and for a pulse lasting a few nanoseconds, fracture and spallation are possible even in a very ductile metal (18). Thus, a ruby laser with normal pulse operation was preferred over a Q-switched operation. Results of such a pulse laser interaction with Metglas 2605SC ($\text{Fe}_{80}\text{B}_{14.5}\text{Si}_{3.5}\text{C}_2$) are reported in this investigation.

II BACKGROUND

2.1 Nature of Glassy State

The word "glass", in its original meaning refers, to an amorphous or a non-crystalline solid formed by continuous cooling of a liquid. A solid is defined as any body having a viscosity greater than 10^{14} P. A glass, like the liquid from which it is formed, lacks three dimensional atomic periodicity, however, has compositional homogeneity. Lack of three dimensional long range order can be verified easily by the presence of a limited number of diffuse halos in x-ray, electron, and neutron diffraction patterns. A x-ray diffractometer generally exhibits broad peaks centered in the range in which strong peaks are also seen in the diffraction patterns of the corresponding crystalline phase(s). High resolution electron microscopy reveals no diffraction contrast and, in particular, reveals none of the contrast effects normally associated with grain and lattice defect structures. Such effects are characteristic of amorphous solids indicating that any coherently scattered diffraction domains present are smaller than about 20 Å in diameter (19).

The expression "glass" is sometimes also used to describe amorphous solids produced by electrodeposition, vapor condensation, sputtering, and ion implantation based on the similarity in diffraction patterns and crystallization behavior between amorphous solids formed by atomic

condensations and ones formed by liquid solidification (19). Noncrystalline solids produced by different methods are often indistinguishable in x-ray measurements, but their physical properties may differ drastically in as-prepared state, Ni-P glasses produced by liquid quenching method are ductile whereas electrodeposited amorphous Ni-P alloys are very brittle (20). In this dissertation, the term "metallic glass" or "glassy metal" is used to describe non-crystalline solids formed by continuous cooling of a melt to distinguish it from amorphous solids formed by other methods which are referred to as amorphous metals for the sake of clarity. The term "metallic glass", however, is somewhat misleading because the majority of the glassy metals synthesized are in reality alloys containing metallic as well as nonmetallic elements. Their physical properties though are typically metallic.

During the solidification of a melt to form a glass, no essential change in the spatial atomic configuration occurs. Hence, a liquid and a glass can be considered to belong to the same phase structurally and thermodynamically. In other words, a glass may be considered as a solid with frozen-in liquid structure. The structure of a glass can be clearly distinguished from that of a liquid, because glass structure is independent of temperature but depends on the means of preparation and heat treatment. Whereas for a liquid, both structure and properties are independent of thermal history. A glass, when given sufficient time and atomic mobility, relaxes structurally towards a more stable equilibrium state, hence it is considered to be metastable with respect to crystalline phase and transforms to stable configuration through the process of nucleation and growth. In the following sections important attributes of the glassy state, the glass-to-liquid transition, structural

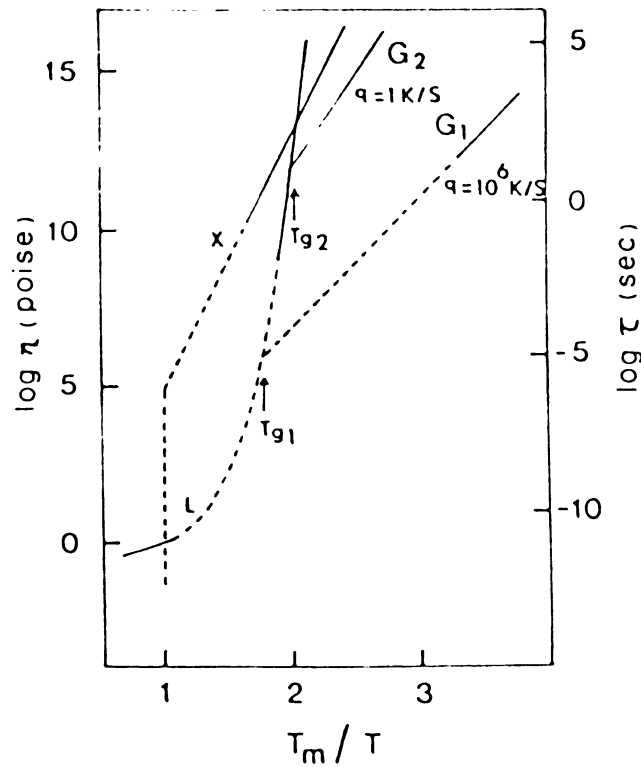


Figure 1: Temperature dependence of viscosities and time constant for structural relaxation in a Pd-Cu-Si alloy (21).

relaxation, and crystallization behaviour are described.

2.1.1 Liquid-Glass Transition

The temperature dependence of viscosities of a Pd-Cu-Si glass forming alloy (21) is shown schematically in Figure 1 to illustrate the liquid-solid transformation. In this figure, the solid lines represent the experimental data. The logarithm of viscosity η and structural relaxation time τ are plotted against the reciprocal of reduced temperature T_m / T , where T_m is the thermodynamic equilibrium melting temperature. τ is the average time required for atomic rearrangement and is related approximately to viscosity η and shear modulus μ by:

$$\tau = \eta/\mu \quad 2.1$$

with $\mu = 10^{11}$ dynes cm^{-2} for amorphous alloys.

The viscosities of molten metals above T_m are low (10^{-2} P) and increase slowly on cooling with a relatively low activation energy $Q \approx 3 kT_m$. On super cooling a liquid below T_m , it either crystallizes or forms a glass. On crystallization, η increases discontinuously by many orders of magnitudes and then follows a path X with activation energy $Q = 3eV$. If crystallization is bypassed, η increases continuously with decreasing temperature following the path L. The rate of increase in η and the time constant τ of the liquid increase with increasing undercooling. Below the melting temperature, the viscosity of supercooled liquids can be described empirically by Vogel-Fulcher expression (21-23)

$$\eta = \eta_0 \exp [B / (T - T_0)] \quad 2.2$$

where η and B are constants depending upon materials and T_0 is an ideal glass transition temperature. This form of temperature dependence of η has also been observed to be true in many oxide glasses and other nonmetallic glassy materials near the glass transition. For liquid metals and organic liquids, B is small and represents a small fraction of the chemical bonding energy, while T_0 represents a large fraction (1/3 to 2/3) of T. In network forming liquids, values of B are large and are of the order of chemical bonding energy, and T_0 is low. In pure silica or germania, the viscosities are well described by an Arrhenius equation (24). η of the oxides is high ($\approx 10^7$ P) even above T_m and increases rapidly with decreasing temperature.

At sufficient undercooling, the time constant of the liquid, τ , becomes comparable to or greater than the duration of experimental measurement. Below this temperature, the atomic configuration remains

virtually unchanged, thus giving rise to the discontinuity in the η against T relationship and is observed to follow an Arrhenius expression (25)

$$\eta \propto \exp (Q/kT) \quad 2.3$$

The temperatures, T_{g1} and T_{g2} , which correspond respectively to fast and slow cooling and mark transition from equilibrium liquid state to frozen-in non-equilibrium structure of iso-configurational structure, are known as glass transition temperatures T_g . At T_g , the structural relaxation time τ_g is related to the rate of cooling $q \equiv -dT/dt$ by (26)

$$\tau_g \approx (kT_g^2 / Q_a q) \quad 2.4$$

where Q_a is the apparent activation energy for structural relaxation of the supercooled liquid, $\tau_g \propto \exp (Q/kT_g)$ and k is Boltzmann's constant. For most metallic glasses, $Q_a \approx 4$ eV, $T_g \approx 700$ K and hence $(kT_g^2 / Q_a) \approx 2-10$ K.

At different cooling rates, the glass freezes in a different state e.g. G_1 and G_2 . The glass has a lower viscosity and greater specific volume and internal energy when produced at a faster cooling rate. Figure 2 shows the corresponding specific volume of a Pd-Cu-Si glass (27). At the fast cooling rate of 10^6 K/s, usually experienced during melt spinning of metallic glasses, the glass freezes at T_g , at which $\tau_g = 10^{-5}$ s, into a glass denoted by G_1 . At slower cooling rates ≈ 1 K/s, the glass freezes at low temperatures T_{g2} and the resultant glass G_2 has higher viscosities below T_g by at least six orders of magnitude than does the glass G_1 produced at higher cooling rates.

If the crystallization of a glass is sluggish enough in a temperature range just above T_g , then a reversible transition from a glass to the undercooled state can be observed experimentally (28,29).

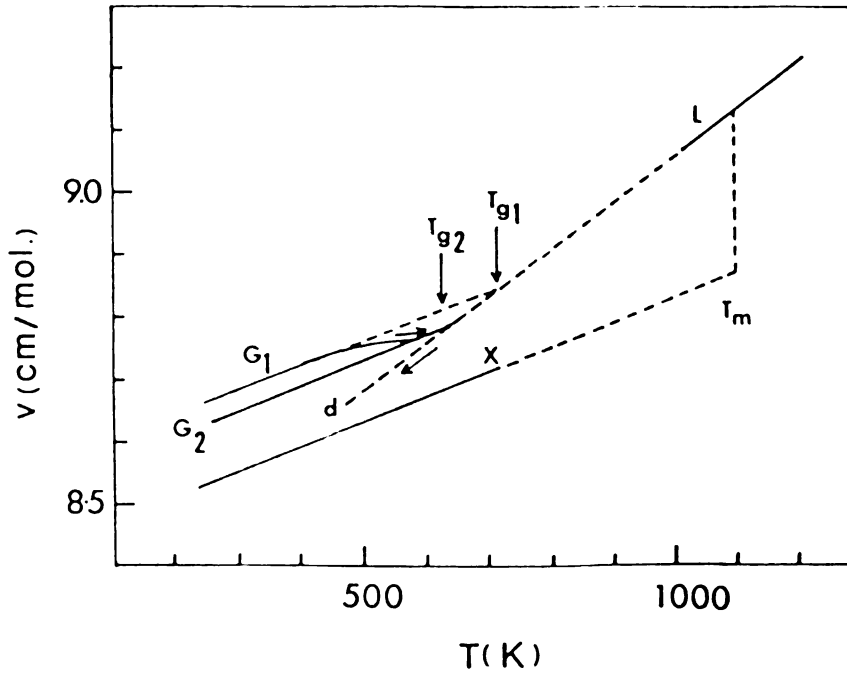


Figure 2: The specific volume V of a Pd-Cu-Si alloy (27).

In many other glassy metals, however, the glass-liquid transition is unobservable at slow rates of measurements due to the intervention of rapid crystallization process.

2.1.2 Structural Relaxation

Glasses, in as-prepared state, are thermodynamically unstable with respect to the fully relaxed glassy state and tend to relax structurally to the latter stage at a rate which depends on the previous thermal history and temperature. The glasses produced at higher cooling rates which possess a greater frozen-in structural disorder and thus high diffusivity, would relax structurally at relatively lower temperature compared to glasses produced at slower cooling rates. Evidence for structural relaxation upon annealing (30,31) at temperatures below the crystallization temperature and at times insufficient to cause

detectable crystallization was observed by such phenomena as internal friction (32,33), stress relief(34), stress relaxation and creep (25, 35), recovery from cold work (36), specific heat (37), and magnetic annealing (38). A direct indication of structural changes was obtained by x-ray diffraction studies by Waseda and Masumoto (39).

Upon heating a glass undergoes structural relaxation in the temperature range for which the time constant for structural relaxation of the glass is given by

$$\tau_g \approx t_{\text{mea}} \approx Aq^{-1} \quad 2.5$$

where $A = kT^2/Q_g \approx 10K$. Q_g is the activation energy for the structural relaxation of the glass and is usually low ($\sim 1-2$ eV). At slow heating rates of ≈ 1 K/s, the glass G_1 would have value of $\tau_g \approx 10$ s and would undergo structural relaxation at temperatures far below T_{g1} . The glass G_2 , which is produced at slower cooling rates or preannealed near T_g , would have $\tau_g > t_{\text{mea}} \approx 10$ s and would not show structural relaxation below T_{g2} . Both G_1 and G_2 , however, undergo glass-liquid transition at temperature T_g , upon slow heating. If the glass G_1 is heated at rates higher than the quenching rate of 10^6 K/s, e.g. during laser heating, the glass would exhibit negligible structural relaxation and transform to liquid at or above T_{g1} .

As shown in Figure 2, the glass G_1 , produced at a faster rate of cooling, has a specific volume greater by $\sim 0.5\%$ than does the slowly cooled glass G_2 . At extremely slow cooling rates, volume contraction follows path d. In practice, length of path d is limited by the increasingly slow rates of cooling that are required. Further extrapolation of the glassy volume, V , would intersect the crystalline value ~ 200 K below T_g , corresponding approximately to the ideal glass

transition temperature T_0 .

Upon heating the quenched glass G_1 , at rates slower than the rates of quenching, e.g. 1 K/s, the glass at just above room temperature exhibits an irreversible contraction that is caused by structural relaxation. The initial contraction is small and becomes more pronounced at higher temperatures. At the glass transition, the glass transforms to a liquid, and coefficient of thermal expansion increases by a factor of two. Upon further heating, the glass crystallizes and its volume contracts by $\sim 1-2\%$. The volume contraction associated with structural relaxation is about one third the volume change that accompanies crystallization. This fraction ($\sim 1/3$) is also the ratio of heat evolution and elastic constants associated with structural relaxation to those of crystallization (27,37).

Many physical and mechanical properties such as mechanical ductility (31,40), microhardness (41), electrical resistivity (41), atomic diffusivity (42) and magnetic anisotropy (40) alter significantly upon structural relaxation. This was attributed to local structural and compositional fluctuations at temperatures well below crystallization temperature. The change in density associated with metallic glasses is small, $\sim 0.5\%$; however, change in other physical properties is appreciable, e.g. Young's modulus by $\sim 7\%$ (27,32,33,43), internal energy by ~ 200 cal/mol (37), Curie temperature by as much as 35 K (44), and atomic diffusivity by many orders of magnitude (42).

2.1.3 Kinetics of Structural Relaxation

The rate of isothermal isobaric volume change can be written as

$$d(V - V_e) / dt = (V - V_e) / \tau_v \quad 2.6$$

where t is the experimental time, V and V_e are actual and equilibrium specific volumes of the glass respectively and τ_v is the volume retardation time. The form of equation (2.6) is applicable to the rate of change in various physical properties such as viscosity, magnetic anisotropy and Curie temperature. The temperature dependence of the relaxation time for various properties is similar. The rate of stabilization depends on the experimental procedure because the relaxation time is determined not only by temperature of measurement but also by overall free volume. The rate of structural relaxation is greater for glasses produced at higher rates of quenching and for glasses with lower T_g (45,46). Isothermal structural relaxation of metallic glasses near T_g has been studied from the change in x-ray intensity function (30), from enthalpy recovery, and Curie temperature aging (47). The rate of equilibrium obeys approximately logarithmic time law. This relationship is different from the exponential time dependence frequently observed in magnetic aging (48,49) in which the relaxation kinetics are described by the first-order rate reaction with a single relaxation time.

In stress relief and magnetic aging experiments at temperatures below T_g , the kinetics of annealing is given by equation (2.6) with a single thermally activated process having $Q \sim 1$ eV. The stress relief of as-quenched glasses exhibits two processes, the initial short-time relaxation and the final long-time relaxation (50). The rates of stress relief are reduced drastically, but the apparent activation energies ($Q_{re} \sim 1$ eV) are not affected much in glasses produced at slower cooling rates.

2.1.4 The Glassy-to-Crystalline Transformation

If an amorphous solid is heated to high enough temperature or annealed for a longer time, it will transform to crystalline state. The process of crystallization involves nucleation and growth of the crystalline phase. Liquid-to-crystalline transformation is an extremely fast phase change and takes place at well defined temperatures, whereas glass-to-crystalline transformation is a rate process. The rates of glass-crystal transformation are usually dominated by frequency of nucleation and hence depend not only on atomic diffusivities but also strongly on glass-crystal interfacial energy and entropy of fusion. In other words, the transformation kinetics depends not only upon the transport properties, but also on the relative stability of the crystalline phase. The ease of glass formation and the stability of alloy glasses thus, in general, occur in parallel. Empirically, glasses with eutectic compositions are most stable, and ternary alloy glasses that form readily at slow cooling rate are more stable than the corresponding binary alloy glasses (29).

The kinetics of transformation are analyzed using the generalized theory of phase transformation (51,52), $x = 1 - \exp(-k_n t^n)$ where x is the volume fraction transformed in time t , k_n is a kinetic constant, and the exponent n is determined by transformation mode. n ranges from 2.5 to 4 for Pd-Si glasses (53-55), whereas values from 3 to 5 are obtained in Fe-based glasses (56-58). In a Pd-Ag-Si alloy value of n reported is equal to unity (59). The activation energy, Q_x , for crystallization varies widely with composition and temperature of transformation. In several stable glasses such as Pd-Cu-Si (53), Pd-Ni-P (60), Fe-Ni-P-B (61), Zr-Cu (31) which crystallize above T_g , Q_x is high (> 4 eV) and

comparable to the Q_η for the viscous flow in an equilibrium glass. For most metallic glasses which crystallize near or below T_g , Q_x ranges from 4 eV to 2 eV (1,9,61,62). Most monoatomic amorphous metals which are thermally least stable exhibit a very low $Q_x \leq 1$ eV and crystallize at about 20 to 50 K, which is just above the vapor deposition temperature (63). Pd-Si (1,64) and Cu-Zr (4,65) alloys undergo crystallization during annealing below T_g , whereas Fe-Ni-based alloys crystallize near T_g . The occurrence of crystallization in many metallic glasses far below T_g , apparently reflects the high nucleation frequency and high diffusivities in the unrelaxed glassy state so that crystallization proceeds concurrently with the structural relaxation.

The crystallization process is marked by an exothermic peak in the differential scanning calorimeter (DSC) trace, by abrupt changes in mechanical and magnetic properties, and by presence of sharp peaks in a diffraction pattern. Crystallization behaviour of amorphous ferromagnetic glassy alloys is studied by Mossbauer spectroscopy. Measuring electrical resistivity as a function of temperature is a simple technique used extensively to determine the approximate temperature at which crystallization proceeds rapidly. The onset of crystallization is marked by one or several rapid drops in resistivity-versus-temperature plot. Appearance of multiple steps in the plot indicates formation of metastable crystalline phases which later are replaced by more stable phases at higher temperatures.

Various crystallization morphologies are observed to develop depending on the annealing temperature and composition. In vapor deposited amorphous Ni-P films, the mode of crystallization was found to be dependent on phosphorus content (66). The facet and dendritic

morphologies are expected modes of crystallization. For a glass with a continuous random type of structure, whereas a microcrystalline body might be expected to crystallize by grain growth process. However, an extremely fine-grained crystallite structure might arise from copious homogeneous nucleation of the crystal followed by crystallite coarsening. In $\text{Fe}_{40}\text{Ni}_{40}\text{P}_{14}\text{B}_6$ crystallization was observed to take place by nucleation and growth of crystal having a barrel shape (11,14,40,67), whereas for $\text{Fe}_{50}\text{Ni}_{30}\text{B}_{20}$ and $\text{Fe}_{80}\text{B}_{20}$ alloys, crystallites exhibited a characteristic cylindrical shape with rounded ends and flattened sides (68). Yeh and Maddin (56) have reported often appearance of different crystallization morphologies in the same sample. Shimomura et al. (10) have reported marked changes in the morphology of crystalline phases as a result of a small change in the composition of the amorphous Fe-based alloys. Crystallization processes of metallic glasses are quite complex. Crystallization behaviour of various metallic glasses has been reported in the literature (4,9-15,40,65,67-91).

Thus, upon heating, a glass exhibits three characteristics: structural relaxation, a glass-liquid transition, and crystallization. Structural relaxation occurs when the glass attains appreciable mobilities such that $\tau_g(T, q, \text{etc.}) \approx t_{\text{mea}}$, while the glass transition takes place when the time constant of the relaxed glass $\tau_1(T)$ approaches $t_{\text{mea}} \propto q^{-1}$. The observed glass transition temperature T_g is thus determined by the heating rate during measurement and is less susceptible to previous heat treatments. In contrast, the rates of structural relaxation depend critically on previous history. Glasses produced at high quenching rates or subjected to cold-rolling or irradiation processes exhibit highly disordered structure and high

atomic mobilities, and thus may undergo structural relaxation far below T_g (50,92). Annealing drastically reduces atomic mobilities and the rate of structural relaxation. Since the kinetics of crystallization processes are governed not only by atomic diffusivities but also by thermodynamic parameters, there is no unique correlation between the stability of a glass as indicated by the crystallization temperature T_x and the glass transition temperature T_g . In general, however, more easily formed glasses are more stable.

2.2 Glass Formation

Structural and kinetic criteria have been proposed to describe the process of glass formation. Rawson (93) and Cahn (94) have reviewed many of the structural theories. These theories take into consideration the atomic structure, atomic size effects, and bonding to predict glass formation tendency. The kinetic criterion, developed mainly by Turnbull and Cohen (95) and by Turnbull (96), considers rate of cooling relative to the kinetics of crystallization. This theory assumes that any material may be rendered glassy if quenching rates are high enough to avoid crystallization. The two criteria are complementary. The structural criteria based on chemical bonding, coordination or chemical structure merely imply indirectly that the free energy of particularly stable glassy structure will be low enough to make the driving force for crystallization negligible. The kinetic criteria which have been successfully employed to predict ease of glass formation are described next.

2.2.1 Kinetic Criteria

Adapting simple nucleation theory and assuming the avoidance of a single nucleus as the criteria for glass formation, Turnbull (96) estimated quantitatively the condition for glass formation. The homogeneous nucleation frequency I for normal metals is expressed by

$$I(\text{cm}^{-3}\text{s}^{-1}) = \frac{10^{30}}{\eta} \exp(-b\alpha^3\beta/T_r\Delta T_r^2) \quad 2.7$$

where η is viscosity, b is the shape factor (e.g. for a spherical nucleus $b=16\pi/3$), the reduced temperature $T_r=T/T_m$ and $\Delta T_r=1-T_r$ with T_m as the melting temperature. Here α and β are dimensionless parameters related to the liquid-crystal interfacial tension σ and the entropy of fusion ΔS_f and are given by $\alpha = (N_o V)^{1/3} \sigma / \Delta H_f$ and $\beta = \Delta S_f / R$, where N_o is Avogadro's number, V is the molar volume in the crystal, ΔH_f is the molar heat of fusion, and R is the gas constant. For constant $\eta=10^{-2}$ P, the nucleation frequency I increases sharply with ΔT_r from zero to a broad peaked maximum at $T_r = 1/3$. The peak nucleation frequency $I_{\text{max}} \approx 10^{32} \exp(-113\alpha^3\beta)$ depends strongly on thermodynamic parameters and decreases sharply from 10^{31} to 10^{-4} $1/\text{cm}^3\text{s}$ as $\alpha\beta^{1/3}$ increases from 0.25 to 0.9. Turnbull concluded that liquids with $\alpha\beta^{1/3} = 0.9$ should readily form glasses, while for liquids with $\alpha\beta^{1/3} < 0.25$, it should be impossible to suppress crystallization. Glass formation is thus enhanced greatly by a large interfacial energy and entropy of fusion. $\beta \approx 1$ for metals, SiO_2 , GeO_2 , organic plastic materials, and many strong acids and bases, while for typical organic and inorganic compounds, ranges from 4 to 10. Droplet nucleation experiments indicate that for typical metals $\alpha = 0.4$ to 0.5 , and for most non metals $\alpha = 0.33$. The progressive increase in β improves the glass-forming tendency. The network liquids such as SiO_2 , B_2O_3 , P_2O_5 , GeO_2 etc. form glasses easily

because of their extremely high viscosity at T_m .

Uhlmann (97) and Davies (98) have carried out a qualitative estimation of the critical quenching rate for glass formation. For this they have considered the theory of nucleation and growth and the Johnson-Mehl treatment of transformation kinetics. In this approach time-temperature-transformation (TTT) curves corresponding to a small volume fraction of crystalline phase are constructed, and then these curves are used to estimate minimum quenching rates, q_{CR} , for the formation of various glasses.

The reduced glass transition temperature, $T_{r_0} = T_0/T_m$, is the most important factor determining the glass forming abilities for metals, where T_0 is an ideal glass transition temperature. Increase in T_{r_0} drastically lengthens the time at the nose of the TTT curves, sharpens and shifts the nose to smaller undercooling as shown in Figure 3. With an assumption that viscosity is dependent on temperature, q_{CR} is observed to vary from $\approx 10^9$ K/s to 10^2 K/s as T_{r_0} increases from 0.3 to 0.6. These values agree reasonably with the values estimated experimentally e.g. 10^{10} K/s for pure metals Ni and Pd; 10^6 K/s for glass forming alloys Au-Si, Ni-P, Pd-P; and 10^2 K/s for easy glass formers Pd-Cu-Si, Pd-Ni-P. For the above systems, $T_{r_0} \approx 1/4, 1/2$ and $2/3$ respectively.

The glass transition temperature T_g depends weakly on composition. The increase in T_{r_0} and hence the drastic enhancement of glass-forming tendency in these alloy systems is due to lowering of the liquidus temperature. Near eutectic compositions have lowest liquidus temperature, hence form glasses quite easily as evidenced for most metallic glasses and ionic glasses in which bonding character is not altered drastically. The estimation of q_{CR} by the construction of TTT curves

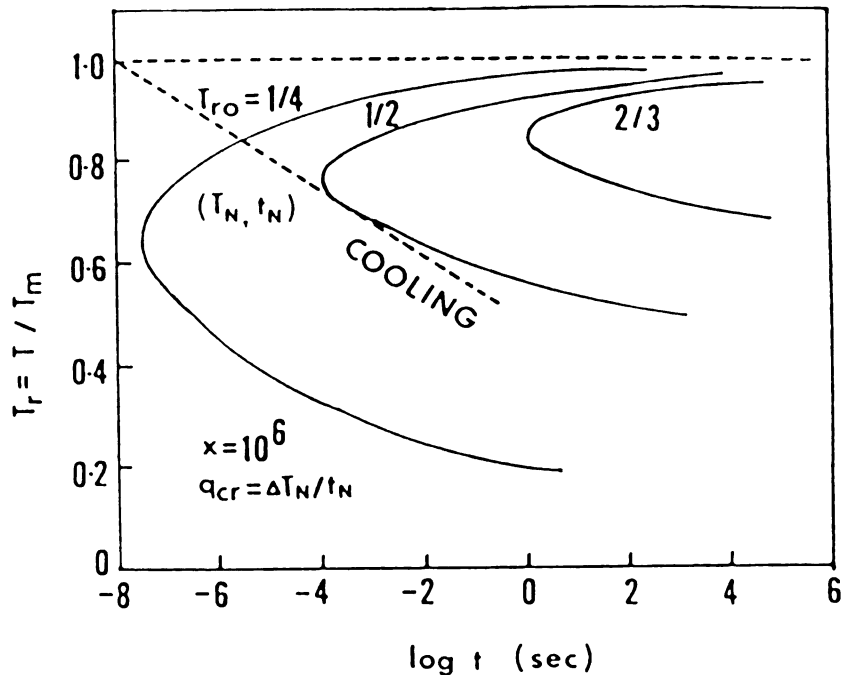


Figure 3: Time-temperature-transformation (TTT) curves of metals.

implicitly assumes that the crystallization kinetics over the full range of temperature is as rapid as at the temperature of the nose and thus overestimates q_{cr} by about a factor of three, estimated from the continuous cooling curves (99).

2.2.2 Methods of Preparation

Glassy metals have been known for many years. As early as 1845, Wurtz has reported a method of obtaining a nickel deposit on iron by chemical deposition of a Ni solution with hypophosphide. From the details given in that paper, it is most likely that the metallic deposit was amorphous, but it could not have been confirmed until the discovery

of x-rays 65 years later. A number of amorphous alloys were prepared by chemical deposition method in early 1950s, however, emphasis was given to the mechanical and chemical properties. In 1960 Klement et al. (100) reported the production of Au-Si glassy metal by quenching from a melt. Since then the liquid method has been extensively developed and has become the preferred method because it is faster, applicable to a wider range of composition, probably gives material of more uniformity and few unknown contaminants, and is adaptable to large scale production. The field of glassy metals is expanding so rapidly that it is difficult to describe all the techniques in detail that are being used.

2.2.2.1 Electrochemical Methods

These methods can be considered as standard electrolytic or electroless techniques for the following reasons: (i) the metallic deposit is glassy and resides in the chemical composition of the bath, (ii) its pH, and (iii) its temperature. When a potential is applied to the cell, the current density is also important. The number of glassy metals obtainable by electrolysis is very limited. The truly amorphous structure of these alloys has been established for transition metals Ni (101,102), Co (103), and Fe (104) with P.

2.2.2.2 Rapid Quenching Techniques

With the exception of easy glass forming alloys such as Pd-Cu-Si, Pd-Ni-P, and Pt-Ni-P, most metallic glasses are produced at a relatively high cooling rate of 10^5 K/s or higher. The high quenching rates are accomplished by spreading a thin layer of liquid in good contact with a

ni

ra

on

la

or

ca

co

co

at

fr

pr

si

va

no

ch

an

ve

la

on

an

ra

pr

chi

de

highly conductive substrate, e.g. metals or sapphire. The quenching rate is determined by the rate of heat transfer at the liquid-substrate interface and the thickness and thermal conductivity of the liquid layer. Usually the thickness of the quenched metallic glass in which crystallization is prevented, is limited to $\sim 50 \mu\text{m}$. Amorphous solids can also be formed by methods in which the liquid state is bypassed completely. These processes, known as atomic deposition or atomic condensation, involve growth from the vapor phase by thermal evaporation, sputtering or from decomposition of gaseous compounds by radio frequency discharges. These techniques provide a very high effective quenching rate and yield amorphous solids which cannot be obtained as a glass by liquid quenching.

2.2.2.2A Vacuum Evaporation and Sputtering Methods

Vacuum deposition offers a method of very fast quenching rate from vapor to solid phase. The atoms in the vapor phase strike the substrate more or less independently of their neighbors, but once on the substrate the diffusion paths are very short (of the order of atomic distances), and as soon as stable nuclei are formed, the growth of a crystal can be very rapid. Hence amorphous metals or alloys have been obtained (including superconducting amorphous films of Bi, Ga, As, Sb, and Be), only on substrates maintained at liquid-helium temperature (4 K). Many amorphous films are very unstable and crystallize with a temperature range of 20-50 K. Thus it is necessary to study the structure and properties of such films within the evaporation chamber. In spite of this difficulty, vacuum evaporation is the only method by which pure metals, particularly high melting point transition metals can be

obtained in the amorphous state. It has been suggested that the unavoidable presence of traces of impurities may stabilize an amorphous structure. The crystallization temperature of amorphous Co and Fe films increased with an increase in residual gas pressure, as reported by Ichikawa (105), strongly support the view.

Many alloys of metals or metals and metalloids that have not been prepared in glassy phase by liquid quenching can also be prepared in amorphous form by vapor deposition or by sputtering. Binary alloys of metals such as Cu-Ag and Co-Au (106), Au-Ni (107), Pb-Au (108), Fe-Au (109), and Fe-Si (110) were produced in the form of amorphous films by deposition on targets at 80 K and are stable at room temperature. Solid-state immiscibility and a large (> 10%) difference in atomic radii of the constituents has been proposed as the criteria for amorphous phase formation by Madder (111). In liquid quenching, the glass forming compositions generally lie near a low melting eutectic. As different processes are involved in vacuum evaporation and liquid quenching, the different criteria for glass formation in each case are justified (112).

In sputtering method, atoms of the source material are bombarded by high energy inert gas atoms. Atoms are removed from the source by collision with the inert gas ions instead of thermal evaporation. Amorphous alloys can be obtained by sputtering on a substrate at room temperature and these alloys are more stable than vapor deposited ones.

2.2.2.2B Liquid Quenching

The principle behind liquid quenching technique is to retain in the solid state the atomic arrangement present in liquid state at the

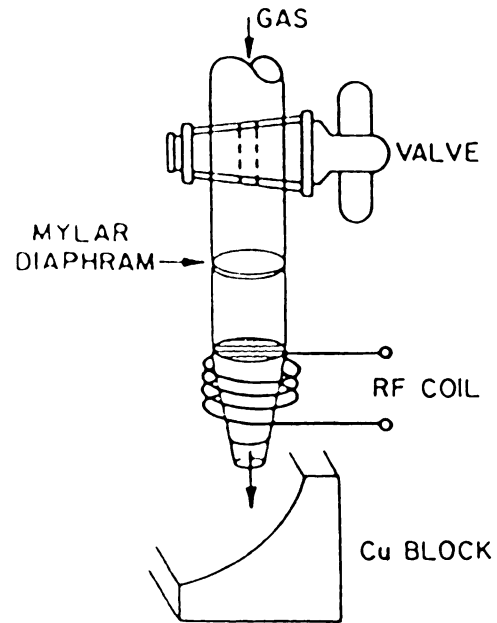


Figure 4: Single foil quenching gun technique (100).

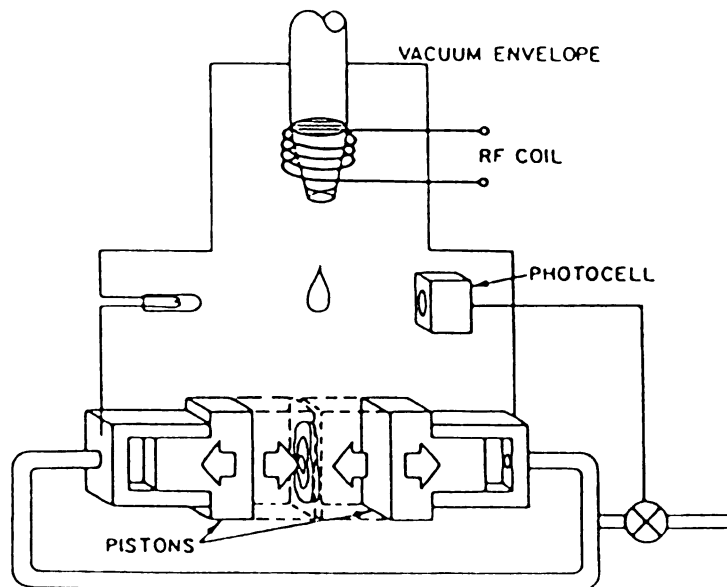


Figure 5: Piston and anvil technique (113).

quenching temperature. If the liquid alloy could be cooled fast enough, so as to avoid the normal process of crystallization, then the liquid structure can be said to be "frozen-in". This requires very rapid rates of heat transfer to the cooling medium and are achieved by conduction from the liquid to a highly conductive metallic substrate. In addition, the condition that the layer of liquid alloy in contact with the substrate must not exceed a certain thickness must be satisfied. This is necessary since the rate of cooling at a point away from the substrate decreases with the distance from the substrate. Using these conditions as criteria, Klement, Willens and Duwez (100) synthesized the first metallic glass $\text{Au}_{75}\text{Si}_{25}$ from a liquid by the now classical gun technique (also splat cooling) (Figure 4). In this process, a small liquid globule was propelled via a gaseous shock wave onto a copper substrate. The substrate was curved so that centrifugal force promoted good thermal contact between the liquid layer and the substrate. Quenched samples produced were irregular in shape with thickness varying from about 1 μm to 10 μm . In the gun technique, heat is extracted from the melt from one side only. Pietrokowsky (113) designed a piston and anvil technique in which the liquid globule was squeezed between a fast moving piston and fixed anvil (Figure 5). Both piston and anvil were lined with copper to insure fast heat removal. The rate of cooling obtained by the gun technique is often mentioned as being about 10^6 K/sec. The rate of cooling mentioned here is only a rough average, since the actual rate varies not only from point to point but also with time during quenching. The average rates of cooling in gun technique differ by one order of magnitude. The piston and anvil method gave geometrically better samples, e.g. 2 cm in diameter and 20-50 μm in thickness.

Methods of making long ribbons since first reported, have been extensively developed. The ribbon-making methods are basically similar; a continuous jet of liquid metal is directed on a moving metal surface, or between two metal rolls, or sometimes into a moving liquid stream. The techniques are called by various names: melt-spinning, liquid quenching, chill-block spinning, roller quenching etc.

The first continuous casting process was reported by Chen and Miller (114) and investigated extensively by Babic et al. (115). In this two-roller or roll-quenching process, a molten metal stream was directed into a gap between a pair of rapidly rotating rollers lined with copper. By proper adjustment of mass flow of the liquid alloy, temperature, the peripheral velocity of the rolls, and the size of the gap, the resultant product obtained was a metallic glass ribbon about 2 mm in width and 50 μ m in thickness. Other commonly used techniques are melt-spinning processes of Strange and Pim (116) (Figure 6b), and Pond and Maddin (117) (Figure 6c) in which the molten stream is cast respectively onto the outside or inside of a rotating drum. These techniques were developed originally for fabricating crystalline filaments and later adopted for continuous production of metallic glass ribbons (1, 118). In comparison with Strange and Pim process, the Pond and Maddin process yields a higher quenching rate because centrifugal force allows better thermal contact between the melt and drum surface. The disadvantage in this process is that quenched samples are difficult to remove from the drum. A process developed by Chen and Miller (119) is shown in Figure 6d. By impinging a stream of melt onto the inner sloped surface of a rotating drum, good heat transfer between the melt and substrate was ensured and continuous fabrication of glassy filaments was achieved.

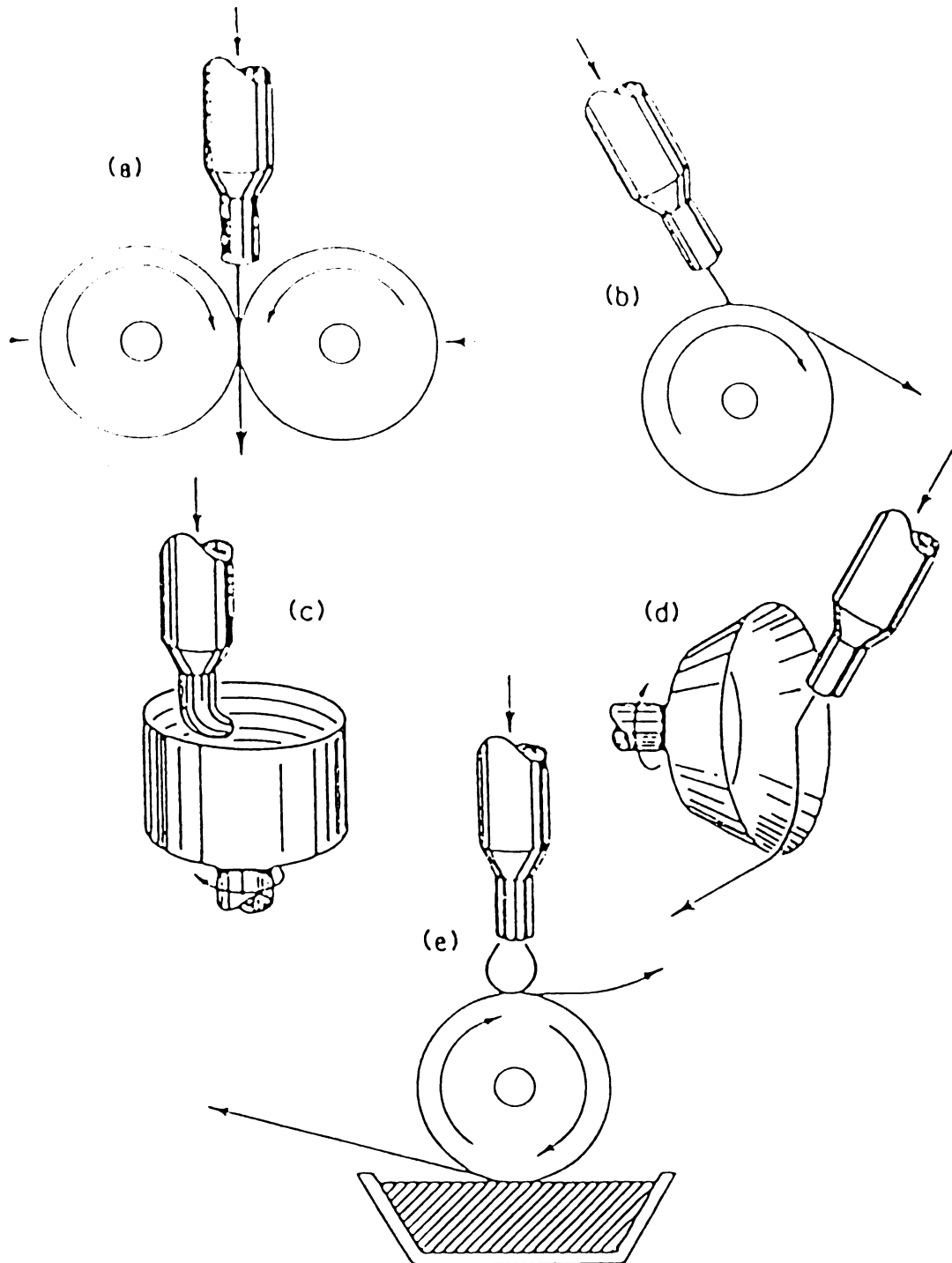


Figure 6: Continuous casting processes: a) twin-roller quenching (114, 115); b) melt-spinning (outside) (116); c) rotating crucible spinning (117); d) melt-spinning (inner) (119); and e) melt-extraction method (120).

In a melt-extraction method (120) the periphery of a spinning disc is brought into contact with the surface of a melt or a molten drop at the end of continuously fed rod of alloy (Figure 6e). The liquid alloy solidifies upon contact with the disc and separates from it because of the radial acceleration. The roller quenching method has an advantage over melt casting by extracting heat from both sides and in principle yields metallic glasses twice as thick for a given cooling rate and with smooth surfaces of uniform thickness.

Other methods of quenching liquid alloys, such as plasma spraying (121), explosive forming (122) and melt atomization (123,124) which yield glass surface layer have not been much explored for fabrication of metallic glasses. Laser surface melting (125) was first successfully employed to demonstrate formation of a glassy Pd-Cu-Si surface layer on a crystalline alloy of glass-forming composition. The quenching rates reported were higher than 10^{10} K/s. Poate et al. (126) reported production of amorphous layer of Pt-Si on a silicon single crystal substrate with a very short pulse laser interaction. Since then vitrification of various metallic glasses by laser glazing has been reported (127-132).

2.2.3 Solidification Processes and Quenching Rates

Basic apparatus designs and processing techniques for manufacturing amorphous alloy ribbons have been developed with consideration for optimization of heat transfer and fluid dynamics. In other words, in various continuous casting processes used in the manufacture of rapidly solidified alloys, the important objectives are (i) to maximize the average quench rate and (ii) to control the geometrical dimensions and finish

of the cast product. The melt jet upon impingement on the circumferential surface of a rapidly rotating wheel, forms a puddle and then departs under the action of radial acceleration. During its period of contact with the substrate, the melt cools rapidly and its viscosity increases. The kinetic energy of the melt jet causes spreading of the liquid on the substrate to an extent determined by melt surface tension and other fluid properties as well as momentum balance on impact. The width and length of the puddle, which are governed by the nozzle size, velocity of the melt jet, and the rapid substrate velocity, determine the width w , and thickness t , of the ribbon. Therefore the ribbon width may be increased by increasing the melt jet diameter and velocity, and by using steep angle of melt jet incidence on the moving substrate surface. Ribbon thickness may be reduced by increasing the substrate surface velocity, reducing the melt jet diameter and velocity, and by using a steep angle of incidence of melt jet on the moving substrate surface. Excessively high melt jet velocity may result in thickened ribbon edges, while extremely high substrate velocities may result in continuously-cast product having serrated edges and surface perforations.

The high surface tensions, low viscosities of the metallic melts, and interaction between the gas boundary layer on the moving substrate surface and the melt puddle, cause significant puddle turbulence and subsequent ribbon edge serrations and surface perforations. The turbulence in the puddle may greatly be smoothed by impinging the melt jet with a significant component of motion along the direction of substrate motion or by quenching the melt in a He atmosphere or in a crude vacuum (133). The ribbon width can be increased to strip or sheet dimensions by using a long slit nozzle or by employing a series of

uniformly spaced nozzles. In each case it is necessary to maintain a stable, elongated melt puddle in contact with rapidly moving substrate surface, such that merging of the individual melt puddles yields the desired elongated composite puddle. The use of multiple nozzles has yielded a ribbon as wide as 10 mm (133, 134). A common characteristic of glassy alloy ribbons manufactured by this method is the appearance of a line texture along the length of the ribbon.

The initial quench rate of a twin-roller quenching method is greater than in a single roller method; however, contact time or distance over which the ribbon touches the substrate is extremely short, thereby rendering no significant improvement in overall quench rate. Although the twin-roller method produces ribbons which are flat and have parallel surfaces, undesirable cold work of the ribbon during casting as well as in-plane curvature is found to occur.

The rates attained in any quenching process are determined by the thickness of the product and the mode of heat transfer between the melt and the quenching medium. The quenching rate achieved varies with t^{-n} with $n=1$ for Newtonian and $n=2$ for ideal quenching. Ideal cooling is achieved when the Nusselt number, $Nu (=hd/k)$, is greater than 30, while $Nu < 1$, Newtonian cooling is obtained. Here h is the heat transfer coefficient, and k is the thermal conductivity of the melt. Figure 7 shows predicted cooling rate q as a function of t and h (135, 136). Comparison of experimental data with calculated values of Figure 7 reveals that (i) in case of splat quenched foils (< 1 m thick) the mode of cooling is Newtonian and rates of cooling are very sensitive to the thermal contact with substrate; (ii) for melt-spun ribbons ($\sim 20 \mu\text{m}$ thick) q is less sensitive to thermal contact when $h \geq 10 \text{ Wm}^2/\text{s}$.

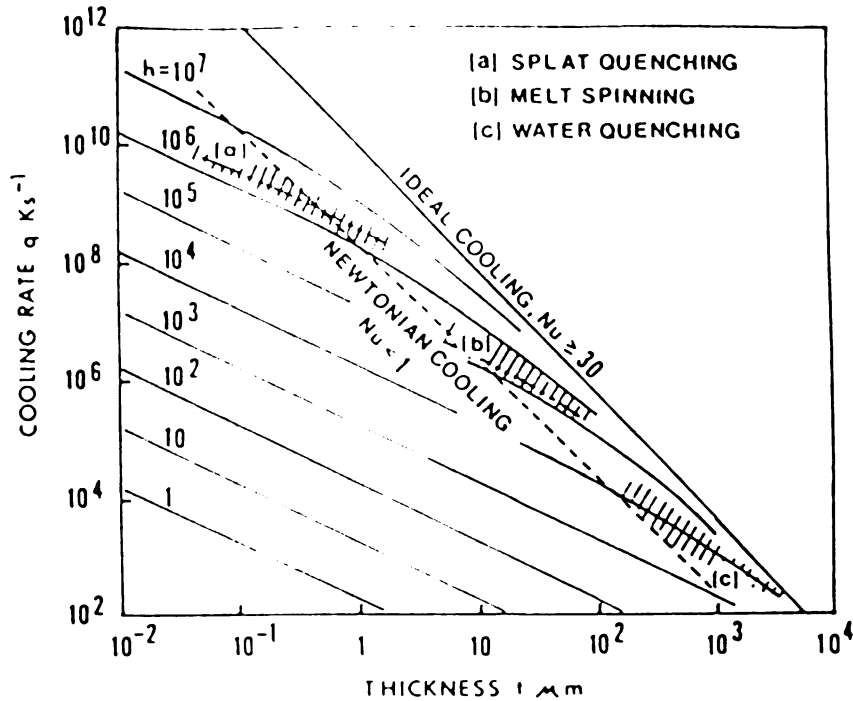


Figure 7: Predicted cooling rate as a function of section thickness t , and heat transfer coefficient h ($\text{W/m}^2\text{s}^1$) (135,136).

Non-wetting of the substrate by the melt contamination or oxide formation on the substrate, however, may greatly reduce the rates of quenching and hamper glass formation.

The quenching rates attained are $\sim 10^9$ K/s for splat quenching, $\sim 10^6$ K/s for melt quenching, and 10^3 K/s for the water quenching processes. The maximum thickness t_{max} obtainable for glassy ribbons is determined by the thermal diffusivities of the melt D_t , and the critical quenching rate q_{cr} , required for glass formation. For ideal quenching: $t_{\text{max}} \sim (D_t T_m / q_{\text{cr}})^{1/2}$ where T_m is melting temperature. For most alloy liquids, $D_t = 0.2$ cm^2/s , $T_m = 1000$ K, and $t_{\text{max}} \approx 0.1$ mm for $q_{\text{cr}} = 10^6$ K/s.

2.2.4 Glass-Forming Alloys

The ability to form glass depends critically on quenching conditions. Attempts to form metallic glass from pure metallic elements have never been materialized. Computer simulations have indicated glass formation by atomic deposition (137) or by liquid quenching at rates of 10^{12} K/s (138). In practice, however, pure monatomic metal liquids have not been quenched into glasses due to failure to attain such high rates of quenching to avoid crystallization. Formation of a glassy phase is reported in literature (139), in the thinnest portion of a splat quenched Ni foil in oxidizing atmospheres. It is suggested that impurity contamination played a significant role in stabilizing the glassy phase.

Glass-forming binary alloys may be divided into three groups; transition metal or noble metal alloys containing about 10-30% semimetal (P, B, Si, C), alloys of early transition metals (Zr, Nb, Ta, Ti) and late transition metals (Fe, Co, Ni, Cu, Pd), and alloys containing IIA metals (Mg, Ca, Be). Phase diagrams of the selected systems from each group are shown in Figure 8 (140).

The first group, commonly known as metal-metalloid systems, are represented by $Au_{75}Si_{25}$, $Pd_{80}B_{20}$, $Fe_{80}B_{20}$, $Ni_{80}P_{20}$ and $Pt_{75}P_{25}$, whose glass-forming compositions fall into a narrow deep eutectic region (Figure 8a). The second group referred to as inner-transition systems (Figure 8b,c) forms glasses generally near an early transition metal composition of 60%, e.g. $Zr_{70}(Ni, Fe, Co, Pd)_{30}$, $Ti_{65}Ni_{35}$, $Nb_{60}Rh_{40}$. In alloys of Zr-Cu, Ti-Cu, Nb-Ni (141), however, glasses can be formed for a broad range of composition. The third group consisting of IIA metals is represented by Mg-Zn, Ca-Mg and Ca-Al or Ca-Zn systems (142).

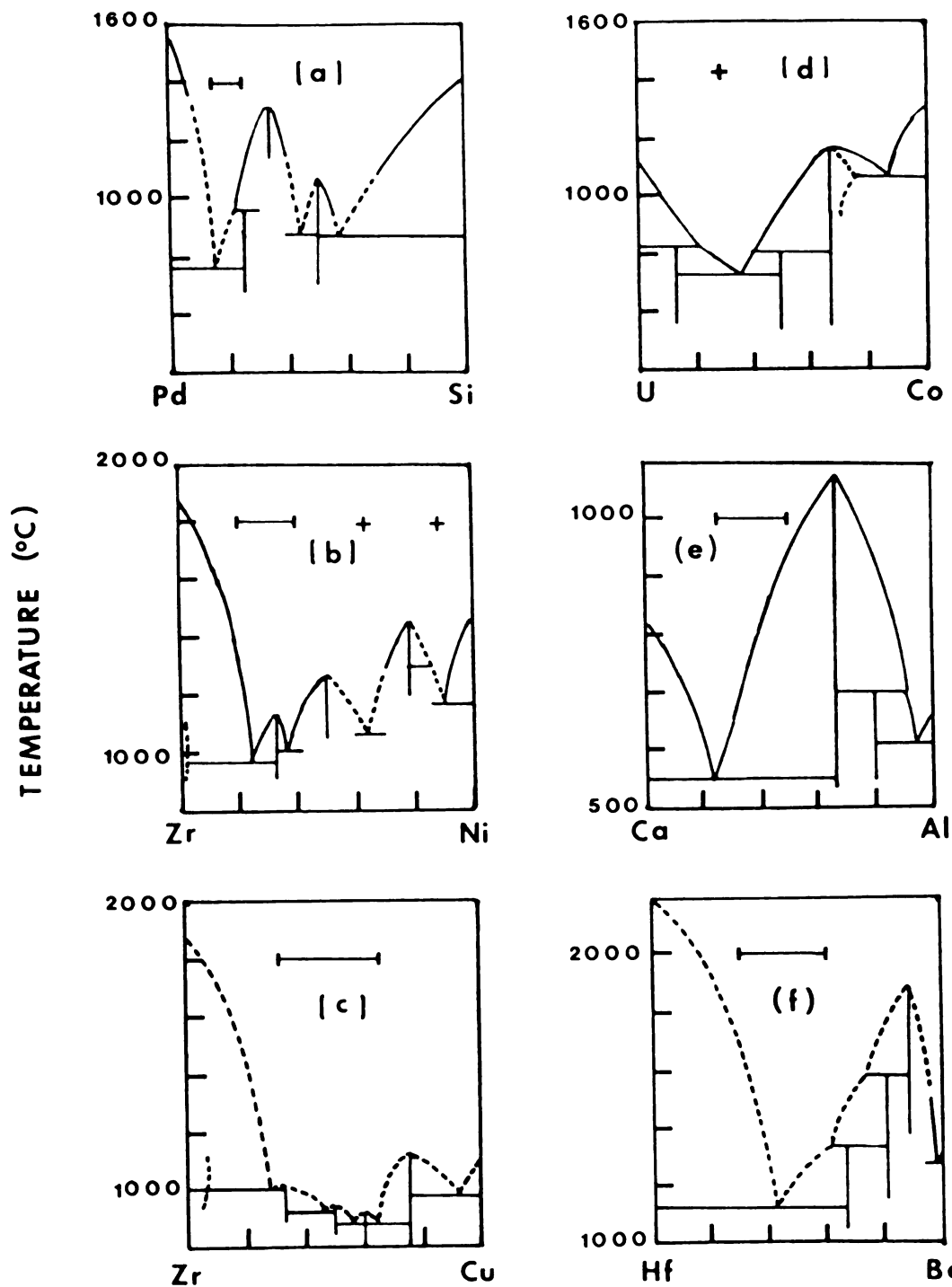


Figure 8: Representative phase diagrams of glass-forming alloy systems (140).

These alloy systems are characterized by a relatively high melting intermetallic phase of AB_2 type; e.g. $MgZn_2$, $CaMg_2$ and $CaAl_2$, participate in a relatively low melting eutectic near 40% of B element (Figure 8c). In Be-containing alloys, Ti-Be alloys form glasses in a narrow range (37-41% Be), while Zr-Be and Hf-Be alloys exhibit a wide range (30-50% Be and 30-60% Be respectively) (5).

In addition to these three types of glass-forming systems, various alloy systems have been identified which form glasses, e.g. U alloys containing 20-40% V and Cr (143), U-30% Mn, Co, Fe and Ni, and Pt-10-20% transition metal (144) (Figure 8d), Al-17% Cu (145), Al-30% Ge (146), Al-7% Cr (147), Al-7% Ni (148), La-24% Au (149), Gd-M with M = Co, Ni, Cu and Pd (150), $Y_{60}Fe_{40}$ and $Th_{50}Fe_{50}$ (151).

The common features present in all glass-forming alloys are (i) a strong interaction between the constituent atoms as indicated by a negative heat of mixing, and (ii) a low lying eutectic (Figure 8). The heats of mixing, ΔH_m , range generally from -2 to -10 K Cal (g-atom)⁻¹ for the glass-forming alloys mentioned above. The strong atomic interactions are also evident from the formation of stable intermetallic phases which play a role in a relatively low eutectic reaction. The eutectic temperatures T_e are generally about 0.6 of the melting temperature T_m as compared with $T_e/T_m = 0.8$ for eutectic systems. The additional depression of melting points for the glass-forming alloys is because of the strong atomic interaction (152).

Most binary metallic glasses, with the exception of Pd-Si, Zr-Cu, and Zr-Be systems, are not stable and crystallize at temperatures below the effective glass transition temperature. These glasses produced only as foils $\sim 40 \mu m$ thick, require a critical quenching rate of 10^5 K/s or

higher. The admixture of glass-forming binary alloys or the addition of third elements, having different atomic radii and different inter-metallic compound symmetry, enhances sharply the thermal stability and the glass-forming tendency, mainly by lowering the eutectic temperature. Ternary alloy systems, Pd-Cu-Si, Pd-Ni-P and Pt-Ni-P, have been prepared with consideration to above mentioned criteria. These glasses requiring low quenching rates (10^2 K/s) exhibit excellent thermal stability and remain glassy at the glass transition temperature for several hours. The eutectic point of ternary alloys is lowered by 50-300 K from that of the constituent binary alloys (29, 153). The increased ease of formation and thermal stability upon alloying is a common phenomenon and has been observed for many metallic glasses.

2.2.5 Factors Affecting Glass Formation

The kinetic approach indicates occurrence of a deep eutectic as a likely signal for glass formation. The efforts to correlate eutectic compositions with the liquid structure complement the kinetic approach. The first such attempt by Hume-Rothery and Anderson (154) suggests that at special compositions such as $A_{12}B$, A_5B and A_3B , eutectic structures might be most stable structurally due to low free energy. Bennett et al. (155) suggested that in transition metal-metalloid systems small and softer metalloid atoms occupy the large voids in the random dense network of large transition metal ions and stabilize the random configuration. Geometrical arrangement based on this proposal yields an alloy composition consisting 80% large metal atoms, a composition frequently observed suitable for most metal-metalloid alloys that have been produced. It was indicated (156), however, that none of the holes

were large enough to accommodate the metalloid atoms. In some cases it was observed that the glass-forming composition of the metal-metalloid system departs significantly from the predicted range, and in many cases the softer metalloid atoms are larger than the metal atoms, as in case of $\text{Pt}_{65}\text{Sb}_{35}$ (157) and $(\text{Au}, \text{Ag})_{25}\text{Pb}_{75}$ (158).

Considering the glass as a nearly free electron solid, Nagel and Tauc (159) proposed that at a composition where the Fermi level is at a minimum density of states, or where the Fermi vector $2K_f$ equals q_p , the first peak of structure vector, the glassy phase should be stabilized. Thus an alloy with valence electron concentration (VEC) $Z=1.7$ should be most stable against crystallization. At such composition in liquid alloys, electrical resistivity has a negative temperature coefficient (NTC). The Nagel and Tauc model was further modified by Guntherodt and Kunzi who suggested that glass formation would be favored for compositions which show NTC in liquid state. This VEC value and NTC criterion compare favorably with some compositions of metal-metalloid alloys, and the wide glass-forming composition range in Zr-Cu and Nb-Si systems, however, fail to justify the large difference in glass-forming tendency among alloys that satisfy the criteria. In many glassy alloys, no minimum density of states is found. For (Mn, Fe, Co, Ni)-Ge alloys the concentration ranges of NTC are centered near the equiatomic composition; however, the observed glass-forming range is near 80% metal-20% metalloid composition. These models are based on the assumption of stabilization of liquid phase and ignore the composition dependence of the stability of crystalline phase. Very little experimental evidence, as suggested by Chadwick (160), is available to argue in favor of stabilization of liquid phase. Chen (152) proposed

consideration of the destabilization of the crystalline mixture, rather than the stabilization of the glassy phase, as a criteria for predicting useful glass-forming range. Masumoto and Maddin (161) have suggested a correlation between the glass-forming elements and its position in the periodic table. Elements of different valence often participate in strong A-B bonding, which is important in promoting glass formation. Valence difference often coincides with the differences in atomic size.

Thus, so far there exists no theory of glass formation in metallic systems that is truly predictive. Appreciable atomic size differences and strong interaction of component atoms are hallmarks of deep eutectic systems and thus of potential glass-forming alloys.

2.3 Structure

To characterize the structure of the non-crystalline materials, x-ray, electron and neutron diffraction methods are commonly used. The x-ray diffraction patterns of glassy alloys consist of a series of broad diffraction maxima of decreasing intensity and increasing width with increasing Bragg angle, indicating clearly that the metallic glasses we are discussing are truly amorphous, as opposed to microcrystalline.

The structural models for amorphous solids used most frequently are quasi-crystalline model and the Bernal model. Quasi-crystalline models are heterogeneous in which the misoriented crystallites are very small and are separated by regions of less-ordered non-crystalline arrangements. Microcrystalline models for amorphous solids have been proposed for monatomic (162) as well as polyatomic (163) systems. The second model used for describing the structure of metallic glasses is

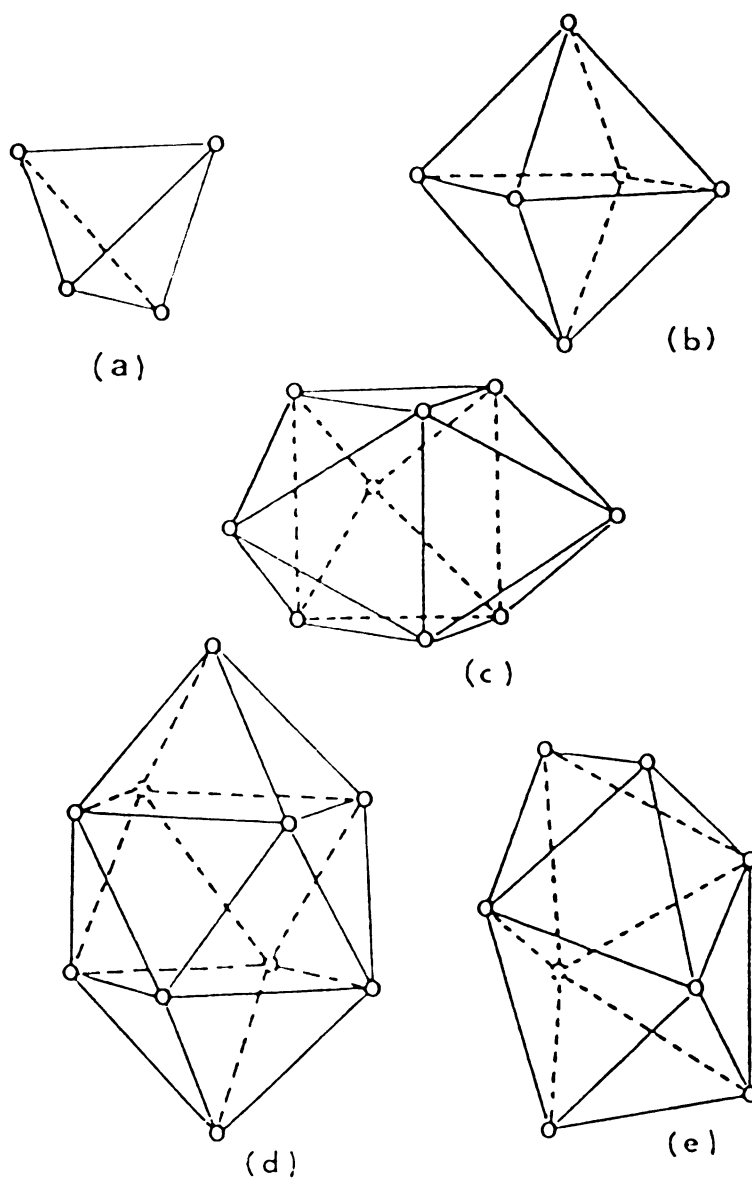


Figure 9: Bernal's idealized holes describing the topology of dense random packing: a) tetrahedron; b) octahedron; c) trigonal prism capped with three half-octahedra; d) Archimedean anti-prism capped with two half-octahedra; and e) tetragonal dodecahedron (164).

known as the dense random-packing of hard spheres model (DRPHS) and was first proposed by Bernal (164) who applied it to monatomic liquids. Later this model was modified and applied to amorphous solids (165). The hard sphere model predicts splitting of the second peak in the interference and in the atomic distribution functions that has been observed in large majority of amorphous alloys. This feature is normally prominent for amorphous solids but not for liquids, indicating at least some increase in structural order for the amorphous solid compared with the liquid state. In crystalline state, the metalloid atoms; e.g. P, B, Si and C, have smaller atomic size than the transition metal atoms. Hence the hard sphere model with two sizes of spheres was analyzed (166). Polk (167) suggested that smaller metalloid atoms fit into the "holes" of the five basic Voronoi polyhedra present in this model (Figure 9). Assuming all these holes were occupied by the metalloid atoms, the atomic fraction of the metalloid in one alloy was obtained to be 19.1%, which is remarkably close to the metalloid fraction (20 at %) observed in most metal-metalloid systems. Experimental data and model studies of metallic glasses have been reviewed extensively in the literature (156, 168). Also critical reviews of the structural models are published (169-171).

2.4 Corrosion Behavior

Results of corrosion studies on metallic glasses were first reported by Naka et al. (172, 173). It was observed that metallic glasses containing certain amount of Cr and P exhibited extremely high corrosion resistance in acid and neutral solutions such as 1 M H₂SO₄, 6% FeCl₃ and 1 N HCl. Glassy Fe₈₀P₁₃C₇ alloy, which is fairly unstable in

corrosive environments, exhibits remarkable corrosion resistance on addition of chromium. Fe-Cr-P-C glasses containing more than 8% Cr showed extremely high resistance exceeding 18Cr-8Ni stainless steel, particularly in FeCl solution in which the latter suffers pitting and crevice corrosion. This superior corrosion resistance of the Fe-Cr-P-C glasses has been attributed to the rapid formation of thick, uniform, and highly corrosion resistant passive films. Hashimoto et al. (174) found that the corrosion potential of the glassy alloys was high and showed higher reactivity as compared with the 18Cr-8Ni stainless steel, apparently due to the presence of a large amount of semimetallic elements. This high reactivity of a glassy alloy was considered responsible for promoting the rapid formation of thick and highly corrosion-resistant passive films enriched in chromium via rapid dissolution of other elements in the alloys. The high reactivity of glassy alloys also was credited for a rapid recovery of rupture sites of the passive films. Thus it was concluded that the chromium enrichment process in forming passive films enables the glassy alloy to exhibit a superior corrosion behaviour at lower Cr content as compared with 18Cr-8Ni stainless steel.

The rate of formation of chromium-enriched passive film in the active state depends on the rate of active dissolution. Consequently the effectiveness of Fe-Cr-based glasses simply reflects whether the individual element accelerates the active dissolution. The alloys containing P and C have the highest corrosion potential and thus are the best corrosion-resistive while the alloys with Si and B are less reactive and exhibit poor corrosion resistance (175).

Masumoto and Hashimoto (176) observed that the corrosion rate of

the Fe-Cr glassy alloy progressively decreased by addition of silicon, boron, carbon and phosphorus in 0.1 N H_2SO_4 ; the progression was boron, carbon, silicon and phosphorus in 3% NaCl. The addition of chromium without phosphorus to Fe-based glassy alloys (e.g. Fe-10Cr-13P-7C and Fe-10Cr-13P-7Si) was observed to be ineffective in improving their corrosion resistance properties (175, 177). On the other hand, the glassy Fe-Cr alloys with phosphorus revealed a negligible corrosion rate in all cases except the alloy containing silicon.

The addition of various metallic elements such as Ni, Mo, W, etc., to amorphous Fe-P-C alloys improved the corrosion resistance of the alloys. The effects of additive metallic elements in improving corrosion resistance were observed to be remarkable when a small amount of chromium was present, $\sim 3\%$ Cr, in the Fe-P-C alloys (178). A small amount of Mo addition, $< 3\%$, to Fe-P-C alloys was more effective than a chromium additive in reducing the corrosion rates (179, 180). Corrosion behaviors of glassy nickel-base alloys were found to be similar to the glassy iron-base alloys (176).

2.5 Magnetic Properties

The existence of long-range ferromagnetic ordering in glassy alloys may appear striking; however, ferromagnetism is supposed to arise from nearest neighbor interactions. The very short-range order structure in a glassy state does not differ significantly from that in a corresponding crystalline material. Glassy alloys are not structurally and magnetically isotropic as evidenced by the presence of macroscopic magnetic anisotropy. Residual strain (181), field annealing (182) or directional ordering during solidification (183) induces anisotropies which determine

the domain structure of the glasses and thus their magnetic behavior. The domain structures in glassy alloys are essentially similar to those observed in crystalline counterparts. Most models developed for crystalline magnetic materials to describe the static and dynamic properties are shown to be applicable to glassy alloys (184-186).

Magnetic properties of various metallic glasses have been studied extensively (34,44,50,181-217). Amorphous alloys based on iron or cobalt are ferromagnetic at room temperature (186) and generally have coercive fields less than 100 mOe in the as-cast state. These low coercivities are the result of the high homogeneity of the amorphous structure which has no grain boundaries or precipitate particles to act as pinning centers for domain walls. The lowest coercive fields and highest permeabilities are attained in alloys with zero magnetostriction. The magnetostriction is small only in alloys of high Co and/or Ni content (182). The Ni-rich members of this series have T_C below room temperature (187) and are not of much engineering interest, and the Co-rich alloys are too expensive for use in large equipment. Iron-based metallic glasses have been the focus on intensive research because of their high magnetic inductions, soft magnetic properties and potentially low raw material costs. For practical applications as soft magnetic materials the ribbon form is most useful. Hence, studies of magnetic behaviour of glassy alloys were initially centered on glassy ribbons prepared by continuous melt-spinning (181,182,188).

Of the iron-metalloid binaries, only Fe-B and Fe-P have been successfully prepared in ribbon form. Since Fe-B binary exhibited higher T_C ($=377^\circ\text{C}$) and magnetic moment per iron atom, further studies were concentrated on $\text{Fe}_{80}\text{B}_{20}$ glassy alloy. $\text{Fe}_{80}\text{B}_{20}$ alloy showed good

soft magnetic properties, i.e., high permeability, low coercivity and high room temperature saturation magnetization. In addition, high resistivity and low gage of the glassy alloy made it suitable for use as a core material in power transformers. Table I lists the saturation induction, coercivity, remanence, and permeability of toroidal $\text{Fe}_{80}\text{B}_{20}$ samples, as well as handbook values for commercial alloys (189): 50% Ni-Fe and grain oriented Fe-3.2% Si alloy (189). The properties of the field-annealed toroid of $\text{Fe}_{80}\text{B}_{20}$ glassy ribbons compare favorably with those of the commercial alloys. Although this alloy has B_S value lower than grain-oriented Fe-Si alloys for which B_S reaches ~ 20 kG, its a.c. core loss at 60 Hz is one-third that of the crystalline counterpart. Thus further efforts were directed to attempt various compositional modifications of $\text{Fe}_{80}\text{B}_{20}$ glass in order to find other suitable high induction alloys.

Table I: Some properties of $\text{Fe}_{80}\text{B}_{20}$ glass and comparable commercial materials.

	$\text{Fe}_{80}\text{B}_{20}$ glass toroid		Commercial 2-mil alloys	
	As-cast	field annealed	50% Ni-Fe	Oriented Si-Fe
$4\pi M_s$ (kG)	16.0	16.0	16.0	19.7
H_C (Oe)	0.08	0.04	0.1	0.5
B_r (kG)	8.15	12.3	14.6	14.4
μ (20)	1700.00	4000.00	500.00	1000.00
$\mu_{\max}(\frac{B}{H})$	102000.00	320000.00	146000.00	29000.00
Loss(W/kg) 60 Hz, 13kG	0.53	0.77	1.5
Loss(W/kg) 1 kHz, 1kG	0.33	0.10	0.22	0.26

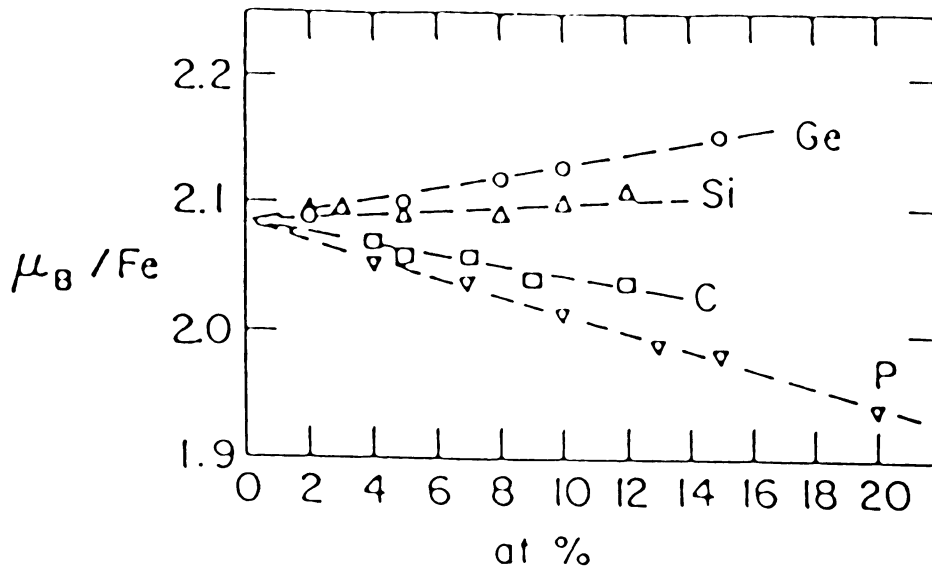


Figure 10: Moment per Fe atom in amorphous $Fe_{80}B_{20}$ alloys as B is replaced by C, Si, P or Ge (192).

The addition of metalloids is expected to alter magnetic moment, μ_B , and the Curie temperature, T_C , of the glassy alloys resulting from the modification of local atomic environment. In Fe-based glassy alloys, replacing Fe with Co or Ni in general reduces the moment. Mizoguchi et al. (190) found that replacing either Fe or Co with Mn, Cr and Mo drastically reduces both μ_B and T_C . The usual assumption is that the moments of these atoms align antiferromagnetically with the dominant iron moment. The influence of composition on T_C has been investigated by Chen et al. (191) for a number of glassy alloys systems. It was reported that the addition of a metalloid which expands Fe-Fe interatomic distance raises T_C while the increase in Co-Co and Ni-Ni pair distances lowers T_C .

The effect of replacing B by other metalloids has been systematically investigated by Kazama et al. (192) with the results shown in Figure 10. It is seen that Ge and Si increase the moment per atom, but

C and P decrease it. When these results are recalculated in terms of moment per gram, all the substitutions lower the moment, but Si and C have only a small effect.

The effect of replacing part of B by C on magnetic properties has been investigated by Hatta et al. (193), Luborsky et al. (194) and Mitera et al. (195). It was found that replacing B by C reduced the thermal stability in an alloy having more than 80 at % Fe, increased the T_C slightly, and decreased the slope of the magnetization-temperature curve. The coercivity was always higher for the ternary Fe-B-C alloys than for the binary Fe-B alloys. The coercivity, both as-cast and after stress-relief annealing, increased on replacement of B by C. The optimum composition was determined to be $Fe_{81}B_{13}C_6$. Thus, although the low-temperature saturation magnetization decreased on replacement of B by C, as expected, the room temperature magnetization exhibited a broad ridge of constant saturation magnetization per gram extending from approximately $Fe_{80}B_{20}$ to approximately $Fe_{83}B_{11}C_6$.

Replacement of B by Si has been investigated by O'Handley et al. (196) and by Luborsky et al. (197). Luborsky et al. (197) observed that T_C increased slightly on replacement of boron by silicon. The crystallization temperature increased with increasing silicon and with decreasing iron and boron content. The alloys with silicon were generally easier to prepare in the amorphous state than binary Fe-B alloys. Also, Fe-B-Si alloys exhibited higher saturation magnetization, with minimum H and hence lowest losses between compositions $Fe_{81}B_{17}Si_2$ and $Fe_{82}B_{12}Si_6$.

Hatta et al. (198) and Mitera et al. (195) have also studied the effects of replacing boron by a combination of silicon and carbon. The

results showed that the stability of the Fe-B-Si-C alloys is greatly improved. Starting from $\text{Fe}_{81}\text{B}_{13}\text{C}_6$ Mitera et al. (195) replaced carbon by silicon upto $\text{Fe}_{81}\text{B}_{13}\text{C}_1\text{Si}_5$ and found a very slight linear drop in σ_{rt} (about 1%) and a modest increase (23 K) in T_c occurring mainly with the few % silicon added. It was also observed that silicon addition is very effective in reducing coercive force and core loss as well as improving magnetic stability during aging at low temperatures. The composition, optimally balanced between coercive force and saturation magnetization, which gives desirable soft magnetic properties, was identified to be $\text{Fe}_{81}\text{B}_{13}\text{Si}_4\text{C}_2$. The results of this study agree nearly with those reported by Luborsky and Walter (199). Luborsky and Walter (199) obtained maximum saturation magnetization for an alloy composition of $\text{Fe}_{81}\text{B}_{13}\text{Si}_{2.5}\text{C}_{2.5}$. The crystallization temperature, Curie temperature, saturation magnetization, and density all appeared to be average values of the ternary Fe-B-C and Fe-B-Si properties. Maximum saturation magnetization obtained in various amorphous alloy systems is summarized in Table II. The best properties reported for $\text{Fe}_{81}\text{B}_{13}\text{Si}_4\text{C}_2$ composition are $\sigma_s(\text{R.T.}) = 176 \text{ emu/g}$, $H_c = 8 \text{ mOe}$, $B_r/B_{100} = 0.88$ and the core loss,

Table II: Maximum Saturation Magnetization at Room Temperature

Alloy system	As-cast		Annealed		References
	σ_s emu/g	$4\pi M_s$ kG	σ_s emu/g	$4\pi M_s$ kG	
Fe-B	130	16.7	184	17.0	(200)
Fe-B-C	180	16.9	184	17.3	(194,201)
Fe-B-Si	170	16.5	183	16.9	(197)
Fe-B-Si-C	182	17.0	186	17.3	(199)

$w/f = 8 \times 10^{-4}$ W-sec/kg (at 12.5 kG and 50 Hz). This alloy, however, has maximum value of magnetostriction ($\sim 50 \times 10^{-6}$) reported for any amorphous transition metal alloy. Thus, small magnetostriction is clearly not an absolute requirement for low H_c . Due to its lowest core loss, this alloy has found application in low and high frequency transformers as a core material, as well as in magnetic amplifiers.

Investigations on Be additions up to 2-4 at % to Fe-B system have also been reported (202). Such additions can occupy the transition metal sites when Be is introduced in glassy Fe-B alloys. This leads to a drastic reduction of the saturation magnetostriction without reducing the magnetization. Substitution effect studies of Fe by Cr in amorphous Fe-Si-B alloys (203) showed that Cr decreases Curie temperature quite greatly, but it also slightly increases T_x . Cr improves soft magnetic properties, namely it decreases coercive force and core loss, and increases initial magnetic permeability.

2.5.1 Effect of Deformation and Magnetic Annealing

A quantity of considerable engineering importance is the power loss per cycle under a.c. excitation. Generally it is found that the losses in as-prepared glassy alloys are somewhat higher than in conventional crystalline permalloys, but after a suitable heat treatment the glassy alloys are superior to the crystalline alloys. If the high-induction (high Fe-content) glassy alloys are compared with conventional crystalline Si-Fe, the glassy alloys are substantially lower in losses except at values of maximum induction approaching the saturation limit. Thus, the development of the excellent soft magnetic properties of glassy

alloy ribbons requires annealing at temperatures too low, or for times too short, to cause crystallization and cooling in a magnetic field. The annealing treatment relieves the stresses resulting from the casting operation, and cooling in the magnetic field induces a uniaxial anisotropy in the ribbon plane. Being amorphous, the ribbons lack the magnetocrystalline anisotropy of crystalline materials. Magnetic annealing of glassy alloys is effective in reducing the stress anisotropy to lower values. It also substantially reduces coercive force, increases hysteresis loop squareness and thereby increases permeability and decreases losses. Magnetic annealing also increases T_C of glassy alloys. The property changes during annealing are primarily associated with changes in internal stresses originally present as a result of the quenching and preparation of the ribbon. Annealing in demagnetized state deteriorates magnetic properties.

Although the losses in glassy alloys are low, the classical eddy current loss component is only 1-15% of the measured eddy current loss (204,205). (Eddy current losses vary inversely with resistivity and linearly with the square of the thickness). The large "anomalous" eddy current loss is attributed to the relatively coarse domain structure of glassy alloys (184). The domain structure of a glassy alloy ribbon in the stress-relief condition is composed of 180 domains parallel to the ribbon axis when the applied magnetic field is parallel to sheet thickness. The ratio of domain wall spacing to sheet thickness is observed to be 20 to 40 (206). This larger ratio than that found in crystalline metals contributes to high anomalous losses in the ferromagnetic amorphous alloys. Presence of domain walls, inferred from the large Barkhausen discontinuities observed in d.c. hysteresis loops, can

be observed by the Bitter technique using colloidal magnetic particles (207), by magneto-optical Kerr effect (208), and by scanning electron microscopy (183).

O'Handly et al. (209) observed a reduction in core loss by annealing in a crossed magnetic field (one field parallel to the ribbon axis and the other perpendicular to the plane of the sample). Similarly, Luborsky et al. (34) annealed in either a parallel or perpendicular field to control the magnitude of the anisotropy (in both cases the field was in the plane of the sample). The resultant losses were found to be sensitive to the magnitude and the direction of the induced anisotropy. Fujimori et al. (210) observed that magnetic annealing in the plane of the strip but oblique to the major strip axis caused a decrease in losses within the frequency range of 50 Hz-20 kHz. Domain observations confirmed that the oblique magnetic anneal resulted in an easy direction of magnetization at an angle to the strip axis and a general decrease of the domain wall spacing. Thus, domain refinement reduced high anomalous loss.

Washko et al. (211) investigated the origin of losses during a.c. excitation in Metglas 2605SC. The calculated losses, using equilibrium domain spacing and measured d.c. hysteresis losses, account for 70-90% of the total core loss. Results of this study thus conclude that losses are dominated by hysteresis losses in the material. The results of the study by Krause and Werner (206) on Metglas 2605SC show that domain refinement by scratching, annealing in a transverse field, precipitation of crystallites, and applying a bias transverse field improve the high frequency magnetic properties. Thus, there appears to be disagreement as to what factor contributes most to the core losses of glassy alloys.

However, power losses of a glassy alloy, except at values of maximum induction approaching the saturation limit, are considerably lower than the conventional grain-oriented silicon steels.

Liebermann et al. (212) have studied the effects of annealing in air on various properties of several glassy alloys. All the alloys studied showed a steady increase in T_C on annealing at low temperatures, but some compositions showed a smaller increase in T_C on annealing near the crystallization temperature than on annealing at lower temperatures. All the alloys showed a clearly measurable decrease in length on annealing. Annealing experiments on the shape of 60 Hz hysteresis loops showed a decrease in anisotropy associated with non-uniform internal stresses, but in some cases also showed the slow development of a fairly strong uniaxial anisotropy with its easy axis perpendicular to the ribbon axis. This uniaxial anisotropy was attributed to the development of an oxide layer during annealing, which in turn produced uniform compressive stress due to differential thermal contraction and therefore a stress-magnetostriction anisotropy.

Effects of deformation and annealing on magnetic properties of $Fe_{80}B_{20}$ (50) and $Fe_{40}Ni_{40}P_{14}B_6$ (50,213) are reported in the literature. Williams and Egami (50) observed that deformation increases anisotropy and stress-relief rate, while annealing reduces it. Luborsky et al. (213) showed that cold-rolling of glassy alloy ribbon results in a large increase in coercive force and a large decrease in magnetization in low fields. This was attributed to both slip-like structures developed by rolling and strain magnetostriction-induced anisotropy. On annealing the rolled ribbon to temperatures below its T_x , the magnetic properties recovered to values obtained on annealing as-cast ribbon, but higher

temperatures were required. The rolled ribbon showed no evidence for structural change, or change in the glass or crystallization temperatures. Studies of effects of mechanical deformation on magnetic properties of $\text{Fe}_{40}\text{Ni}_{40}\text{P}_{14}\text{B}_6$, $\text{Fe}_{40}\text{Ni}_{40}\text{B}_{20}$ and $\text{Co}_{50}\text{Ni}_{20}\text{Fe}_6\text{Si}_{12}\text{B}_{12}$ by Gibbs et al. (214) also showed that as the amount of thickness reduction increased, coercive force increased. However, the large increase in the coercivity after rolling was thought to be due to an increase in the domain wall pinning interaction. Chen et al. (44) studied the effect of structural relaxation on Curie temperatures of Fe-based metallic glasses. It was observed that the T_c of these glasses increased monotonically with the annealing temperature T_a .

2.6 Mechanical Properties

Metallic glasses exhibit unique properties arising from unique characteristics of the glassy state. Though metallic glasses in tensile deformation at room temperature seem macroscopically brittle, they are inherently plastic to a considerable degree as has been demonstrated with $\text{Pd}_{80}\text{Si}_{20}$ by bending of thin ribbons (1,25,218) and compression of short rods (219-221). Fracture in metallic glasses proceeds by highly localized shear deformations, which is unlike the brittle fracture commonly observed in non-metallic glasses (e.g. silicate glasses). The elastic moduli of glassy metals are about two-thirds those of typical crystalline transition metals. Because of the lack of translational periodicity, the fracture strength of glassy metals approaches the theoretical strength ($\sigma_f \approx E/50$) as compared with observed for crystalline metals. Metallic glasses exhibit cycle dependent, i.e. not time dependent, fatigue.

2.6.1 Density and Thermal expansion

In Ni-P (102) and Pd-Cu-Si (222) metallic glasses density was observed to vary linearly with alloy composition, whereas for (Pd,Ni)-P (223) and Fe-B (224) glasses negative deviation from linearity was observed. The density in glassy alloys is usually about 1-2% less than corresponding crystalline alloys.

The volume change associated with structural relaxation is 0.5% (223). The volumetric thermal expansivity $\beta = (1/V)dV/dT$, of most glassy metals is approximately equal to the corresponding crystalline counterpart. The volume change associated with crystallization of metallic glasses is $\sim 1\%$. A number of ferromagnetic metallic glasses exhibit spontaneous volume magnetostriction near the Curie temperature. The magnetostriction is large in Fe-based glassy alloys and increases with decreasing metalloid content. The thermal expansion coefficient is negative in $Fe_{91}B_9$ and becomes positive for the higher boron-containing alloy $Fe_{83}B_{17}$.

2.6.2 Elastic Constants

The Young's modulus E and shear stiffness μ are generally lower by 20-40% but the bulk modulus K by only $\sim 7\%$ in as-quenched glassy alloys than in the crystalline state (225). The relatively large decrease in shear stiffness in the glassy state has been attributed to the inter-atomic shear displacements inherent in a disordered structure (226,227). The shear stiffness softening $\Delta\mu_s$ reduces considerably upon structural relaxation. The difference in shear stiffness of a completely relaxed glassy alloy and its crystalline counterpart is small ($<10\%$). The large

observed in as-quenched glassy alloys is due to frozen-in excess volume (27). The increase in E associated with the decrease in volume V during structural relaxation is large ($\sim 15\%$) and is comparable to that accompanying crystallization ($\sim 17\%$). The Young's modulus of metal-metalloid glasses, $(\text{Pd}_{1-x}\text{Ni}_x)_{80}\text{P}_{20}$ (228), $[\text{Fe}_{1-x}(\text{Ni},\text{Co})_x]_{75}\text{P}_{16}\text{B}_6\text{Al}_3$ (229), and $[\text{Fe}_{1-x}(\text{Ni},\text{Co})_x]_{80}\text{B}_{20}$ (230) is found to show a positive deviation with x from a linearity. The increased E in glassy alloys is correlated to the magnetic ordering by Chou (229). The influence of magnetic ordering, however, is claimed to be insignificant in a ferromagnetic glass (231). Chen and Krause (232) have observed that the Young's modulus E of metal-metalloid glasses increases with boron content, however, is independent of phosphorus content. E decreases in order (Fe,Co), (Pd, Ni) and Pt glasses while the bulk modulus of the corresponding crystalline metals, increases in that order.

2.6.3 Anelasticity

Metallic glasses exhibit viscoelastic behaviour. The glass deforms instantaneously upon applying tensile stress, followed by time dependent reversible deformation and steady-state viscous flow. The time required for attaining a steady flow is of the order of the structural relaxation time. The recoverable anelastic compliance, J_a at a stress level of ~ 1 MPa in Pd-Si (21) is small at low temperature (of the order of the elastic compliance) but increases rapidly in a narrow temperature range when viscosities reach 10^{12} P. J_a becomes as high as several hundreds times the elastic compliance. In this temperature range both isothermal J_a and η of the glass remain constant at small stress $\sigma \leq 1$ MPa but decrease at a higher stress i.e. the glass becomes non-Newtonian. The

total anelastic strain, $\epsilon_a = J_a \sigma$, approaches a constant value $\sim 10^{-2}$. Masumoto and Maddin (1) reported for a $\text{Pd}_{80}\text{Si}_{20}$ glass a relatively small $\epsilon_a = 10^{-3}$ at 100°C (far below $T_g = 370^\circ\text{C}$) but a large value of $\epsilon_a = 10^{-2}$ at about 200°C . The high anelastic strain implies the occurrence of a considerable directional structural ordering. Anelastic behaviour of Pd-Au-Si (32) was examined through internal friction methods. The study has indicated that the internal friction of the amorphous Pd-Au-Si alloy increases exponentially above 150°C suggesting that structural relaxation occurs at temperatures far below the glass transition temperature (about 370°C).

2.6.3.1 Thermoelastic Behaviour

Elastic relaxation may originate from the change in temperature caused during flexural vibration. Berry and Pritchett (43) obtained from thermoelastic relaxation measurements in glassy alloys the thermal diffusivities $D_{th} = 0.05 \text{ cm}^2/\text{s}$ for $\text{Pd}_{82}\text{Si}_{18}$ and 0.012 for $\text{Fe}_{75}\text{P}_{15}\text{C}_{10}$ which are only one-half and one-third of those for the crystalline phase(s). This is consistent with the higher electrical and thus thermal resistivity in the glassy state.

2.6.3.2 Magnetoelastic behaviour

When a substance is exposed to magnetic field, its dimensions change. This effect is called magnetostriction. The fractional change in length, $\lambda = \Delta l/l$, measured at saturation is called saturation magnetostriction, λ_s . Magnetostriction occurs in all pure substances. However, even in strongly magnetic substances, the effect is small: λ_s

is
pos
re
not
(12
You
ori
an
an
na
199
at
ef
ca
co
to
re
th
al
17
va
12
10
Pa

is typically of the order of 10^{-5} . The iron-rich glasses show large positive magnetostrictions, $\lambda_S = (20-40) \times 10^{-6}$ (182,233), while λ_S is negative in Co glasses. In the Fe-Co system $\lambda_S = 0$ occurs at approximately the Fe-Co ratio (~ 0.05) relatively independent of glass formers (234,235). The addition of Ni to an Fe alloy decreases λ_S .

One of the consequences of magnetostriction is dependence of Young's modulus E of a material on its state of magnetization. When an originally demagnetized specimen is saturated, its modulus increases by an amount ΔE . The value of ΔE effect, $(E_S - E_d)/E_S$, is about 0.06 for Ni and less than 0.01 for Fe. The striking ΔE effect in certain ferromagnetic metallic glasses was first reported by Berry and Pritchett (43, 236). The ΔE effects in metallic glasses can be large and are measured at room temperature with moderate magnetic field ~ 5 Oe. The large ΔE effect can not only reduce the elastic stiffness of materials but also can significantly alter or even reverse the sign of the temperature coefficient $(1/E)dE/dT$ (237). The magnitude and field dependence of the ΔE effect can be varied considerably by prior magnetic annealing that reduces internal stress and induces a uniaxial magnetic anisotropy in the specimen. The maximum ΔE effect of metallic glasses is exceptionally large, ~ 0.4 , for the $Fe_{40}Ni_{40}P_{14}B_6$, ~ 0.8 for $Fe_{75}P_{15}C_{10}$ and $Fe_{80}P_{13}C_7$ (239) and ~ 1.9 for $Fe_{78}Si_{10}B_{12}$ (238). In the as-quenched state the value of ΔE effect is small (< 0.1) for Fe-based metallic glasses. As Ni replaces Fe, the ΔE effect decreases in magnitude and the stress level required for saturation also decreases, as a result of decreasing magnetostriction and magnetic moment.

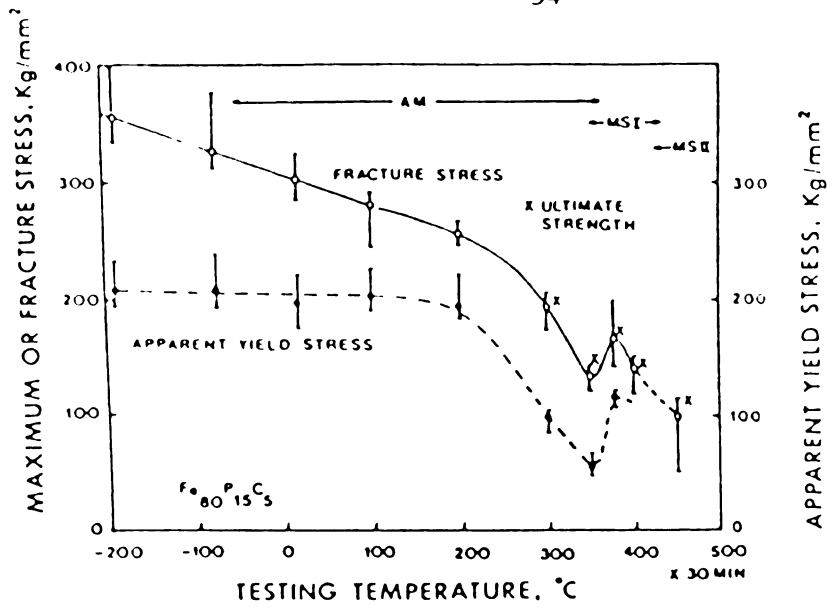


Figure 11: Temperature dependences of apparent yield and tensile strengths for amorphous Fe-P-C alloy (1).

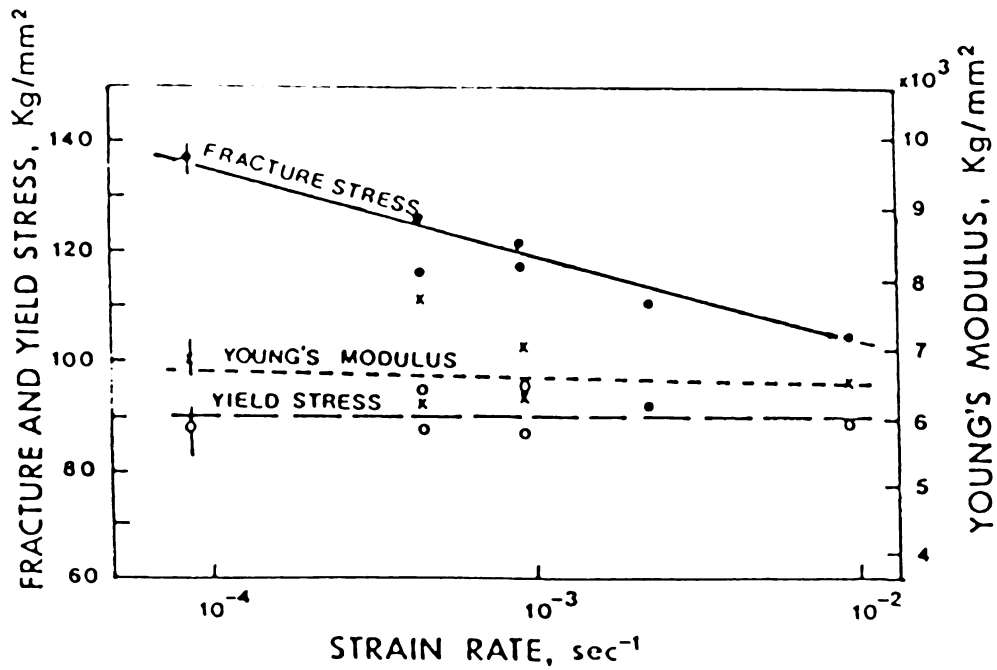


Figure 12: Relationship between the strain rate and strength properties of amorphous Pd-Si alloys (25).

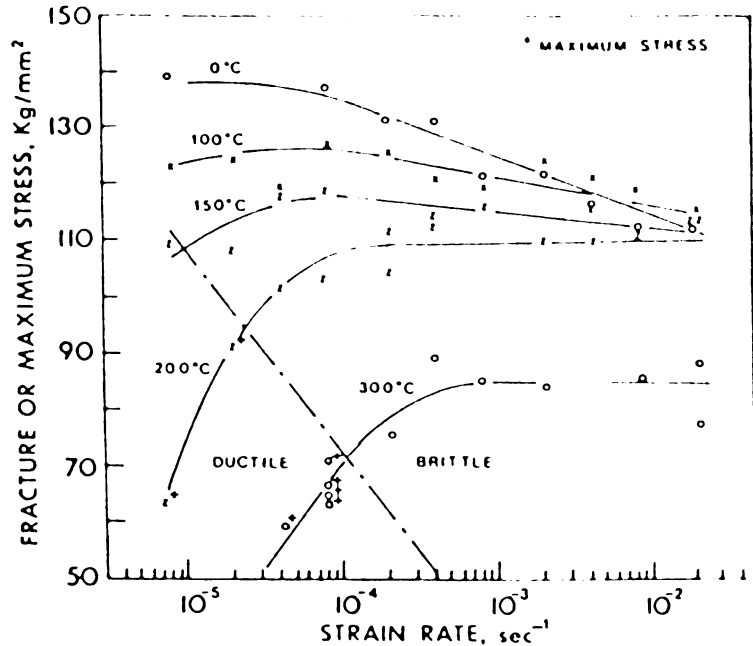


Figure 13: Effect of strain rate on the fracture stress at various temperatures (25).

2.6.4 Strength and Hardness

Metallic glasses exhibit a very high fracture strength and a high fracture toughness at temperatures well below T_g . For Ni- and Fe-based alloys tensile strengths of 140 kg/mm^2 (239) and 310 Kg/mm^2 (161) have been reported. Fracture strength $\sigma_f \approx 370 \text{ Kg/mm}^2$ exhibited by $\text{Fe}_{80}\text{B}_{20}$ metallic glass (240) is much higher than that for the conventional highest strength steels (maraging steel and a hard drawn piano wire). Such high strength in glassy alloys is in sharp contrast with that for the common non-metallic glasses.

It has been reported that temperature dependence of the tensile strength for the amorphous state is, in general, higher than for the fully crystallized state (after annealing), and the strength decreases sharply at temperatures well below the glass transition temperature, T_g

Table III: Mechanical properties of metallic glasses; (a) Vicker's hardness H_v (kgmm^{-2}), fracture strength σ_f (kgmm^{-2}), Young's modulus E ($\times 1000 \text{ kgmm}^{-2}$).

	$H_v^{(b)}$	σ_f	σ_y	H/σ_f	H/σ_y	$E^{(c)}$	E/σ_f	E/σ_y
$\text{Pd}_{77}\text{Cu}_6\text{Si}_{17}$	455	157	-	2.91	-	9.3	59	-
$\text{Pd}_{77.5}\text{Cu}_6\text{Si}_{16.5}$	498	-	157	-	3.17	8.97	-	-
$\text{Pd}_{64}\text{Ni}_{16}\text{P}_{20}$	452	160	-	2.83	-	9.3	58.95	-
$\text{Pd}_{16}\text{Ni}_{64}\text{P}_{20}$	541	180	-	3.01	-	10.6	58.9	-
$\text{Pt}_{75}\text{P}_{25}$	344	-	-	-	-	9.3	-	-
$\text{Fe}_{75}\text{B}_{25}$	1314	-	-	-	-	17.9	-	-
$\text{Fe}_{80}\text{B}_{20}$	1100	-	370	-	2.97	16.9	-	45
$\text{Fe}_{80}\text{P}_{16}\text{C}_3\text{B}_1$	835	-	249	-	3.35	13.8	-	55.4
$\text{Zr}_{50}\text{Cu}_{50}$	580	-	-	-	-	8.51	-	-
$\text{Ti}_{50}\text{Cu}_{50}$	610	-	-	-	-	10.8	-	-
$\text{Fe}_{80}\text{P}_{20}$	755	-	236	-	3.2	13.3	-	56.4
$\text{Pd}_{40}\text{Ni}_{40}\text{P}_{20}$	452	-	158	-	2.97	10.0	-	63.3

(a) Data obtained from literature. See refs. 5, 245 and 246.

(b) Accurate to $\pm 5\%$

(c) Accurate to $\pm 2\%$

(1,241) (Figure 11). Masumoto and Maddin (25) have shown that as the strain rate decreases the fracture stress increases (Figure 12). This behaviour is in contrast with the general strength properties of crystalline metals. The effect of temperature and strain rate on the fracture stress and mode is shown in Figure 13 (25). The effect of temperature on flow and fracture of various metallic glasses is summarized by Pampillo (221).

The hardness H_v , fracture strength σ_f , Young's modulus E , H_v / σ_f and E / σ_f of some typical metallic glasses are listed in Table III. An indication of plastic strength of a material is given by measurement of its microhardness (242). For crystalline metals, the ratio of hardness (Vickers / 136° diamond pyramid) to yield stress is ≈ 3 . As metallic glasses do not work harden, their tensile strengths must be equal to or less than their yield strengths. Metallic glass Fe₈₀B₂₀ which shows remarkable strength has the H / σ_f value close to the theoretical value. The ratio $E / \sigma_f \sim 50$ of metallic glasses may be compared with that of Fe whiskers, $E / \sigma_f \sim 15.5$ (243).

Masumoto (244) has reported that the influence of composition on H_v is similar to that on E . With increasing metalloid content (C, P, B or Si) in Fe- or Co-based glasses, H_v increases. H_v decreases in the order of Fe, Co, Ni, Pd and Pt glasses as does E .

2.6.5 Fatigue Behaviour and Toughness

The fatigue lifetime of metallic glasses Pd-Si (247), Pd-Cu-Si and Fe-Ni-P-B-Al (248) has been reported in the literature. Stress (S) versus cycle-to-failure (N) behaviour was qualitatively similar to that of other materials. The fatigue behaviour of metallic glasses was

observed to be cycle dependent, not time dependent as for hard, non-metallic glasses. The S-N curve had distinct fatigue limit σ^* with $\sigma^*/\sigma_f \approx 0.3$ at a critical number of cycles $\sim 10^5$. The rate of fatigue crack propagation (dl/dN) in glassy alloys was described by a power law of the stress intensity factor with exponent m ranging from 2-4 (247, 249, 250). A well-defined plastic zone consisting of slip bands around a fatigue crack propagated along slip bands formed ahead of the crack. Such a crack growth mechanism in a glass is very similar to that in crystalline metals. The fatigue slip bands which had a single slip step, however, were distinct from the so-called extrusions or intrusions as generally observed in crystalline metals. The mode III fracture toughness K_{III} values for Fe, Pd-Si and Zr-Cu glasses were 320, 140 and 190 $\text{Kgmm}^{-3/2}$ respectively (251). The tearing energy Γ was found to be proportional to the yield stress σ_y : $\Gamma/\sigma_y \approx 0.03 \text{ mm}$. The tearing energy of metallic glasses $\Gamma \approx 10 \text{ J/cm}^2$ is many orders of magnitude larger than in crystalline metals ($\sim 0.01 \text{ J/cm}^2$) (245).

2.6.6 Creep

Creep measurements in a metallic glass were first reported by Chen and Turnbull for Au-Ge-Si (252). The experiments demonstrated for the first time the existence of a rheological solid glass/metastable liquid transition. Creep measurements were conducted within a temperature range just below the glass transition temperature. Within this temperature range, the amorphous alloy behaves as a viscous liquid with a stress independent viscosity η ranging from 10^9 to 10^{12} P. The temperature dependence of viscosity follows a Fulcher-Vogel relation: $\eta = \eta_0 \exp[A/(T-T_0)]$. The η -T relation was found to be independent of how the

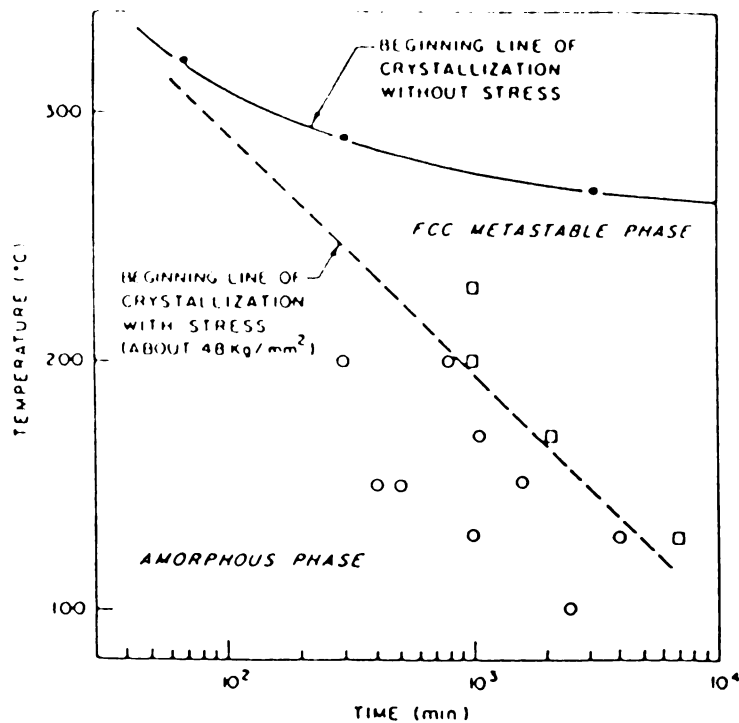


Figure 14: Effect of stress on the start of crystallization in an amorphous Pd-Si alloy (25).

temperature was reached. If the temperature is suddenly changed, the viscosity is found to lag behind the temperature change. Chen and Goldstein (21) have reported similar results on Pd-Au-Si, Pd-Ag-Si, and Pd-Cu-Si metallic glasses near their glass transition temperatures. At low stress and below the temperature T_a , at which $\eta = 10^{12}$ P, the behaviours of the alloys were similar to that of Au-Ge-Si. However, above T_a creep became non-Newtonian, and the viscosity was, therefore, stress dependent. Annealing the samples at $T > T_a$ had no effects on the creep behaviour near T_a , and hence phase separation was disregarded as the possible cause of the anomalous behaviour.

Maddin and Masumoto (25) carried out extensive creep measurements on Pd₈₀Si₂₀ in the temperature range 373 to 473 K ($T_g = 655$ K). It was observed that an applied tensile stress promotes crystallization (Figure

14) (25). Creep experiments were conducted at temperatures and during times within the region where the solid remained amorphous. From the analysis of the steady-state creep it was concluded that creep was non-Newtonian.

2.6.7 Effect of Deformation

Glassy alloys exhibit localized plastic deformation in tension, compression or in bending, suggesting that the strong metallic bonding remains though there is no long range order.

Effects of deformation in cold rolled glassy alloys e.g. Pd-Si (253) and Fe-P-C (254) have been reported. It was observed that in x-ray diffraction pattern, the first peak position shifts slightly to the low angle side and the width of the peak at half height becomes larger by cold rolling (Figure 15) (253). Mossbauer spectroscopy results showed that cold rolling decreased the component of the magnetization axis lying in the plane of the specimen (254). On cold rolling, the Young's modulus, the fracture stress and the hardness decreased as the reduction in the thickness of the glassy alloy increased (Figure 16) (253). The electrical resistance, however, increased on heating after cold rolling. It was concluded that deformation by rolling at room temperature produces much more disordered structure than is present in the as-quenched state by introducing additional irregularities through defects. Results of differential specific heat measurement experiments showed increase in the crystallization temperature indicating stabilization of the internal structure of the amorphous phase.

Chen (255) has reported effects of cold rolling on Young's modulus

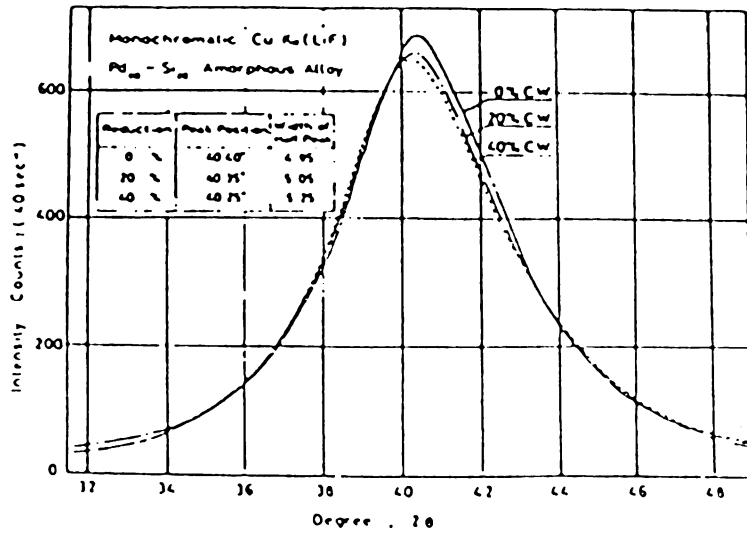


Figure 15: Effect of cold rolling on diffraction patterns of an amorphous Pd-Si alloy (253).

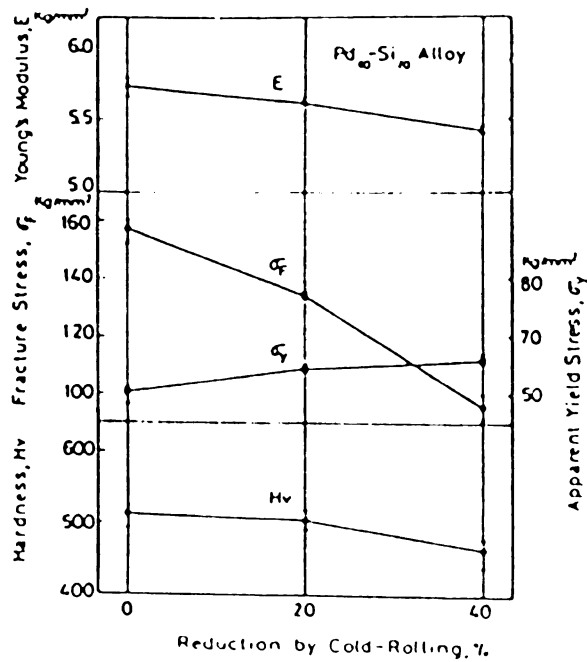


Figure 16: Effect of cold rolling on hardness and tensile properties of the Pd-Si alloy (253).

and structure of metallic glasses. The study concluded that cold rolling of metallic glasses induced two distinct atomic arrangements. Local atomic regrouping appeared to strengthen the structure and increase Young's modulus, whereas the unstable plastic flow lead to structural disorder and softening of glasses. Fe-based glass showed least ductility and smallest poisson's ratio among glasses studied, due to the highest degree of disorder created.

2.6.8 Annealing Embrittlement without Crystallization

Many Fe-based glasses which are ductile in the as-quenched state become brittle upon annealing apparently as a result of structural relaxation (41,45,214,229,250,256). In binary alloys such as Fe-B (45), Fe-P (45), and Zr-Cu (257,258), the alloys embrittle as a result of crystallization, whereas glass forming Pd, Ni, and Pt alloys exhibit a high ductility even in a partially crystalline state (259). The presence of crystalline dispersion in Ni-B alloys was shown to have less embrittling effect than it did in Zr-Cu (257). However, kinetics of embrittlement in many glassy alloys often correlate neither to the state of stress relief nor to the crystallization process (45,229,260,261). Chi et al. (262) showed that $\text{Fe}_{40}\text{Ni}_{40}\text{B}_{20}$ ribbons produced at slower quenching rate were stress relieved at slower rates but embrittled at much lower temperature with low apparent activation energy ~ 1 eV. Based on the observation that $\text{Fe}_{80}\text{P}_{13}\text{C}_7$ (244) and $\text{Fe}_{40}\text{Ni}_{40}\text{P}_{14}\text{B}_6$ (214) lose ductility at lower temperatures of annealing than do $\text{Fe}_{78}\text{B}_{12}\text{Si}_{10}$, $\text{Fe}_{80}\text{B}_{20}$, $\text{Fe}_{40}\text{Ni}_{40}\text{B}_{20}$ which contain no phosphorus, it was proposed that phosphorus is the embrittling agent in the two alloys containing it. Walter et al. (263) found P enrichment on the fracture surface of

$\text{Fe}_{40}\text{Ni}_{40}\text{P}_{14}\text{B}_6$ ribbons. Besides phosphorus segregation or clustering (256,263), phase separation of transition metals (45) and an increase in viscosity causing easier crack propagation (50) were proposed as the possible reasons for observed embrittlement. Chen (45) showed that the enhanced loss of ductility of various glasses studied occurred in the alloys containing two or more metalloid elements. Some P-containing glasses $\text{Fe}_{80}\text{P}_{17}(\text{B},\text{Si},\text{C})_3$ were found to exhibit a mechanical stability comparable to or surpassing those of B-containing glasses, $\text{Fe}_{80}\text{B}_{20}$ and $\text{Fe}_{40}\text{Ni}_{40}\text{B}_{20}$. Thus, he concluded that in the Fe-based alloys, presence of phosphorus cannot be the only cause for such annealing embrittlement as suggested by Luborsky et al. (214).

Chen (45, 229) proposed that local structural and compositional fluctuations analogous to phase separation in regions of ~ 20 Å accompanied by structural relaxation may be responsible for the enhanced embrittlement in glassy alloys. The resulting stress concentration around the clusters leads to embrittlement. This suggestion was strengthened by the fact that ternary alloys of Fe-P-B, Fe-P-Si and Fe-Co-P exhibited a higher tendency to phase separation and hence were more susceptible to embrittlement than were the corresponding binary alloys of Fe-P, Fe-B, and Co-P.

2.6.9 Stress-Strain Behaviour

Tensile tests have been performed on several metallic glasses (1, 218,239,264,265). Generally, the specimens were in the form of thin strips 20-40 μm thick and 1 mm wide. Typically (1,218,239,265) such ribbon specimens fail by shearing off (antiplane shear, slant fracture)

on a plane 45° to both the tensile axis and the thickness vector. Occasionally, at low temperatures, portions of square fracture are observed (264,266), i.e. fracture surface is perpendicular to the tensile axis -macroscopically (i.e. glass follows Tresca criteria (267)). Tensile failure of glassy alloy wires and strips (plane stress) is accompanied by intense plastic shear deformation. This is true whether the macroscopic mode of failure is brittle (tearing; antiplane shear, mode III failure) or ductile (yielding). Figure 17a shows a typical room temperature tensile load versus elongation curve for Pd-Si (1). Unloading experiments as in Figure 17b show that irrecoverable plastic strains occur before failure, and except for a small anelastic component (268), the glass behaves in an elastoplastic fashion. At room temperature tensile plastic elongations (measured after subtracting the linear elastic part) have been reported to be between 0.1 and 0.5% (1, 218,239) showing a macroscopically brittle behaviour. Masumoto and Maddin (1) have reported macroscopically ductile tensile behaviour in Pd-Si when pulled at temperatures above 473 K as shown in Figure 18. Below this temperature, the tensile elongation is 0.1% and increases rapidly above that temperature reaching 4% at 573 K.

As metallic glasses do not work harden their tensile strengths must be equal to or less than their yield strengths. The former case is observed when yielding and failure occurs simultaneously. According to plasticity theory, a thin sheet will yield (following von Mises' criteria) in a zone whose normal makes an angle $\theta = 35.3^\circ$ with the tensile axis and 90° with the thickness vector. According to Argon (269), θ will increase slightly if, as for metallic glasses, σ_y/E (σ_y = yield stress, E = Young's modulus) is large; for $\sigma_y/E \approx 0.02$, typical of

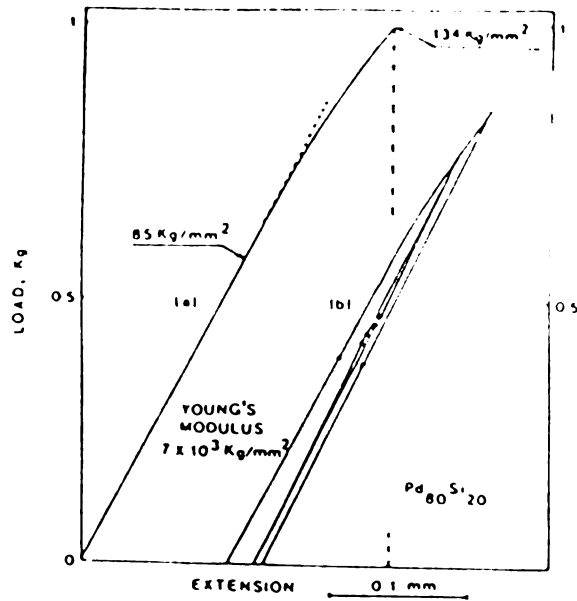


Figure 17: Representative stress-strain curves of a Pd-Si alloy (1).

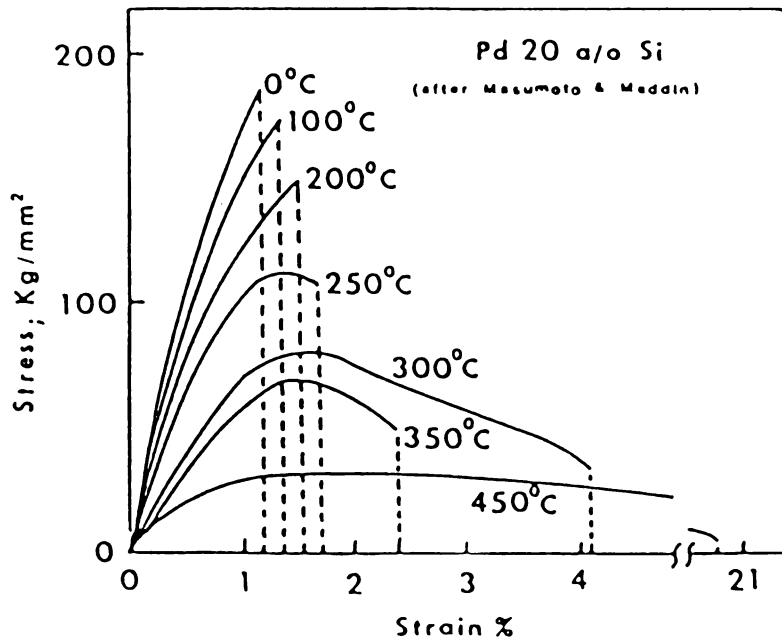


Figure 18: Stress-strain curves of a Pd-Si alloy as a function of temperature (1).

glassy alloys, predicted angle is 37° . Accordingly, the included angle (90°) measured on a wide face at the fracture tip of the specimen which fails coincident with yielding should be $\sim 53^\circ$. This failure geometry has been reported for Ni-Fe-P-B-Si ribbons (270). In Ni-Pd-P alloys it is reported that the fracture surface of the ribbon specimens made an angle of $55 \pm 5^\circ$ and 90° with the tensile axis on the narrow and wide surfaces respectively (271).

Davis (270) has suggested that in order to observe the 53° mode of failure at $T \ll T_g$, one must test specimens with a reduced area gage section with width to thickness (w/t) ratio of the order of 8:1. If smooth, uniform cross section ribbons are tested, failure is typically initiated at grips and occurs by tearing (mode III, antiplane strain (249)). If a reduced section specimen with $w/t \gg 8$ is pulled, failure will occur by tearing across the gage section but at somewhat higher stress due to elimination of the grip constraint. Uniform cross section ribbons fail (at the grips) in 45° slant mode.

Tomizawa and Masumoto (272) tested Cu-Zr alloy ribbons (0.5 mm wide and $20 \mu\text{m}$ thick) in tension. The fracture stress was observed to decrease with increasing strain rate. The fracture surface was at $45\text{--}50^\circ$ to the tensile axis and contained about 30% of smooth, featureless region and 70% of a region of the characteristic 'vein' pattern. Upon increasing strain rate in the tension test, the smooth region increased and the vein pattern became more pronounced.

Uniaxial compression deformation in Pd-Cu-Si (220,273), Pd-Ni-P and Pt-Ni-P (219) glassy alloys is reported in the literature. Figure 19 shows the uniaxial compressive nominal stress-strain curves for Pd-Cu-Si (220) at different temperatures, which approximate the expected

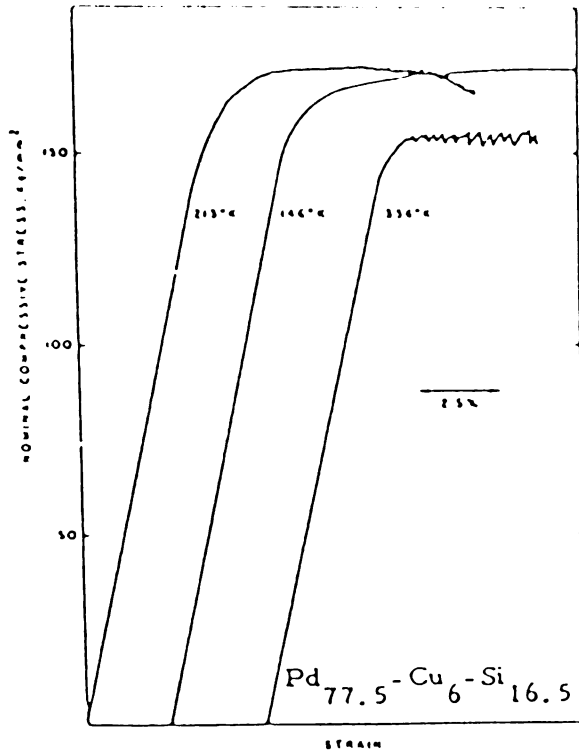


Figure 19: Compression stress-strain curves for a Pd-Cu-Si alloy (220).

behaviour for an elastic-perfectly plastic material. Davis (246) has attributed the roundness of these curves at low strain to extrinsic features such as slight misalignment of the specimen ends. In compression depending on temperature, the glass deforms initially in a smooth or stable way and after a certain strain continues by unstable or jerky flow and serrations (219,220). Serrated flow has been observed in Pd-Cu-Si (220), Pd-Ni-P and Pt-Ni-P (219) glassy alloys. Serrated flow in Pd-Cu-Si is suppressed below 200 K (220). Below this temperature deformation proceeds in a stable manner. Pampillo and Chen (220) have suggested that the unstable flow found in these experiments could be due to partial relaxation of the atomic rearrangements produced by plastic deformation. If these arrangements lead to a 'softer glass' (e.g.

destruction of compositional short range order or increase in the mean atomic volume), then above a certain temperature, T_0 , where there is enough atomic mobility, partial relaxation of these rearrangements (e.g. regeneration of the destroyed short range order) may occur as quickly as the rearrangements are produced: this leads to unstable flow. Below T_0 ($T_0 \approx 200$ K), the atomic mobility is too small to allow this and plastic deformation becomes stable. The explanation suggested is similar to the model postulated to explain serrated flow in crystalline substitutional solid solutions by Cottrell (274). So far, the analogy holds qualitatively, but more experimental data are required before reaching a conclusion.

2.6.10 Deformation Characteristics

Plastic deformation of metallic glasses occurs by either of two mechanisms: a diffuse rearrangement of atoms or the nucleation and propagation of narrow sheared regions. The first type of deformation mode is homogeneous and occurs when metallic glasses are deformed above their glass transition temperatures T_g , in absence of crystallization and at slow strain rates. Flow takes place uniformly with each volume element contributing an equal amount of strain. At low stresses, the strain-rate increases linearly with stress; at slightly higher stresses the strain-rate follows the sinh (stress) law (275). Fracture occurs when some section has necked down to a narrow thickness. Such a homogeneous (Newtonian) viscous flow in Au-Ge-Si metallic glass was first demonstrated by Chen and Turnbull (22).

The second type of deformation mode which is extremely inhomogenous occurs in the form of highly localized shear deformation

bands at temperatures well below T_g and at high strain rates. Plastic flow in a metallic glass at temperatures $T \ll T_g$ was first reported by Chen and Wang (268). Leamy et al. (218) showed that Pd-Si glassy alloy deformed in tension undergoes localized shear along the direction of maximum shear stress on a plane at 45° to both the tensile axis and the thickness vector, followed by shear rupture through the intense shear zone. The fracture surface exhibited two morphologically distinct zones. One zone was smooth and relatively featureless and the other consisted of 'vein' pattern of local necking protrusions. The local plastic shear produced a smooth zone, while the local necking protrusions were formed during rupture. Using stereomicroscopy Leamy et al. (218) demonstrated that veins were hills and not steps on a smooth background. The two complementary fracture surfaces were not mirror images microscopically, thus indicating that the glass did not fracture in a typical glassy or brittle manner. Similar results were obtained by Pampillo and Reimschuessel (276). Davis and Kavesh (264) have reported an enhancement in shear displacement prior to failure under superposed hydrostatic pressure resulting from suppression of crack nucleation. Shear offsets were observed on specimens deformed on rolling (220,277), compression (219,220) or bending (218,277,278). The shear bands lie in zones at $\pm 45^\circ$ to the rolling compression direction.

Under mechanical restraints such as in uniaxial compression, bending, rolling, drawing and indentation, multiple shear bands are observed. When a multiplicity of shear bands is activated macroscopic ductility is observed. On loading in compression, height reductions of about 40% are reported (220). While rolling of Ni-Pd-P ribbons, Takayama and Maddin (277) have reported 40% reduction in thickness. A

thin glassy alloy strip may be sharply bent back on itself without failure. As the temperature increases toward the glass transition the mode of deformation changes from inhomogeneous localized shear to homogeneous flow (or viscous creep) around a critical temperature depending on the strain rate. The tensile strength increases as the strain rate increases or temperature decreases in the homogeneous region; however, its dependence is small or opposite in the inhomogeneous region (1).

2.6.11 Deformation Mechanism

The highly localized deformation and temperature-insensitive fracture strength at lower temperature imply that the inhomogeneous flow is athermal with no work hardening (279). Indeed, Argon (280) suggested that strain localization requires work softening. Direct evidence for zero or negative rate of work hardening in a metallic glass was demonstrated by compression experiments of Pampillo and Chen (220). A specimen of Pd-Cu-Si alloy was compressed to initiate deformation bands and then repolished to remove the associated surface bands. Hence deformation was favored in existing shear bands either due to work softening or on availability of deformation sources, in which case the rate of work hardening could be zero. Pampillo (221) showed that shear bands produced by bending reverse when the direction of bending was reversed. This behaviour was found to be consistent with the absence of work hardening within the bands (281).

Polk and Turnbull (282) suggested the possibility that, at temperatures below T_g , plastic flow could destroy the compositional and/or

structural short range order in the glass, which in turn, lowers the resistance of the material against further deformation leading to concentration of plastic flow. As a part of the disorder created by plastic flow, the destruction of compositional order means that an increase in the number of metal-metal bonds across the slipped surface is created, at the expense of (very probably stronger) metal-metalloid bonds. This should lead to a decrease in the flow within the shear bands giving rise to an easy path for further deformation. The structural disorder created within slip bands could be in the form of an increase in the average atomic volume (282) or dilation (283) associated with plastic flow. The combination of a destruction of compositional order and dilation within the bands may lead to a critical or limiting structure within the band that allows deformation at a stress level lower than required to deform the bulk matrix.

Experimental support for this argument was provided by Pampillo (273) who showed that if a specimen is deformed, polished, and then etched, preferential attack occurs at the sites of the shear deformation bands. This demonstrated clearly a change in the local chemical potential of the deformed zone. This etching sensitivity disappeared if the glass was heat treated for 1 hr at about 50° C below the glass transition temperature because of structural relaxation.

Leamy et al. (218), on the other hand, suggested that concentration of plastic flow was due to the heating effect produced by plastic deformation i.e. by 'adiabatic shear'. The increase in temperature within the deforming band was considered to be high enough to produce softening of glass and promote further slip.

It should be pointed that some polymeric glasses, which are known

to have continuous random structure also deform by an extremely inhomogeneous shear (284). This shows that inhomogeneous shear slip can not be taken as an evidence of microcrystallinity, as recently suggested (285).

A different view point was presented by Pampillo and Reimschuessel (276). It was proposed that the concentrated shear deformation prior to failure defined a weaker 'pseudo-cleavage' plane on which nucleation and propagation of cracks would occur with greatest ease. The weakening of the sheared plane was thought to occur as a result of the structural changes occurring within the band.

Spaepen and Turnbull (286) suggested that when inhomogeneous flow occurs the weakening which initiates the shear band is due to the stress concentration near microcracks which are inevitably present. Further it was suggested that the shear viscosity should be lowered sharply in regions which are dilated by stress concentrations. In both models an important role is played by the rapid softening of the solid which occurs close to the glass-liquid transition. According to Spaepen and Turnbull (286), since plastic deformation occurs at constant volume, the density of the material that has deformed does not change. This means the viscosity remains relatively low also because no work hardening can occur. Thus the zone of plastic deformation consists of a layer of low viscosity between two solid phases.

Spaepen and Turnbull (286), and Pampillo and Reimschuessel (276) pointed out that the mechanism of instability leading to fracture in metallic glasses is the well known Taylor instability (287) which occurs at the moving boundary between two immiscible fluids. To demonstrate this, two glass slides which were held together by a thin layer of viscous medium were slowly separated. The resemblance of the

features thus formed with that of vein pattern has been considered as an evidence of the formation of a fluid layer.

The model of formation of viscous layers at deformation bands was criticized by Davis (288) because the vein pattern morphology of fracture surfaces of metallic glasses is also exhibited by some crystalline materials, e.g. by the shear rupture of 304 stainless steel (289).

Pampillo and Chen (220) observed that shear deformation bands terminate within compressed glassy alloy specimens. The elastic discontinuity which exists between the sheared and unsheared material is, by definition, a Volterra dislocation (281). The dislocation model was first introduced by Levengood et al. (290) to explain the wavy deformation band in natural silica glass and was later developed further by Gilman (283). Gilman proposed that strain is a result of the movement of the dislocation-like defects. Further he suggested that the creation of dilation (or excess free volume) during plastic shearing tends to reduce the viscosity in the immediate vicinity of the dislocation core and soften the local structure.

Unfortunately, dislocations in amorphous materials are not detectable by techniques such as transmission electron microscopy, i.e. diffraction contrast. However, results of positron annihilation data suggest no vacancy-type defects exist in the glassy alloys.

Spaepen (293) and Steif et al. (294) have proposed that deformation generates excess free volume, which in turn lowers the local glass transition temperature and hence decreases the viscosity. A model which combines free volume aspects at high temperatures (viscous-flow-like atomic arrangements) and dislocation aspects at low temperatures (the formation of disc-shaped shear zones) has been proposed by Argon (295).

Some of the models proposed are difficult to verify experimentally since they contain adjustable parameters which can not be measured independently. It seems that there is a need for further study in this regard to thoroughly understand the deformation in metallic glasses.

III EXPERIMENTAL PROCEDURE

Metallic glass used in this investigation had a nominal composition of $\text{Fe}_{80}\text{B}_{14.5}\text{Si}_{3.5}\text{C}_2$ (Metglas 2605SC, Allied Chemical Corporation). The metallic glass obtained was in the form of ribbons, produced by melt-quenching technique. The thickness of the foils was $25\ \mu\text{m}$ and the width was 5 cms. Some of the physical properties of the metallic glass are listed in Table IV. A ruby laser was used in the normal pulse operation (i.e. without Q-switching) to study the interaction mechanism. The laser pulse had a Gaussian profile with an average pulse duration of 12 msec

Table IV: Nominal composition and properties of Metglas 2605SC.

Nominal composition:	80% Fe, 14.5% B, 3.5% Si and 2% C (atomic %)
Density:	$7.38\ \text{gm/cm}^3$
Melting point:	1190°C on heating
Freezing point:	$1117\text{--}1095^\circ\text{C}$
Curie temperature:	420°C
Crystallization temperature:	500°C while scanning at a rate of $20^\circ\text{C}/\text{min}$ or 350°C for 2 hr anneal
Thermal conductivity:	$8\pm 1\ \text{Watts/Kelvin-meter}$ @ 23°C $10\pm 1\ \text{Watts/Kelvin-meter}$ @ 123°C
Electrical resistivity:	$1.25\ \text{micro-ohm-meter}$
Specific heat:	$0.120\ \text{cal/gm}^\circ\text{C}$ @ 25°C

at $\lambda = 0.6943\ \mu\text{m}$ and a maximum energy of 150 J. The laser focus was adjusted to a radius of $r_0(1/e) = 0.05\ \text{cm}$. By using the neutral density filters, the laser intensity in the spot center was varied in the range of $\sim 10^5$ to $\sim 10^7\ \text{Watts/cm}^2$. The experimental set-up is shown in Figure 20. Several hold-down conditions were used in this investigation. These included foils stretched as a membrane, foils supported on a metallic

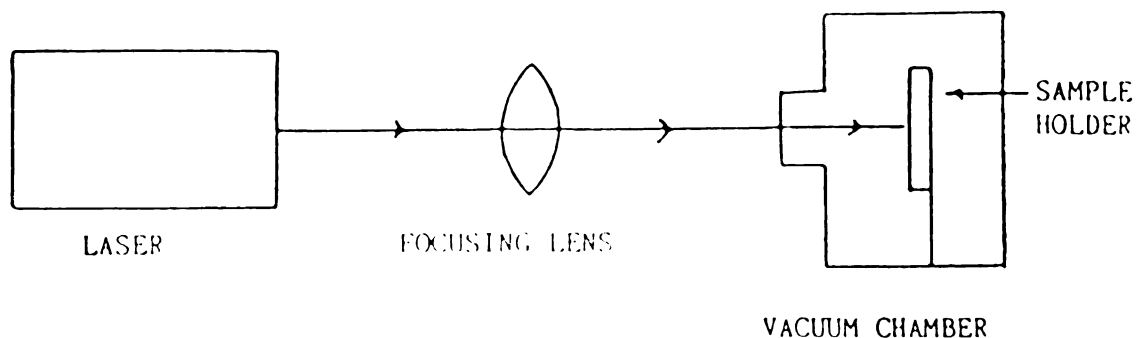


Figure 20: Schematic diagram of the experimental set-up.

(conducting) or a glass (nonconducting) substrate. Further, some sample edges were sandwiched between two metallic flanges with a circular opening of 2.5 cm. Neoprene gaskets were used to avoid metal-to-metal contact. This method provided a well defined and reproducible boundary condition. Some samples were irradiated through an optically flat quartz slide, sandwiching the sample against another nonconducting substrate. The smooth and shiny surface (i.e. the surface which is away from the wheel during melt-quenching) was always used as the surface of interaction. In order to investigate the spot-welding behaviour, some experiments were conducted in which two foils were held together by a circular hold-down ring.

Since amorphous to crystalline transformation is a function of the rate of heating, temperature as well as duration of heating, isothermal and isochronal annealing experiments were conducted on vacuum encapsulated specimens. X-ray diffraction technique was used following water quenching of the annealed samples. X-ray diffractometer (XRD) studies were conducted on as received, laser irradiated; and isothermally and

isochronally annealed specimens for comparison.

Ribbon specimens of Metglas 2605SC (width 5 mm, thickness 25 μm and length 20 mm) were tested in tension at room temperature as well as at various elevated temperatures; and at a strain rate of $4 \times 10^{-4} \text{ sec}^{-1}$, in an Instron testing machine. The edges were resin bonded to the specially designed grips. Prior to tensile testing, thus prepared specimens were annealed in the furnace at 150 °F for 8 hours, in order to dry the resin binder.

An optical microscope (OM) and a Scanning Electron Microscope (SEM) were used to study the microstructural aspects of the laser irradiated specimens as well as specimens fractured in tensile testing. An energy dispersive x-ray mapping technique was used to analyse the chemical segregation, if any, in the heat affected zone (HAZ) of the laser irradiated specimens.

IV RESULTS AND DISCUSSION

4.1 Laser Melting and Microstructural Characteristics of the Metallic Glass

When the metallic glass foil supported only along its edges was subjected to high-energy ($\sim 10^7$ Watts/cm²) ruby laser pulse, a roughly circular hole was produced in the foil (Figure 21). The average hole diameter was measured to be 2.5 mm for a laser spot size of ~ 0.05 cm. The laser irradiated zone represents a region of thermal gradients, with maximum temperature associated with the zone center. The temperature decreased radially away from the zone center. Thus, the resolidified region represents the zone where the temperature attained was equal to the melting point of the metallic glass. The boundary of the resolidified metallic glass formed a lip of uneven thickness due to the surface tension of the molten material. In Figure 21, surrounding the lip region is seen the HAZ, which shows a difference in electron absorption and emission properties under the SEM. In parts of HAZ, where the temperature exceeded the crystallization temperature, crystallization does take place; however, volume fraction of the crystallized mass is too small to be detected by XRD. Two radial cracks, radiating from the lip region, cutting across the HAZ and extending into unaffected region, are also seen. The nature of these cracks and shear band formation is discussed later. The nature of this damage site can be compared with corresponding damage in a ductile and crystalline material. For this purpose, an aluminum foil of comparable thickness was subjected to the same flux

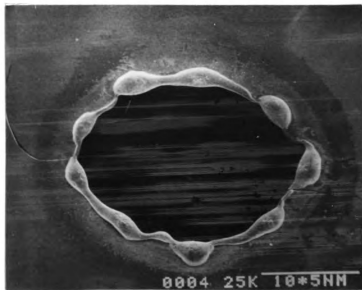


Figure 21: SEM picture of a hole drilled in Metglas 2605SC. Laser fluence $\sim 10^7$ W/cm².

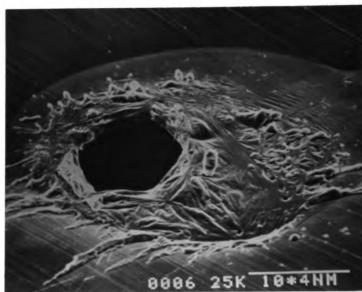


Figure 22: Laser damage in Al foil. Laser fluence $\sim 10^7$ W/cm².

density and the nature of the damage in this material is shown in Figure 22. Absence of any crack formation and profuse liquid metal ejection are noteworthy in this figure.

SEM observation of the lip region, which represents the boundary of the molten material, exhibits a columnar dendritic structure, and a large number of interdendritic voids as shown in Figure 23. Based on the dimensions of the average dendrite spacing, the cooling rate was estimated to be $\geq 10^5$ K/sec. Such a rapid cooling rate is comparable to the original rate of melt-quenching and thus no crystallization is expected to take place in this region. In the HAZ as shown in Figure 24 (a), the onset of crystallization, in the form of spherulites, was observed. The top portion of Figure 24(a) shows the boundary of the lip region. The omnipresence of the spherulites in the HAZ is evident. The laser flux density used was $\sim 10^7$ Watts/cm². The outlined region in Figure 24(a) is shown at a higher magnification in Figure 24(b), where the coalescing spherulites are seen to form a rosette-type structure. A considerable amount of volume change, associated with the growth of these spherulites is evident from the raised area (white region in Figure 24(b)). Analysis of such an area by using an energy dispersive x-ray mapping technique indicated a slightly higher silicon concentration along these impinging boundaries.

Reducing the power level to $\sim 5 \times 10^5$ Watts/cm², hole formation in the metallic glass ribbons could be avoided. At such a power level, however, within a distance of 100 μm from the center of laser irradiated zone, coalesced rosette structures were still present. Using an intermediate power density of $\sim 10^6$ Watts/cm², hole formation was still avoided; however, increased power density increased the region of localized

Figure 23: Dendritic resolidification structure at the lip of a laser induced hole. Laser fluence $\sim 10^7$ W/cm².

Figure 24: a) SEM micrograph showing distribution of spherulites in the HAZ, b) An enlarged view of the selected area in (a).

Figure 23:

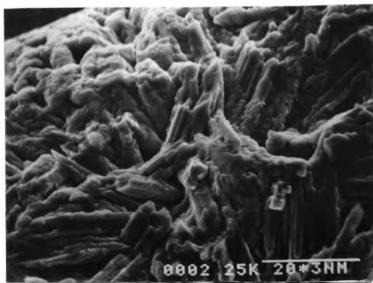


Figure 24(a)

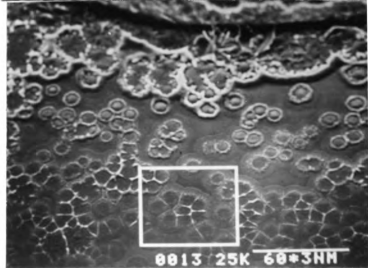
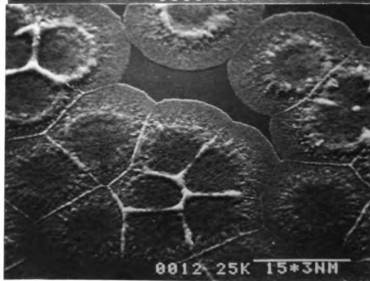


Figure 24(b)



melting in the central irradiated volume. The resulting resolidified structure was still dendritic (Figure 25). It was observed that as the input power level of the laser pulse was increased, the amount of interdendritic porosity also increased. Similar results have been reported by Inal et al. (71).

4.2 Spot-Welding Characteristics

Since at a power density of $\sim 10^5$ Watts/cm², even localized melting was avoided, this level of power input was considered optimum to attempt spot-welding of two foils. At such a power level, good contact between the foils was critical. Optimum pressure enabling good contact was required to assure spot-welding of the glassy foils. This was achieved by mounting two foils on the top of one another in a specially designed spring loaded holder. The spring pressure was determined by trial and error method. Attempts to spot-weld were successful when two pulses of $\sim 3 \times 10^5$ Watts/cm² were used. However, circumferential (Figure 26(a)) as well as transverse (Figure 26 (b)) cracks were observed near the welded region. At this power density, evidence of melting and/or resolidification was not observed. SEM micrographs of another such an attempt are shown in Figure 26(c). In this Figure, the central laser irradiated zone exhibits crystallites with faceted grain-like morphology. At a higher magnification (Figure 26(d)) the grain boundary voids are clearly visible. Figure 26(e) shows clear evidence of crystallization. In the HAZ a somewhat zig-zag path of intergranular cracks was observed as opposed to very smooth nature of cracks in the unaffected amorphous region. Devitrification of the surface region observed in Figure 26(d,e) is attributed to the overlapping of the laser pulses. Overlapping of the

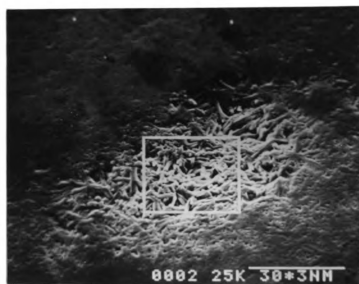
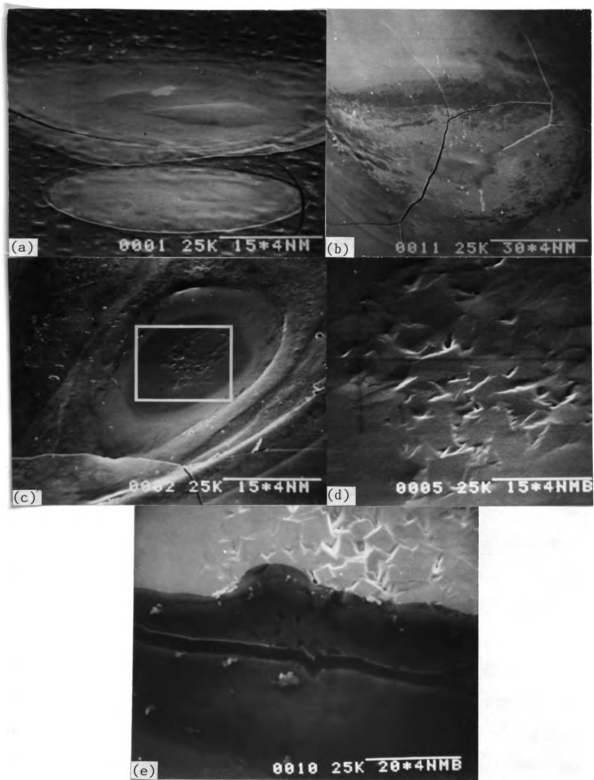


Figure 25: Dendritic resolidification structure at the center of the laser irradiated spot. Laser fluence $\sim 10^6 \text{ W/cm}^2$.

Figure 26: a) Circumferential cracks in spot-welded region; b) transverse cracks across spot-welded region; c) Laser spot-welded region showing surface rippling and crack formation; d) magnified view of region in (c) showing recrystallized polygonal domains; and e) intergranular crack along crystallized zone.



incident laser energy by multiple laser tracing in Pd-Cu-Si alloy has been shown to cause crystallization in the HAZ (129,296).

4.3 Crystallization Behaviour of Metglas 2605SC

In order to understand the crystallization products and the degree of crystallinity resulting due to pulse laser heating, equilibrium annealing of vacuum encapsulated metallic glass ribbons at various temperatures and for various time durations was conducted. Following the annealing treatment the samples were quenched in water and subsequently were examined by x-ray diffractometer using LiF single crystal monochromator and $\text{CuK}\alpha$ radiation. Figure 27 shows a composite diffraction pattern for the as-received material as well as for ribbons annealed at 400°C and 450°C for 15 minutes. A broad and smooth diffraction peak for the as-received ribbons is centered at $2\theta = 45.75^\circ$. X-ray diffraction studies performed on samples isothermally annealed at 350°C for 2 hours as well as for 4 hours, did not show any change in the appearance of the broad and smooth diffraction maximum. This result is thus at variance with the data supplied by the manufacturer (Table IV). However, heating the as-received specimen at 20 °C/min in DSC experiment indicated crystallization temperature, T_x , to be 500°C. This result agrees with the data supplied by Allied Corporation. There was no indication of crystallinity from the x-ray data, until the ribbons were annealed at temperatures $\geq 400^\circ\text{C}$. Similar results from the XRD studies on Metglas 2605SC are reported by Jones et al.(297). In their TEM studies, internal crystallization of α -Fe dendrites was detected only at temperatures $\geq 405^\circ\text{C}$. Prolonged annealing (upto 60 hrs) at 405°C in bulk ribbons caused extensive crystallization. Analysis of the DSC results indicated

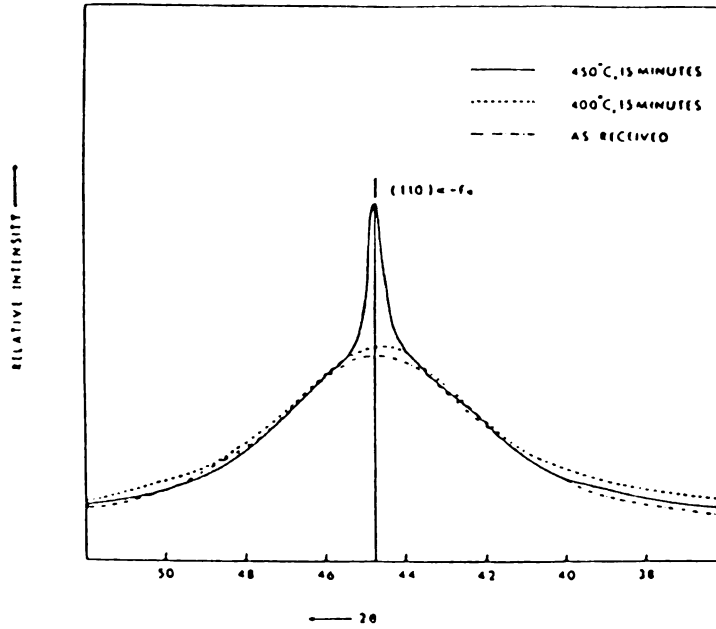


Figure 27: XRD results from as-received and isothermally annealed Metglas 2605SC.

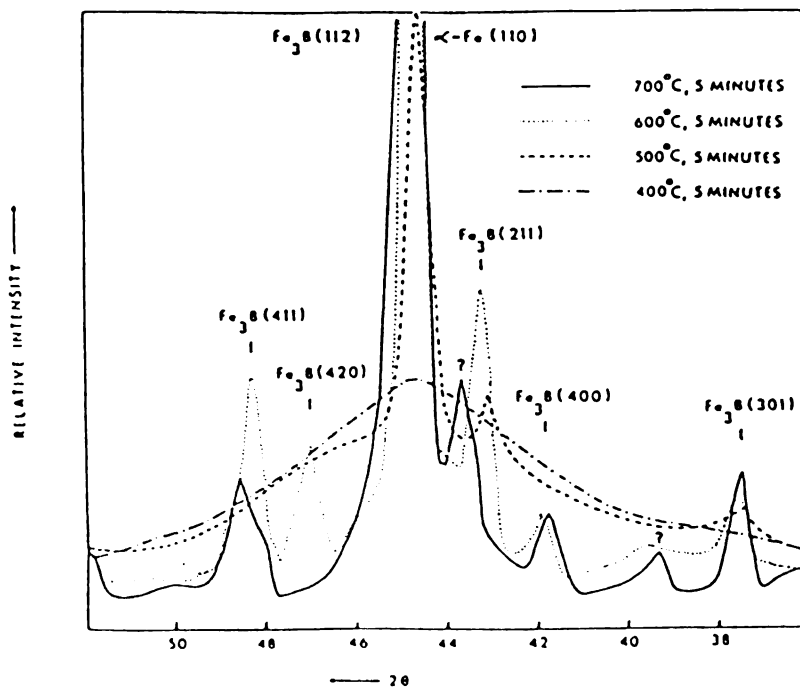


Figure 28: XRD results of various isothermal annealing treatments on the metallic glass showing α -Fe and Fe_3B peaks.

the first crystallization product to be α -Fe.

Results of our XRD experiments on annealed ribbons at 400°C for 15 minutes, showed only a minute change in the diffraction pattern, whereas annealing the samples at 450°C for the same time duration, indicated development of a narrower crystalline peak. On analysis, this peak was determined to be the (110) α -Fe. As the 2θ of the broad peak in the as-received material coincides with the (110) α -Fe peak of the vacuum annealed specimen, it would imply microcrystallinity on or near the surface of the metallic glass foil. The crystallite size from the broad diffraction maximum of the as-received material was calculated to be = 1.7 nm. It is entirely possible, these microcrystalline (quenched-in nuclei) are present at or near the surface. On subsequent heating, as in the case of pulse laser irradiation, these microcrystals can grow without the need for further nucleation. Such a growth of pre-existing surface nuclei could result in a morphologically and kinetically different crystallization behaviour than the bulk crystallization. Possibility of the presence of such quenched-in nuclei in the as-quenched ribbons was suggested by Leake and Greer (298) as well as by Schaafsma et al. (70). Quenched-in crystals were observed in amorphous Ni-B alloy by Walter et al. (299), who attributed their presence to a local reduction in the quench-rate caused by packets of gas being trapped in the molten metal during melt-spinning. Ok and Morrish (75,300) have shown that surface crystallization precedes bulk crystallization.

It was pointed out by Koster and Herold (81) that in isothermal annealing experiments on $\text{Fe}_{80}\text{B}_{20}$ (Metglas 2605) ribbons did not crystallize uniformly throughout their thickness. Crystallization was observed to start near the shiny side (free cooling side which is away

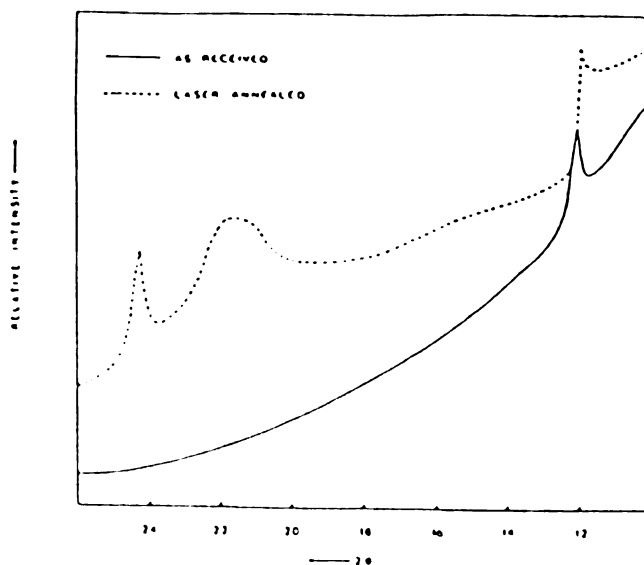


Figure 29: A comparison of x-ray diffraction intensity profiles from an as-received sample and a laser annealed foil.

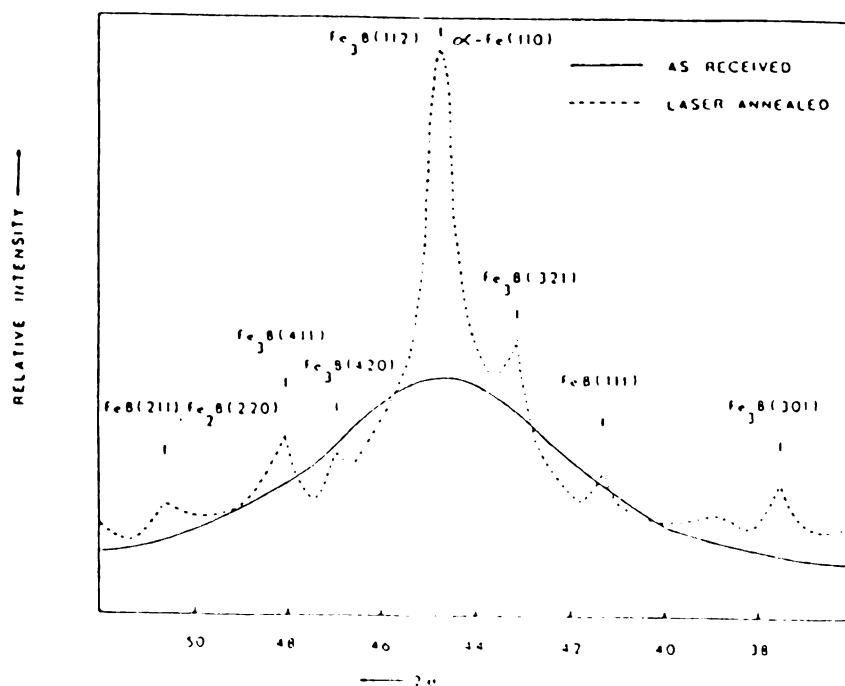


Figure 30: A comparison of x-ray diffraction intensity profiles from an as-received sample and a laser annealed foil.

from the wheel during melt-quenching) of the ribbon. Similar results were reported for $\text{Fe}_{80}\text{B}_{20}$ ribbons produced by melt-quenching method using one wheel (13,70,301) as well as $\text{Co}_{70}\text{B}_{30}$ (80) and $\text{Fe}_{80}\text{B}_{12}\text{Si}_8$ (73) glassy ribbons. Schaafsma et al. (70) also studied the crystallization behaviour of RQ $\text{Fe}_{80}\text{B}_{20}$ glassy ribbon, prepared by twin-roller quench technique. It was observed that there was no difference in the degree of crystallinity exhibited by opposite surfaces. It was suggested that glassy ribbons produced by using one-roller technique, the free cooling side cools slowly enough to have quenched-in nuclei at the surface. Crystallization occurs only by the growth of (crystalline) nuclei which are already present in the as-quenched amorphous material. However, in other metallic glasses, e.g. $\text{Fe}_{81}\text{B}_{13.5}\text{Si}_{3.5}\text{C}_2$ (87), $\text{Fe}_{82}\text{B}_{12}\text{Si}_6$ (302), $\text{Fe}_{40}\text{Ni}_{40}\text{Mo}_4\text{B}_{18}$ (75), $\text{Fe}_{75.4}\text{B}_{14.2}\text{Si}_{10.4}$ (303), the wheel side surface was observed to crystallize first. Our x-ray diffraction studies on isothermally as well as isochronally annealed ribbons did not show any difference in the degree of crystallinity from opposite surfaces.

XRD studies of the isothermally annealed ribbons of the metallic glass at high temperatures and at a shorter time duration (5 minutes) produced the (110) α -Fe peak which had grown in intensity (Figure 28). Additional diffraction peaks were indexed as the reflections from a metastable (70,71,78,81,88,91) Fe_3B phase.

Repeated pulse annealing of the metallic glass ribbon was done over an area of 0.5 cm x 1.5 cm by using power density $\sim 3 \times 10^5$ Watts/cm². XRD results of such a laser annealed specimen are shown in Figures 29 and 30. XRD patterns from opposite surfaces indicated that the degree of crystallinity was the same. In Figure 29, a diffraction pattern from the as-received ribbon shows a small crystalline peak near $2\theta = 12^\circ$, whereas

the laser annealed samples shows two additional peaks. These two additional peaks could not be identified either in terms of α -Fe or the borides (Fe_3B , Fe_2B or FeB). Presence of a narrow peak at $2\theta = 12^\circ$, in the amorphous background of the as-received material, indicates some microcrystallinity and such occurrences are not unusual (304). Figure 30 shows a comparison between the diffraction patterns from a laser annealed and an as-received metallic glass ribbon at higher 2θ angles. Most of peaks in the diffraction pattern of the laser annealed ribbon were identified to be from Fe_3B reflections. The lattice parameter of body centered tetragonal Fe_3B phase was determined to be $a = 0.863$ nm and $c = 0.429$ nm. The remaining peaks are either from Fe_2B or FeB . Since the heating and cooling rates due to laser irradiation are very rapid, metastable Fe_3B phase formation can be justified. In the overlapped regions of the HAZ, in successive laser irradiation, crystallization does take place. In Metglas 2605SC since iron is the major constituent, it is natural that it will separate out first as crystallization takes place. In regions in which temperature does not exceed T_x , rearrangement of the atoms in the matrix takes place. Thus, presence of α -Fe, as the first crystallization product is justified from Figure 27. As the heating times involved in the annealing treatments are relatively short, most other peaks formed at higher temperatures are due to Fe_3B . In $\text{Fe}_{80}\text{B}_{20}$ glass at sufficiently higher temperatures ($\geq 900^\circ\text{C}$) the metastable Fe_3B phase decomposes into α -Fe and Fe_2B (71). Presence of Fe_2B observed in our studies can be justified by suggesting that similar reaction occurs in regions where the temperature exceeds 900°C and cooling rates following laser heating are not rapid enough to avoid crystallization. Additional support comes from Tian et al.(88), who suggested that in

Metglas 2605SC, Fe_3B decomposes into $\alpha\text{-Fe}$ and Fe_2B above 1000°C . However, Swartz et al. (82) have reported $\alpha\text{-Fe}$ and Fe_3B as the crystallization products of Metglas 2605SC. Finally, presence of other crystalline phases, namely a Fe-Si alloy and Fe_3C as mentioned by other authors (89-91), was not identified. This may be due to a different technique used or due to the size and volume fraction of these phases. The same technique (Mossbauer spectroscopy) was used by Saegusa and Morrish (89,90) and Bhanuprasad et al.(91), however, their results are not in agreement with each other, including the first crystallization product formed. Thus, disagreement does exist regarding the sequence of crystallization products.

4.4 Crack Formation in the Metallic Glass

It was mentioned earlier that plastic deformation of metallic glasses occurs by either of two mechanisms: a diffuse rearrangement of atoms or the nucleation and propagation of narrow shear bands. The first type of deformation mode is homogeneous and occurs when metallic glasses are deformed above their glass transition temperatures T_g , without causing crystallization and at low strain rates. Under such conditions the plastic flow occurs uniformly with each volume element contributing an equal amount of strain. Whereas inhomogeneous deformation, in the form of shear bands, takes place at low temperatures ($T < T_g$) and at higher strain rates. It was noted that as the temperature increases towards the T_g , the mode of deformation changes from inhomogeneous to homogeneous mode around a critical temperature depending upon the strain rate. In laser irradiated metallic glass the heating is almost adiabatic and highly localized. In regions exceeding

the melting temperature, the molten mass resolidifies in the form of dendrites. From the estimated cooling rates these dendrites are amorphous; however, in the HAZ, crystallization takes place in regions where temperature exceeds T_x . At the boundary of the crystallized region and the amorphous matrix, lies the intermediate zone where small crystalline islands do exist. Because of such a host of microstructure, steep temperature gradient, and a strong thermoelastic stress wave which propagates through the solid, the deformation mode in the metallic glass when subjected to pulse laser heating can not be categorized fully as homogeneous or inhomogeneous. Instead, depending upon the temperature, microstructure, the input energy and hence the magnitude of the thermoelastic stress wave, in addition to homogeneous and inhomogeneous deformation mode, a mixed mode may also occur.

Figure 31(a,b) shows the nature of radial(R) and circumferential (C) cracks. It is to be noted here that the radial crack is a mode I type (crack opening). It can be postulated that the mode I cracks are formed by the contraction associated with the crystallization of the amorphous alloy. The free volume in the metallic glass is larger than the free volume in crystalline solid and thus upon crystallization void formation and/or contraction is expected (305). The tearing type of cracks (mode III) were observed to propagate well into the HAZ. In many cases, the initial mode I cracks were observed to make a transition to a mode III nature during its propagation towards the HAZ. The occurrence of tearing steps away from the laser spot (Figure 32) indicates that, though the tearing energy for most metallic glasses is higher by two orders of magnitude than crystalline metals (251), tearing does take place in the metallic glass due to laser irradiation, depending upon the

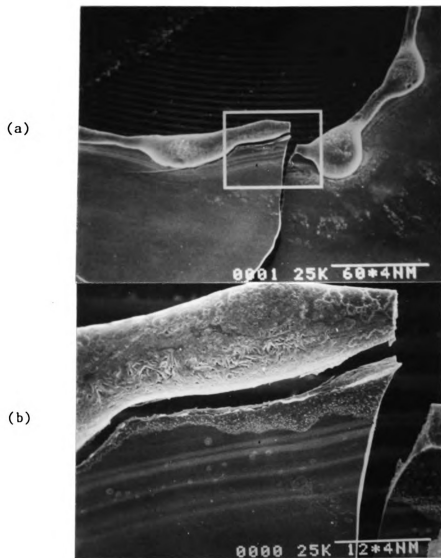


Figure 31: a) SEM picture showing crack formation; b) magnified view of selected region from (a) showing concentric bands.

Figure 32: SEM picture showing tearing steps.

Figure 33: a) SEM micrograph showing tearing steps and a crack-tip shear band zone induced by laser irradiation in Metglas 2605SC when covered with a transparent overlay; b) magnified view of the crack-tip shear band zone seen in (a).

Figure 32:

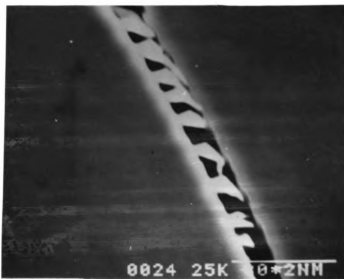


Figure 33(a):

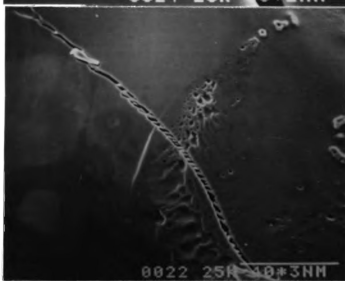
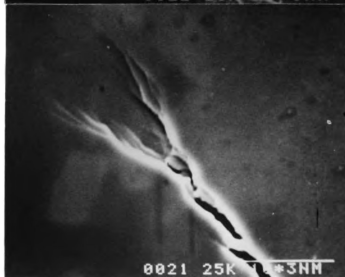


Figure 33(b):



input energy. Since tearing type of deformation is relatively difficult to occur in glassy alloys, it is suggested that the cracks are initiated by a crack opening mode but are propagated by a tearing mode, due to severe elastic displacement normal to the foil plane. Such an elastic displacement of a metallic surface, due to high energy laser pulse has been reported by other investigators (18,306).

In order to demonstrate the mode III nature of the cracks passing through the HAZ, it was essential to increase the amplitude of the peak shock pressure. Mukherjee et al. (18) have shown that magnitude of peak shock pressure is amplified if the surface of a metal is covered with a transparent overlay. Thus, a set of experiments were conducted in which the metallic glass ribbon was sandwiched between a quartz glass slide and a solid substrate, and subsequently was laser irradiated. Aside from pressure amplification, the overlay produced a constraint to displacement normal to the ribbon plane. As a result tearing steps were observed on the crack surface (Figure 32). At the crack-tip, however, a localized shear band zone was observed (Figure 33(a,b)). The crack-tip nonlinearity observed in the form of a shear band zone is discussed later.

4.5 Wavy Deformation and Shear Band Formation

The normal surface displacement, due to a propagating elastic wave, produces a concentric permanent plastic deformation in the foils. If the hold-down boundary condition is circular and symmetric to the laser spot, then a set of well defined wavy deformation bands are observed (Figure 34). If the stored elastic energy in the propagating elastic wave front is sufficient to produce plastic deformation, then shear bands can form in such a material since shear band formation is the

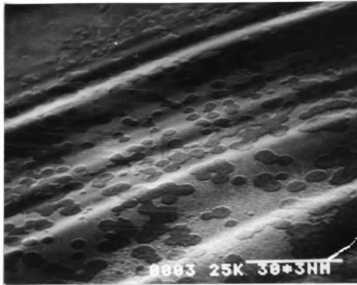


Figure 34: SEM micrograph showing wavy deformation bands.

primary mode of deformation in metallic glasses.

The spacing of the shear bands in a metallic glass is a function of temperature (307) and the spacing is coarser at elevated temperatures. Since the deformation in the laser irradiated metallic glass foil occurs in a region of steep temperature gradient, it is expected that coarser bands will form near the laser spot and a finer band spacing will be found in regions away from the high temperature zone. Indeed, this is found to be the case. Figure 35 shows the relatively coarse shear band spacing on the crack surface near the lip of hole drilled in the metallic glass. The average spacing in this region is $\approx 3 \mu\text{m}$ which can be compared with the shear band spacing of $\approx 0.5 \mu\text{m}$ on the crack surface away from the laser spot (Figure 36). Presence of the shear bands on the crack surface near the lip of the hole indicates clearly that the deformation at the boundary of the molten metallic glass was inhomogeneous.

The nature of shear bands in laser damaged metallic glass is quite different from that produced by mechanical tearing of the metallic

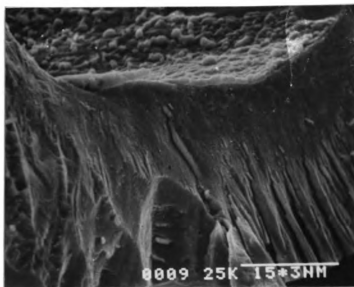


Figure 35: Coarse ($\sim 3 \mu\text{m}$) shear bands seen on the fracture surface near the hole.

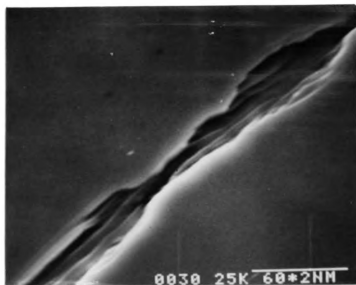


Figure 36: Finer ($\sim 0.05 \mu\text{m}$) shear band spacing observed on the crack surface away from the laser irradiated zone.

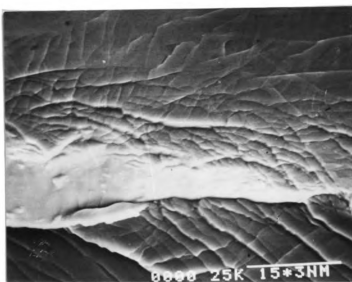


Figure 37: Shear bands in Metglas 2605SC produced by mechanical tearing at ambient temperature.

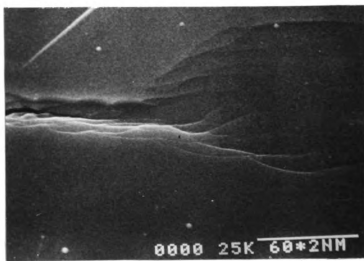


Figure 38: Crack-tip shear band zone induced by laser damage in the metallic glass. Angle of tilt 30°.

glass ribbon at the ambient temperature. Figure 37 shows the complex network of shear bands at the crack-tip produced in the metallic glass by mechanical tearing at room temperature. Such a generalized deformation mode was not observed in laser irradiated ribbons under any of the various sets of boundary conditions mentioned earlier. Figures 33(a,b) and 38 show the nature of crack-tip shear band configuration observed in laser irradiated ribbons.

Thus, it is evident that both temperature and strain rate play important roles in controlling the nature of the deformation in metallic glasses. In pulse laser heated metallic glass ribbon, the deformation proceeds through a steep temperature gradient, hence it is essential to know the response of the metallic glass to deformation at higher temperatures.

4.6 High Temperature Mechanical Testing

In order to understand the effect of temperature on the nature of deformation, the metallic glass ribbon specimens were tested in tension at various temperatures. Figure 39 shows a composite of the tensile stress versus strain curves as a function of temperature. At room temperature there was very little indication of macroscopic ductility; however, at higher testing temperatures the fracture stress decreased, and the plastic strain increased. The ribbon specimens did not have reduced gage sections. Thus the stress values obtained may be lower than if reduced section specimens were tested (246); however, the nature of the stress-strain response curves should not change. At temperatures lower than T_x , some specimens exhibited fragmentation upon failure. This behaviour may be explained in terms of annealing embrittlement occurring

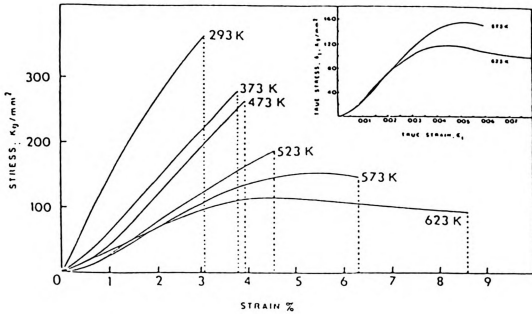


Figure 39: Stress-strain response curves of the metallic glass as a function of temperature.

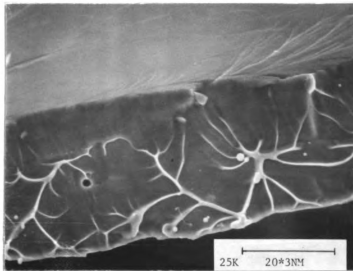


Figure 40: Tensile fracture surface showing characteristic vein pattern.

in Fe-based glassy alloys (308). It is to be noted here that all specimens did not show such a behaviour. At this point better justification can not be offered and further investigation is suggested. Similar occurrence of fragmentation upon failure in a Fe-based glassy alloy has been documented in literature (265).

The fractured surfaces of the specimens were examined using SEM. Figure 40 shows presence of characteristic 'vein' pattern. Void formation was also observed on the fractured surface occasionally. The specimen dimensions at the fracture surface were measured. From such measurements, there was no indication of necking (See Appendix 1). Above 523 K stress-strain curves exhibited strain softening. This behaviour is justified as metallic glasses do not work harden.

A set of experiments was also conducted in which the metallic glass ribbons were first annealed at various test temperatures (for the same time durations as in the high temperature deformation studies) and then were cooled to room temperature. Later, these specimens were tested in tension at room temperature. None of the specimens exhibited any macroscopic ductility. Also, annealing at higher temperatures reduced the fracture stress. Thus, from the results obtained, it is clear that the deformation temperature (above 523 K) was responsible for strain softening behaviour and not the structure present at that temperature. Since samples annealed at temperatures 573 K, but tested at room-temperature, did not exhibit any ductility.

Thus, from the tensile testing experiments at various temperatures, it is clear that deformation above certain critical temperature (in this case above 523 K), the metallic glass exhibits strain softening. In the following, a theoretical model is described to explain the observed

crack-tip shear band zone in terms of elastic-plastic response of the metallic glass.

4.7 Crack-Tip Nonlinearity

From fracture mechanics point of view, crack problems in a hypothetical homogeneous, incompressible, isotropic, elastic material, have been recently considered by some investigators (309-311). Metallic glasses satisfy these conditions more closely than a crystalline metal. These authors (309-311) have considered a special class of materials which lose equilibrium ellipticity at sufficiently severe deformations. For this class of materials, the elastic field near a crack-tip is quite different from that for materials which retain equilibrium ellipticity at all strains, e.g. most work hardening metals and alloys without a yield drop. The commonly considered point singularity at the crack-tip is replaced by a finite singular domain. Instability, leading to shear band formation within this domain is predicted from such a theory.

The starting point for such a solution requires the assumption of a specific nature of the Cauchy shear stress-strain response curve of the material. One fundamental prerequisite for the hyperbolic solution near the crack-tip is that at least one segment of the response curve exhibits strain softening. Non-trivial solutions can then be obtained by considering the strain energy density function or the elastic potential, W . These authors (309-311) have considered

$$W = W(I_1) \quad 4.1$$

where I_1 is the first fundamental scalar invariant of the Cauchy-Green deformation tensor. For an incompressible solid, the third scalar invariant, I_3 , is unity, and for the special class of materials, W is

considered to be independent of the second invariant, I_2 . For a mode III crack problem, the out of plane displacement U , in the anti-plane shear field satisfies the differential equation,

$$[W'(I_1) U_{,\alpha}],_{\alpha} = 0 \quad \text{on } D \quad 4.2$$

where D is the cross-section of open region R in the plane $x_3 = 0$. W' is the derivative of W with respect to I_1 . In anti-plane shear,

$$y_1 = x_1, \quad y_2 = x_2, \quad \text{and } y_3 = x_3 + U(x_1, x_2). \quad 4.3$$

Therefore the deformation gradient tensor, F , is given by

$$F = \begin{pmatrix} 1 & 0 & 0 \\ 0 & 1 & 0 \\ U_{,1} & U_{,2} & 1 \end{pmatrix} \quad 4.4$$

and left Cauchy-Green deformation tensor, G , is given by

$$G = F F^T = \begin{pmatrix} 1 & 0 & U_{,1} \\ 0 & 1 & U_{,2} \\ U_{,1} & U_{,2} & 1 + |\nabla U|^2 \end{pmatrix} \quad 4.5$$

Thus,

$$I_1 = 3 + |\nabla U|^2 \quad 4.6$$

where $|\nabla U|^2 = U_{,\alpha} U_{,\alpha}$. At infinite distance, for a simple shear in absence of a crack

$$U \sim kx_2 \quad 4.7$$

where $k \geq 0$ is the amount of applied shear, and x_2 , is along the coordinate normal to the direction of crack propagation and lies on the plane of the foil. Further, traction on the faces of the crack must vanish. Equations (4.2), (4.6) and (4.7), along with the vanishing traction at the crack surface define a boundary value problem. This boundary value problem has been solved for various assumed shear stress, (k) , and shear strain, k , response curves (309-311).

$$r(k) = \mu \left[1 + \frac{b}{n} k^2 \right]^{n-1} k \quad (0 \leq k < \infty)$$

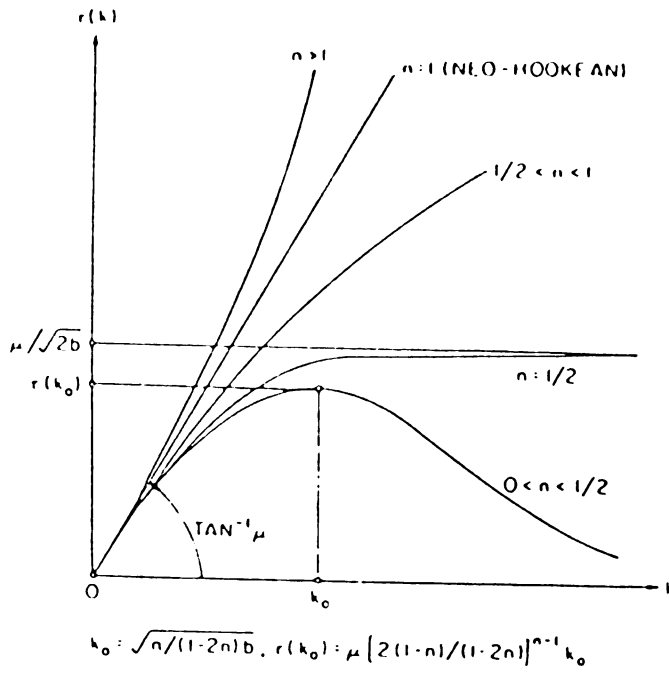


Figure 41: Response curve in simple shear for a power-law material (309).

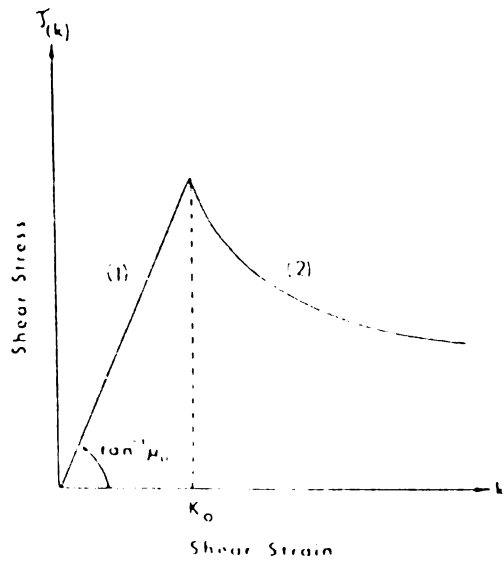


Figure 42: Cauchy shear stress-strain curve assumed by Knowles and Sternburg for a special class of materials (309).

In order to solve this boundary value problem, Knowles and Sternburg (309) initially considered a subclass of 'power law' materials which is governed by the elastic potential

$$W(I_1) = \frac{\mu}{2b} \left[\left[1 + \frac{b}{n} (I_1 - 3) \right]^n - 1 \right] \quad (3 \leq I_1 < \infty) \quad 4.8$$

where μ , b and n are material constants. The corresponding response curve in simple shear is expressed by

$$\tau(k) = \mu \left[1 + \frac{b}{n} k^2 \right]^{n-1} k \quad (0 \leq k < \infty) \quad 4.9$$

where μ is the shear modulus at infinitesimal deformations, and n is the hardening parameter. Figure 41 shows the response in shear for various values of n . A power-law material hardens or softens in simple shear depending on whether $n > 1$ or $n < 1$ respectively. For $n \geq 1/2$, $\tau(k)$ strictly increases monotonically with k such that $\tau(k) \rightarrow \infty$ as $k \rightarrow \infty$. For $n = 1/2$, $\tau(k)$ approaches $\mu/\sqrt{2b}$ as $k \rightarrow \infty$, whereas for $n < 1/2$, $\tau(k)$ has a maximum at $k = k_0 = [n/b(1-2n)]^{1/2}$ and then gradually decreases to zero. Thus, all solutions of the displacement equation of equilibrium (4.2) are elliptic everywhere when $n \geq 1/2$. For $n < 1/2$, a solution of (4.2) involving displacement gradients of magnitude exceeding k_0 at some point suffer loss of ellipticity. The response curve assumed by Knowles and Sternburg (309) for a special class of materials is shown in Figure 42. The segment (1) and (2) of this figure are assumed to be given by

$$(1) \quad \tau(k) = \mu k, \quad 0 \leq k \leq 1 \quad 4.10$$

$$(2) \quad \tau(k) = \mu k^{-1/2}, \quad 1 \leq k < \infty \quad 4.11$$

where μ is the slope of the linear segment. Note that $\tau(k)$ increases linearly with k upto $k=1$, whereas $\tau(k)$ decreases monotonically for $1 \leq k < \infty$ and $\tau(k) \rightarrow 0$ as $k \rightarrow \infty$. Equation (4.2) suffers a loss of ellipticity at a solution U and a point (x_1, x_2) if $|\nabla U(x_1, x_2)| > 1$.

The corresponding crack-tip nonlinearity is shown by the schematic

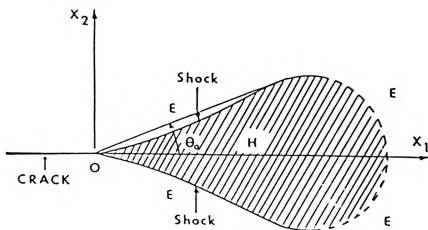


Figure 43: Crack-tip shear band zone predicted corresponding to the response curve shown in Figure 42 (309).

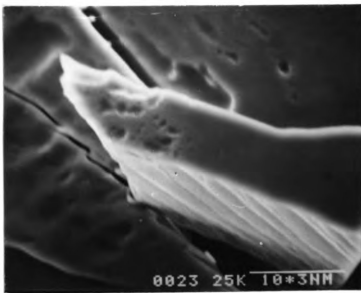


Figure 44: SEM picture showing evidence of normal surface displacement in the laser irradiated metallic glass specimen.

diagram in Figure 43. Across the elastostatic shocks, displacement and traction are continuous but displacement gradient and stress suffer a jump discontinuity. Within the cross-hatched region, strain localization and shear band formation are predicted.

The generalized form of the shear stress-strain response curve given by (4.10) and (4.11) is

$$\tau(k) = \mu k, \quad 0 \leq k \leq 1 \quad 4.12$$

$$\tau(k) = \mu k^{-\alpha}, \quad 1 \leq k < \infty \quad 4.13$$

where α is a material constant, restricted by $0 \leq \alpha < 1$. The angle θ_0 , defined in Figure 43, is related to the material constant, α , by (309)

$$\sin \theta_0 = \frac{1 - \alpha}{1 + \alpha} \quad 4.14$$

For the special class of materials considered by Knowles and Sternburg (309) $\alpha = 1/2$ and the angle θ_0 determined from equation (4.14) is 19.47° .

Table V: Comparison of measured and calculated θ_0 values.

θ_0 measured	α calculated from measured values	θ_0 obtained by Knowles and Sternburg (309)	α value considered by Knowles and Sternburg (309)
$18.5 \pm 0.5^\circ$	0.5183	19.47°	0.5
$19.0 \pm 0.5^\circ$	0.50878		
$19.5 \pm 0.5^\circ$	0.49394		
$20.5 \pm 0.5^\circ$	0.48125		

Returning to the experimental results, Figures 33(b) and 38 show crack-tip nonlinearity observed in the form of a shear band zone in the laser irradiated metallic glass. Note the observed shear band zone is remarkably similar in nature to the theoretically predicted configuration. θ_0 values measured from the experimental results are summarized

in Table V.

The average of measured values of Θ_0 when substituted in equation (4.14) yields $\alpha = 0.50056$, which is in close agreement with the value of $\alpha (=1/2)$ considered by Knowles and Sternburg (309). Thus the shear stress-strain response curve for the metallic glass studied can be represented by equations (4.10) and (4.11).

Mode III nature of deformation in the laser irradiated metallic glass was inferred from the tearing steps observed as shown in Figure 32. Additional evidence in support of this argument comes from the normal surface displacement observed in laser irradiated metallic glass as shown Figure 44. Shear band formation being the primary mode of deformation in metallic glasses, deformations can be considered locally volume preserving, thus satisfying the condition of incompressibility. Above 523 K, results of the tensile stress-strain curves exhibit clearly that strain softening does take place (as no necking was observed. See Appendix 1). Finally, though the crack propagation in the laser irradiated metallic glass foil, occurs through a steep temperature gradient, a crack-tip shear band zone, away from the HAZ is possible when the crack arrest occurs in the region where the temperature is suitable for such an instability. Thus, the model predicted by Knowles and Sternburg (309) is applicable in this study.

V CONCLUSIONS

In conclusion, it has been shown that a 12 msec duration laser pulse interacting with an Fe-based metallic glass causes crystallization in the HAZ, even at power levels which do not produce substantial melt or hole drilling.

It is also shown that the crystallization occurs through the growth of spherulitic domains which coalesce to produce a network-type microstructure. It is suggested that the morphology and kinematics of this surface crystallization may be influenced by preexisting nuclei.

Joining or welding of two foils of the metallic glass is possible with the use of lower power density and multiple pulsing. However, in the HAZ, microcrystallinity is developed, causing some embrittlement and crack formation.

Results of XRD experiments on isothermally annealed ribbons of metallic glass foils indicated that α -Fe was the first crystallization product followed by formation of Fe_3B phase, which is a metastable one.

X-ray diffraction studies on isothermally as well as isochronally annealed ribbons did not show any difference in the degree of crystallinity from opposite surfaces.

For the first time, a direct experimental mapping of a crack-tip shear band zone was recorded. A theoretical model, predicted by Knowles and Sternburg, was shown to be applicable in this study.

APPENDIX I

Original cross sectional area of the specimen, A_o , is

$$A_o = 5 \text{ mm} \times 0.025 \text{ mm} = 0.125 \text{ mm}^2 .$$

As the load bearing capacity of the specimen does not change

$$\frac{\sigma_f}{A_f} = \frac{\sigma_{\max}}{A_{\max}} \quad (\text{i})$$

Assuming locally volume preserving deformations, i.e. constancy of volume,

$$A_o l_o = A_{\max} l_{\max} \quad (\text{ii})$$

where A_{\max} and l_{\max} represent the cross sectional area and length of specimen at the maximum load respectively. Thus,

$$A_{\max} = \frac{A_o l_o}{l_{\max}} = \frac{0.125 \times 20}{20.045} = 0.1247 \text{ mm}^2. \quad (\text{iii})$$

Now, substituting value of A_{\max} in equation (i),

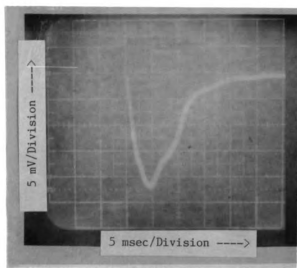
$$A_f = \frac{\sigma_f \times A_{\max}}{\sigma_{\max}} = \frac{91.94 \times 0.1247}{112.90} = 0.10156 \text{ mm}^2. \quad (\text{iv})$$

Thus, if necking took place, then the cross sectional area at fracture should have been 0.10156 mm^2 , which is about 18.75% smaller than the original cross sectional area. Such a reduction in area was not seen. This supports that strain softening occurred in the metallic glass at the temperature.

APPENDIX II

In order to obtain a pulse duration profile of the ruby laser used in this study following arrangements were made. A defocussed ruby laser beam was made incident on a silicon photodiode (Newport Research Corporation, Model # 882) after passing the laser beam through an optical diffuser and a neutral density 3.0 filter. This was done to avoid the detector saturation. The output of the pulse detector was fed to a storage oscilloscope (Tektronix, model # 464) through a laser power meter (Newport Research Corporation, model # 820). The pulse duration profile obtained is shown in the figure below.

Figure I: Voltage versus time duration profile of a ruby laser pulse.



LIST OF REFERENCES

LIST OF REFERENCES

1. T. Masumoto and R. Maddin, *Acta Met.*, 19 (1971) 725.
2. R. L. Freed and J. B. Vander Sande, *ibid* 28 (1980) 103.
3. C. P. Peter Chou and F. Spaepen, *ibid* 23 (1975) 609.
4. J. M. Vitek, J. B. Vander Sande, and N. J. Grant, *ibid* 23 (1975) 165.
5. L. E. Tanner and R. Ray, *Scripta Met.*, 11 (1977) 783.
6. M. A. Marcus, *Acta Met.*, 27 (1979) 879.
7. F. E. Luborsky and J. L. Walter, *J. Appl. Phys.*, 47(8) (1976) 3648
8. H. Chang and S. Sastri, *Metall. Trans.*, 8A (1977) 1063.
9. F. E. Luborsky, *Mater. Sci. Eng.*, 28 (1977) 139.
10. K. Shimomura, P. H. Shingu, and R. Ozaki, *J. Mater. Sci.*, 15 (1980) 1175.
11. T. Watanabe and M. Scott, *ibid* 15 (1980) 1131.
12. U. Herold and U. Koster, in 'Rapidly Quenched Metals III', (ed. B. Cantor), Vol.1, p. 281, Metals Society, London (1978).
13. A. L. Greer, *Acta Met.*, 30 (1982) 171.
14. D. G. Morris, *ibid* 29 (1981) 1213.
15. P. Duhaj, D. Barancok, and A. Ondryka, *J. Non-Cryst. Solids*, 21 (1976) 411.
16. B. C. Giessen, Ref. 12. p. 438.
17. J. F. Ready, in 'Effects of High-Power Laser Radiation', Academic Press, New York (1971).
18. K. Mukherjee, T. H. Kim and W. T. Walters, in 'Lasers in Metallurgy', (ed. K. Mukherjee and J. Mazumder), p. 137, The Metallurgical Society of AIME, Warrendale, Pa. (1981).

19. B. G. Bagley, H. S. Chen, and D. Turnbull, *Mater. Res. Bull.*, 3 (1968) 159.
20. A. Staudinger and S. Nakaharas, *Thin Solid Films*, 45 (1977) 125.
21. H. S. Chen and M. Goldstein, *J. Appl. Phys.*, 43 (1972) 1642.
22. H. S. Chen and D. Turnbull, *J. Chem. Phys.*, 48 (1968) 2560.
23. H. S. Chen, *J. Non-Cryst. Solids*, 29 (1978) 223.
24. C. A. Angell, *J. Am. Ceram Soc.*, 51 (1968) 117.
25. R. Maddin and T. Masumoto, *Mater. Sci. Eng.*, 9 (1972) 153.
26. H. S. Chen, *J. Non-Cryst. Solids*, 27 (1978) 257.
27. H. S. Chen, *J. Appl. Phys.*, 49 (1978) 3289.
28. H. S. Chen and D. Turnbull, *Appl. Phys. Letts.*, 10 (1967) 284.
29. H. S. Chen and K. A. Jackson, in 'Metallic Glasses', p. 75, Metals Park, Ohio:ASM (1978).
30. T. Egami and T. Ichikawa, *Mater. Sci. Eng.*, 32 (1978) 293.
31. N. A. Pratten and M. G. Scott, *Scripta Met.*, 12 (1978)137.
32. H. S. Chen, H. J. Leamy, and M. Bartmatz, *J. Non-Cryst. Solids*, 5 (1970) 444.
33. T. Soshiroda, M. Koiwa, and T. Masumoto, *J. Non-Cryst. Solids*, 22 (1976) 173.
34. F. E. Luborsky, J. J. Becker, and R. O. McCary, *IEEE Trans Magn.*, MAG-11, (1976) 1644.
35. T. Egami, *J. Am. Ceram Soc.*, 60 (1977) 128.
36. K. D. Krishnanand and R. W. Cahn, *Scripta Met.*, 9 (1975) 1259.
37. H. S. Chen and E. Coleman, *Appl. Phys. Lett.*, 28 (1976) 245.
38. F. E. Luborsky, R. O. McCary, and J. J. Becker, in 'Rapidly Quenched Metals', (eds. N. J. Grant and B. C. Giessen) Vol. 1, p. 467, MIT Press, Cambridge, MA (1976).
39. Y. Waseda and T. Masumoto, *Z. Phys.*, B 22 (1975) 121.
40. Y. Waseda, H. Okazaki, and T. Masumoto, *J. Mater. Sci.*, 12 (1977) 1927.
41. H. S. Chen, in 'The Structure of Non-Crystalline Solids', (ed. P. H. Gaskell) p. 79, Taylor and Francis, London (1977).

42. H. S. Chen, L. C. Kimberling, J. M. Poate, and W. L. Brown, *Appl. Phys. Lett.*, 32 (1978) 461.
43. B. S. Berry and W. C. Pritchett, *J. Appl. Phys.*, 44 (1973) 3122.
44. H. S. Chen, R. C. Sherwood, H. J. Leamy, and E. M. Gyorgy, *IEEE Trans. Magn.*, MAG-12, (1976) 933.
45. H. S. Chen, *Scripta Met.*, 11 (1977) 367.
46. F. E. Luborsky and J. L. Walter, *Mater. Sci. Eng.*, 35 (1978) 255.
47. H. S. Chen, *J. Appl. Phys.*, 49 (1978) 4595.
48. F. E. Luborsky, *AIP Conf. Proc.*, 29 (1976) 209.
49. B. S. Berry and W. C. Pritchett, *J. Appl. Phys.*, 47 (1976) 3295.
50. R. S. Williams and T. Egami, *IEEE Trans. Magn.*, MAG-12, (1976) 927.
51. J. W. Christian, in 'The Theory of Transformations in Metals and Alloys', p 525, Pergamon Press, Oxford (1965).
52. D. Turnbull, *Solid State Phys.*, 3 (1956) 225.
53. B. G. Bagley and E. M. Vogel, *J. Non-Cryst. Solids*, 28 (1975) 29.
54. C.-P. Chou and D. Turnbull, *ibid* 17 (1975) 168.
55. J. J. Burton and R. P. Ray, *ibid* 6 (1971) 393.
56. H. L. Yeh and R. Maddin, *Ref. 38*. p. 281.
57. M. G. Scott and P. Ramachandrarao, *Mater. Sci. Eng.*, 29 (1977) 137.
58. P. H. Shingu, K. Shimomura, R. Ozaki, K. Osamura, and Y. Mukarami, as in *Ref. 12*. p. 315.
59. N. Funakoshi, P. Kanamori, and T. Manabe, *Japan J. Appl. Phys.*, 16 (1977) 515.
60. P. G. Boswell, *Scripta Met.*, 11 (1977) 701.
61. E. Coleman, *Mater. Sci. Eng.*, 23 (1976) 161.
62. T. Masumoto, A. Inoue, and H. Kimura, *J. Japan Inst. Met.*, 41 (1977) 730.
63. K. L. Chopra, in 'Thin Film Phenomena', p. 195, McGraw Hill, New York, (1969).
64. J. Megusar, J. B. Vander Sande, *Ref. 38*. p. 401.

65. R. L. Freed and J. B. Vander Sande, *J. Non-Cryst. Solids*, 27 (1978) 9.
66. B. G. Bagley and D. Turnbull, *Acta Met.*, 18 (1970) 857.
67. J. L. Walter, P. Rao, E. F. Koch, and S. F. Bartram, *Metall. Trans.* 8A (1977) 1141.
68. J. L. Walter, S. F. Bartram, and R. R. Rusell, *ibid* 9A (1978) 803
69. L. E. Collins, N. J. Grant, and J. B. Vander Sande, *J. Mater. Sci.*, 18 (1983) 804.
70. A. S. Schaafsma, H. Snijder, and F. Vander Sande, *Phy. Rev.*, B 20 (11) (1979) 4423.
71. O. T. Inal, L. E. Murr, and F. G. Yost, *Mater. Sci. Eng.*, 51 (1981) 101.
72. H. N. Ok and A. H. Morrish, *Phy. Rev.*, B 22(7) (1980) 3471.
73. C. F. Chang and J. Marti, *J. Marer. Sci.*, 18 (1983) 2297.
74. H. N. Ok, K. S. Beak, and C. S. Kim, *Phy. Rev.*, B 24(11) (1981) 6600.
75. H. N. Ok and A. H. Morrish, *J. Appl. Phys.*, 52(3) (1981) 1835.
76. K. Osamura, K. Shibue, R. Suzuki, Y. Mukarami, and S. Takayama, *J. Mater. Sci.*, 16 (1981) 957.
77. F. L. Cumbreira, C. F. Conde, M. Millan, A. Conde, R. Marquez, *J. Mater. Sci. Lett.*, 2 (1983) 499.
78. T. Kemeny, I. Vincze, and B. Fogarassy, *Phy. Rev.*, B 20(2) (1979) 476.
79. O. T. Inal, L. Keller, and F. G. Yost, *J. Mater. Sci.*, 15 (1980) 1947.
80. U. Koster and U. Herold, *Scripta Met.*, 17 (1983) 495.
81. *Idem*, *ibid* 12 (1978) 75.
82. J. L. Walter, A. E. Berkowitz and E. F. Koch, *Mater Sci. Eng.*, 60 (1983) 31.
83. K. Muller and M. Von Heimendahl, *J. Mater. Sci.*, 17 (1982) 2525.
84. F. L. Cumbreira, H. Miranda, A. Conde, R. Marquez, and P. Vigier, *J. Mater. Sci.* 17 (1982) 2677.
85. D. G. Morris, *Scripta Met.*, 16 (1982) 585.

86. J. L. Walter, S. F. Bartram, and I. Mella, *Mater. Sci. Eng.*, 36 (1978) 193.
87. J. C. Swartz, R. Kossowsky, J. J. Haugh, and R. F. Krause, *J. Appl. Phys.*, 52(5) (1981) 3324.
88. D. C. Tian, F. Fouquet, F. Guyot, C. Mai, and J. Perez, *Mat. Sci. Eng.*, 53 (1982) 179.
89. N. Saegusa and A. H. Morrish, *Phy. Rev.*, B 26 (1982) 305.
90. Idem, *Phy. Rev.*, B 27 (1983) 4027.
91. B. Bhanu Prasad, A. K. Bhatnager, and R. Jagannathan, *J. Appl. Phys.*, 54(4) (1983) 2013.
92. H. S. Chen, *Appl. Phys. Lett.*, 29 (1976) 79.
93. H. Rawson, in 'Inorganic Glass-Forming Systems', Academy Press, New York, (1967)
94. R. W. Cahn, *Fizika 2 Suppl. 2*, papers 25 (1970)
95. D. Turnbull and M. H. Cohen, in 'Modern Aspects of the Vitreous State', (ed. J. D. Mackenzie) Vol. 1, p 36, Butterworth, London (1960).
96. D. Turnbull, *Contem. Phys.*, 10 (1969) 473.
97. D. R. Uhlmann, *J. Non-Cryst. Solids*, 7 (1971) 337.
98. H. A. Davies, *Phys. Chem. Glasses*, 17 (1976) 159.
99. P. I. K. Onorato and D. R. Uhlmann, *J. Non-Cryst. Solids*, 22 (1976) 367.
100. W. Klement, R. Willens, and P. Duwez, *Nature*, 187 (1960) 869.
101. J. Dixmier, K. Doi, and A. Guinier, in 'Phys. of Non-Cryst. Solids', *Proc. Int. Conf.* p. 67, Interscience, New York (1964).
102. G. S. Cargill, III, *J. Appl. Phys.*, 41 (1970) 12.
103. G. S. Cargill, III and R. W. Cochrane, *J. Phys.*, Paris 35 (1974) CA 269.
104. J. Logan, *Phys. Stat. Solidi*, A30 (1976) 73.
105. T. Ichikawa, *ibid* A19 (1973) 707.
106. S. Mader, A. S. Nowick, and H. Widmer, *Acta Met.*, 15 (1967) 203.
107. S. R. Herd and P. Chaudhari, *Phys. Stat. Solidi*, A 26 (1974) 627.

108. M. G. Scott, and R. Maddin, Ref. 38, p. 249.
109. G. Marchal, P. Mangin, and C. Janot, *Phil. Mag.*, 32 (1975) 1007.
110. P. Mangin, G. Marchal, B. Rodmacq, and C. Janot, *ibid* 36 (1977) 643.
111. S. Mader, in 'Recrystallization, Grain Growth and Texture', p. 523, Cleveland: ASM (1966).
112. R. Roy, *J. Non-Cryst. Solids*, 3 (1970) 33.
113. P. Pietrokowsky, *Rev. Sci. Instrum.*, 34 (1963) 455.
114. H. S. Chen and C. E. Miller, *ibid* 41 (1970) 1237.
115. E. Babic, E. Girt, R. Krsnik, and B. Leontic, *J. Phys., E. Sci. Instrum.* 3 (1970) 1014.
116. E. H. Strange and C. A. Pim, 1908 US Patent No. 905758.
117. R. Pond and R. Maddin, *Trans. Metall. Soc. AIME* 245 (1967) 407.
118. H. H. Liebermann and C. D. Graham, *IEEE Trans. Magn.*, MAG-13, (1976) 921.
119. H. S. Chen and C. E. Miller, *Mater. Res. Bull.*, 11 (1975) 49.
120. R. E. Maringer and C. E. Mobley, *J. Vac. Sci. Tech.*, 11 (1974) 1067.
121. P. H. Shingu, K. Shimomura, and R. Ozaki, *Trans. Jpn. Inst. Met.*, 20 (1979) 33.
122. C. F. Cline and R. W. Hopper, *Scripta Met.*, 11 (1977) 1137.
123. T. Yamaguchi and K. Narita, *Appl. Phys. Lett.*, 35 (1978) 468.
124. S. A. Miller and R. J. Murphy, *Scripta Met.*, 13 (1979) 673.
125. E. M. Breiman, B. H. Kear, and C. M. Banas, *Phys. Today*, Nov. p. 44 (1976).
126. J. M. Poate, H. J. Leamy, T. T. Sheng, and G. K. Keller, *Appl. Phys. Lett.*, 33 (1978) 918.
127. R. Fastow, J. Gyulai, M. Nastasi, and P. G. Zielnski, *J. Mater. Sci.*, 3 (1984) 109.
128. H. Yoshioka, K. Asami, and K. Hashimoto, *Scripta Met.*, 18 (1984) 1215.
129. K. Asami, T. Sato, and K. Hashimoto, *J. Non-Cryst. Solids*, 68 (1984) 261.

130. S. Yatsuya and T. B. Massalski, *Mat. Sci. Eng.*, 54 (1982) 101.
131. R. Becker, G. Sepold, and P. L. Ryder, *Scripta Met.*, 14 (1980) 1283.
132. C. -J. Lin, F. Spaepen, and D. Turnbull, *J. Non-Cryst. Solids*, 61-62 (1984) 767.
133. H. H. Liebermann, *IEEE Trans. Magn.*, MAG-15, (1979) 1393.
134. J. L. Walter, Ref. 12. p.30.
135. H. Jones, *Rep. Prog. Phys.*, 36 (1973) 1425.
136. R. C. Ruhl, *Mater. Sci. Eng.*, 1 (1967) 313.
137. C. H. Bennett, *J. Appl. Phys.*, 43 (1972) 2727.
138. A. Rahaman, M. J. Mandel, and J. P. McTague, *J. Chem. Phys.*, 64 (1976) 1564.
139. H. A. Davies, J. Aucote, and J. B. Hull, *Nature Phys. Sci.*, 246 (1973) 13.
140. M. Hansen, in 'Constitution of Binary Alloys', McGraw Hill, New York (1958).
141. R. Ray, B. C. Giessen, and N. J. Grant, *Scripta Met.*, 2 (1968) 357.
142. B. C. Giessen, J. Hong, L. Kabacoff, D. E. Polk, R. Raman, and S. Amand, Ref. 12. p. 249.
143. R. Ray and E. Musso, US Patent No. 3981722 (1976).
144. B. C. Giessen and R. O. Elliott, Ref. 12. p. 406.
145. H. A. Davies and J. B. Hull, *J. Mater. Sci.*, 9 (1974) 707.
146. P. Ramachandrarao, M. Laridjani, R. W. Cahn, *Z. Metall.*, 63 (1972) 43.
147. P. Furrer and H. Warlimont, *Mat. Sci. Eng.*, 28 (1977) 127.
148. K. Chattopadhyay, P. Ramachandrarao, S. Lele, and T. R. Anantharaman, Ref. 38. p. 157.
149. W. L. Johnson, S. J. Poon, and P. Duwez, *Phy. Rev. B* 11 (1975) 150.
150. K. H. J. Buschow, N. M. Beekmans, Ref. 12. p. 133.
151. K. H. J. Buschow, A. M. Van Diepen, N. M. Beekmans, and J. W. M. Biesterbos, *Solid State Commun.* 28 (1978) 181.

152. H. S. Chen, *Acta Met.*, 22 (1974) 1505.
153. M. Naka, Y. Nishi, and T. Masumoto, *Ref. 12.* p. 231.
154. W. Hume -Rothery and E. Anderson, *Phil. Mag.*, 5 (1960) 383.
155. C. H. Bennett, D. E. Polk, and D. Turnbull, *Acta Met.*, 19 (1971) 1295.
156. G. S. Cargill, III, *Solid State Phys.*, 30 (1975) 227.
157. P. K. Srivastava, B. C. Giessen, and N. J. Grant, *Met. Trans.*, 3 (1972) 977.
158. P. Predecki, B. C. Giessen, and N. J. Grant, *Trans. Metall., Soc. AIME* 233 (1965) 1438.
159. S. R. Nagel, and J. Tauc, *Phys. Rev. Lett.*, 35 (1975) 380.
160. G. A. Chadwick, in 'Liquids: Structure Properties Solid Interactions', p. 326, Elsevier, New York (1965).
161. T. Masumoto and R. Maddin, *Mater. Sci. Eng.*, 19 (1975) 1.
162. N. F. Mott, and R. W. Gurney, *Rep. Prog. Phys.*, 5 (1938) 46.
163. N. Valenkov and E. Porai -Koshits, *Z. Krist.*, 95 (1937) 195.
164. J. D. Bernal, *Nature*, 185 (1960) 68.
165. M. H. Cohan and D. Turnbull, *ibid* 203, (1964) 964.
166. J. F. Sadoc, J. Dixmier, and A. Guinier, *J. Non-Cryst. Solids*, 12 (1973) 46.
167. D. E. Polk, *Acta Met.*, 26 (1972) 485.
168. B. C. Giessen and C. N. J. Wagner, in 'Liquid Metals: Chemistry and Physics', (ed. S. V. Beer) p. 633, Dekker, New York (1972).
169. J. L. Finney, *Nature*, 266 (1977) 309.
170. Y. Waseda, *J. Solid State Phys.*, 12 (1977) 181,
171. P. Chaudhari and D. Turnbull, *Science*, 199 (1978) 11.
172. M. Naka, K. Hashimoto, and T. Masumoto, *J. Japan Inst. Met.*, 38 (1974) 835.
173. *Idem*, *Corrosion*, 32 (1976) 146.
174. K. Hashimoto, M. Naka, and T. Masumoto, *Sci. Rep. Res. Inst. Tohoku Univ.*, A26 (1976) 48.

175. M. Naka, K. Hashimoto, and T. Masumoto, *J. Non-Cryst. Solids*, 28 (1978) 403.
176. T. Masumoto and K. Hashimoto, *Ann. Rev. Mat. Sci.*, 8 (1978) 215.
177. M. Naka, K. Hashimoto, and T. Masumoto, *Sci. Rep. Res. Inst. Tohoku Univ.*, A26 (1977) 283.
178. K. Hashimoto, K. Osada, T. Masumoto, and S. Shimomura, *Science*, 16 (1976) 71.
179. M. Naka, K. Hashimoto, and T. Masumoto, *J. Non-Cryst. Solids*, 29 (1978) 61.
180. K. Hashimoto, M. Naka, K. Asami, and T. Masumoto, *Corrosion*, 19 (1979) 165.
181. T. Egami, P. J. Flanders, and C. D. Graham, *AIP Conf. Proc.*, 24 (1974) 697.
182. R. C. Sherwood, E. M. Gyorgy, H. S. Chen, S. D. Ferris, G. Norman, and H. J. Leamy, *ibid* 24 (1974) 745.
183. H. J. Leamy, S. D. Ferris, G. Norman, D. C. Joy, R. C. Sherwood, E. M. Gyorgy, and H. S. Chen, *Appl. Phys. Lett.*, 26 (1975) 259.
184. E. M. Gyorgy, H. J. Leamy, R. C. Sherwood, and H. S. Chen, *AIP Conf. Proc.*, 29 (1975) 198.
185. E. M. Gyorgy, in 'Metallic Glasses', p. 275, Metals Park, OH: ASM (1978).
186. C. D. Graham and T. Egami, *Ann. Rev. Mat. Sci.* 8 (1978) 423.
187. S. Ohnuma, K. Watanabe, and T. Masumoto, *Phys. Stat. Solidi*, 44 (1977) K-151.
188. H. Fujimori, T. Masumoto, Y. Chi, and M. Kikuchi, *Japan J. Appl. Phys.*, 13 (1974) 1889.
189. R. C. O'Handley, L. I. Mendelsohn, R. Hasegawa, R. Ray, and S. Kavesh, *J. Appl. Phys.*, 47(10) (1976) 4660.
190. T. Mizoguchi, K. Yamaguchi, and H. Miyajima, in 'Amorphous Magnetism', p. 325. Plenum, New York (1973).
191. H. S. Chen, R. C. Sherwood, and E. M. Gyorgy, *IEEE Trans. Magn.*, MAG-13 (1977) 1538.
192. N. S. Kazama, M. Nitera, and T. Masumoto, *Ref. 12*. 164.
193. S. Hatta, T. Egami, and C. D. Graham, Jr., *Appl. Phys. Lett.*, 34 (1979) 113.

194. F. E. Luborsky, J. J. Becker, J. L. Walter, and D. L. Martin, IEEE Trans. Magn., MAG-16 (1980) 521.
195. M. Mitera, T. Masumoto, and N. S. Kazama, J. Appl. Phys., 50(11) (1979) 7609.
196. R. C. O'Handley, C. -P. Chou, and Christofaro, ibid 50(5) (1979) 3603.
197. F. E. Luborsky, J. J. Becker, J. L. Walter, H. H. Liebermann, IEEE Trans. Magn. MAG-15, 3(1979) 1146.
198. S. Hatta, T. Egami, and C. D. Graham, Jr., ibid MAG-14, (1978) 1013.
199. F. E. Luborsky and J.L. Walter, ibid MAG-16, (1980) 572.
200. F. E. Luborsky, H. H. Liebermann, J. J. Becker, and J. L. Walter, Ref. 12. Vol. 2, p. 188.
201. F. E. Luborsky, J. J. Becker, and H. H. Liebermann, Ref. 12. Vol. 2, p. 249.
202. R. Hasegawa, J. Appl. Phys., 52(3) (1981) 1847.
203. K. Inomata, M. Hasegawa, and K. Shimanuki, IEEE Trans. Magn., MAG -17, 6 (1981) 3076.
204. M. Blundell, C. D. Graham, Jr., and K. J. Overshott, J. Magn. Magn. Matls., 19 (1980) 174.
205. M. Blundell and K.J. Overshott, IEEE Trans. Magn., MAG-16, (1980) 1224.
206. R. F. Krause and F. E. Warner, ibid 6 (1981) 2686.
207. H. Fujimori, Y. Obi, T. Masumoto, and H. Saito, Mater. Sci. Eng., 23 (1976) 281.
208. J. W. Shilling, AIP Conf. Proc., 29 (1976) 222.
209. R. C. O'Handley and M. C. Narasimhan, IEEE Trans. Magn., MAG-15, (1979) 970.
210. H. Fujimori, H. Yoshimoto, and H. Morita, ibid 5 (1980) 1227; H. Fujimori, H. Yoshimoto, T. Masumoto, and T. Mitera, J. Appl. Phys., 52(3) (1981) 1893.
211. S. D. Washko, M. L. Osborn, and W. G. Veeraraghaven, J. Appl. Phys., 52(3) (1981) 1899.
212. H. H. Liebermann, C. D. Graham, and P. J. Flanders, IEEE Trans. Magn. MAG-13, 5 (1977) 1541.

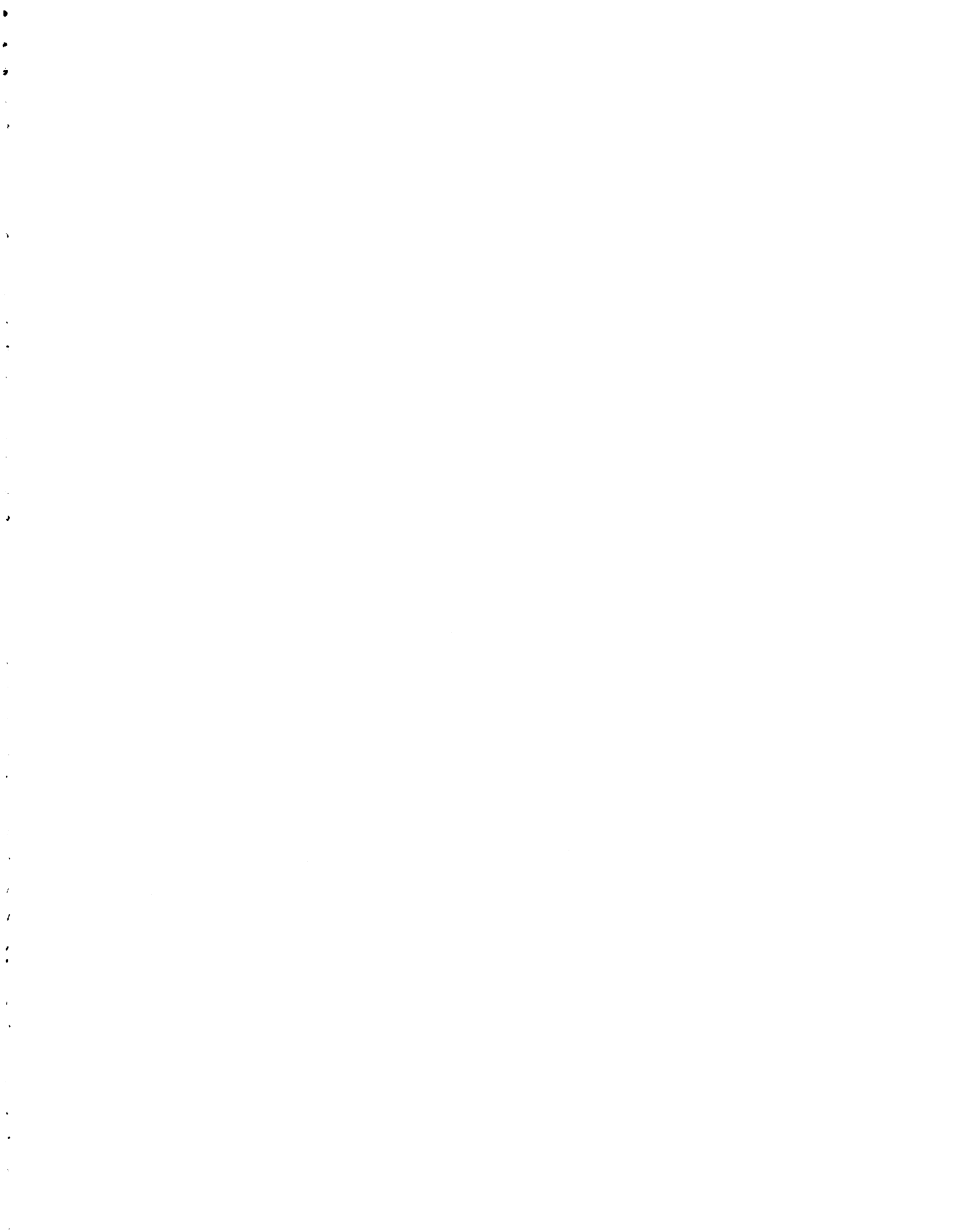
213. F. E. Luborsky, J. L. Walter, and D. G. LeGrand, *ibid* 6 (1976) 930.
214. M. R. J. Gibbs, J. E. Evetts, and N. J. Shah, *J. Appl. Phys.*, 50 (11) (1979) 7642.
215. K. Narita, J. Yamasaki, and H. Fukunaga, *ibid* 50(11) (1979) 7591.
216. N. DeCristofaro, A. Freilich, and G. Fish, *J. Mater. Sci.*, 17 (1982) 2365.
217. C. D. Graham, and T. Egami, *IEEE Trans. Magn.* MAG-15, 6 (1979) 1398.
218. H. J. Leamy, H. S. Chen, and T. T. Wang, *Met. Trans.*, 3 (1972) 699.
219. H. S. Chen, *Scripta Met.*, 7 (1973) 931.
220. C. A. Pampillo and H. S. Chen, *Mater. Sci. Eng.*, 13 (1974) 181.
221. C. A. Pampillo, *J. Mater. Sci.*, 10 (1975) 1194.
222. H. S. Chen and B. K. Park, *Acta Met.*, 21 (1973) 395.
223. H. S. Chen, J. T. Krause, and E. A. Sagety, *J. Non-Cryst. Solids*, 13 (1973/74) 321.
224. R. Ray, B. C. Giessen, C.-P. Chou, and L. A. Davis, *Scripta Met.*, 11 (1977) 973.
225. B. Golding, B. G. Bagley, and F. S. L. Hsu, *Phy. Rev. Lett.*, 29 (1972) 68.
226. E. Orowan, *Proc. 1st National Congress of Appl. Mech.*, p. 453, New York: ASME (1952).
227. D. Weaire, M. F. Ashby, J. Logan, and H. J. Weins, *Acta Met.*, 19 (1971) 779.
228. H. S. Chen, J. T. Krause, and E. Coleman, *J. Non-Cryst. Solids.*, 18 (1975) 157.
229. H. S. Chen, *Mater. Sci. Eng.*, 26 (1976) 79.
230. C.-P. Chou, *Phy. Rev. Lett.*, 37 (1976) 1004.
231. B. S. Berry and W. C. Pritchett, *AIP Conf. Proc.* 34 (1976) 292.
232. H. S. Chen and J. T. Krause, *Scripta Met.*, 11 (1977) 761.
233. K. I. Arai, N. Tsuya, N. Yamada, H. Shirae, H. Fujimori, H. Saito and T. Masumoto, as in Ref. 38. p. 489.

234. H. A. Brooks, *J. Appl. Phys.*, 47 (1976) 344.
235. R. C. O'Handley, R. Hasegawa, R. Ray, and C.-P. Chou, *Appl. Phys. Lett.*, 29 (1976) 330.
236. B. S. Berry and W. C. Pritchett, *ibid* 34 (1975) 1022.
237. B. S. Berry, in 'Metallic Glasses', p. 161, Metals Park, OH: ASM (1978).
238. K. I. Arai and N. Tsuya, *J. Appl. Phys.*, 49 (1978) 1918.
239. C. A. Pampillo and D. E. Polk, *Acta Met.*, 22 (1974) 493.
240. Materials Research Report, Nov. 1975, Allied Chemical Corp.
241. T. Masumoto and H. Kimura, *J. Japan Inst. Metals*.
242. J. J. Gilman, in 'The Science of Hardness Testing & its Research Applications', p. 51, Metals Park, OH: ASM (1973).
243. S. S. Brenner, *J. Appl. Phys.*, 47 (1956) 344.
244. T. Masumoto, *Sci. Rep. Res. Inst. Tohoku Univ.*, A26 (1977) 246.
245. H. S. Chen, *Rep. Prog. Phys.*, 43 (1980) 353.
246. L. A. Davis, *Ref. 38*. p. 369.
247. T. Ogura, T. Masumoto, and K. Fukushima, *Scripta Met.*, 9 (1975) 109.
248. L. A. Davis, *J. Mater. Sci.*, 11 (1976) 711.
249. *Idem*, *ibid* 10 (1975) 1557.
250. D. G. Ast and D. Krenitsky, *Mater. Sci. Eng.*, 23 (1976) 241.
251. H. Kimura and T. Masumoto, *Scripta Met.*, 9 (1975) 211.
252. H. S. Chen and D. Turnbull, *Acta Met.*, 11 (1969) 104.
253. T. Masumoto and M. Koiwa, *J. Japan Inst. Metals*.
254. M. Ura, M. Kitaguchi, E. Fujita, and T. Masumoto, *J. Japan Inst. Metals*.
255. H. S. Chen, *Scripta Met.*, 9 (1975) 411.
256. L. A. Davis, R. Ray, C.-P. Chou, and R. C. O'Handley, *Scripta Met.*, 10 (1976) 541.
257. P. E. Donovan and W. M. Stobbs, *J. Non-Cryst. Solids*, 55 (1983) 61.

258. N. A. Pratten and M. G. Scott, as in Ref. 12, p. 389.
259. H. S. Chen and D. E. Polk, *J. Non-Cryst. Solids*, 15 (1974) 174.
260. A. Inoue, T. Masumoto, S. Arakawa, and T. Iwadachi, as in Ref. 12 p. 265.
261. A. Inoue, T. Masumoto, and H. Kimura, *J. Japan Inst. Metals*, 42 (1978) 303.
262. G. C. Chi, H. S. Chen, and C. E. Miller, *J. Appl. Phys.*, 49(1978) 1915.
263. J. L. Walter, F. Bacon, and F. E. Luborsky, *Mater. Sci. Eng.*, 24 (1976) 239.
264. L. A. Davis and S. Kavesh, *J. Mater. Sci.*, 10 (1975) 453.
265. D. E. Polk and C. A. Pampillo, *Scripta Met.*, 7 (1973) 1161.
266. J. M. Vitek and N. J. Grant, *Metall. Trans.*, 6 (1975) 1472.
267. R. Hill, in 'Mathematical Theory of Plasticity', Oxford (1950).
268. H. S. Chen and T. T. Wang, *J. Appl. Phys.*, 41 (1970) 5338.
269. A. S. Argon, in 'The Inhomogeneity of Plastic Deformation', p. 161, ASM, Ohio (1973).
270. L. A. Davis, *Scripta Met.*, 9 (1975) 339.
271. S. Takayama and R. Maddin, *Metall. Trans.*, 7A (1976) 1065.
272. S. Tomizawa and T. Masumoto, *Sci. Rep. Inst. Tohoku Univ., Sec A*, 26 (1977) 263.
273. C. A. Pampillo, *Scripta Met.*, 6 (1972) 915.
274. A. H. Cottrell, *Phil. Mag.*, 44 (1953) 829.
275. A. I. Taub, *Acta Met.*, 28 (1980) 633.
276. C. A. Pampillo and A. C. Reimschuessel, *J. Mater. Sci.*, 9 (1974) 718.
277. S. Takayama and R. Maddin, *Acta Met.*, 23 (1975) 943.
278. H. S. Chen, H. J. Leamy, and M. J. O'Brien, *Scripta Met.*, 7(1973) 415.
279. A. H. Cottrell, in 'The Mechanical Properties of Matter', p. 322, John Wiley, New York (1964).
280. A. S. Argon, in 'Polymer Materials', p. 411, ASM, Ohio (1975).

281. A. E. H. Love, in 'The Mathematical Theory of Elasticity', p. 221 Dover (1944).
282. D. E. Polk and D. Turnbull, *Acta Met.*, 20 (1972) 493.
283. J. J. Gilman, *J. Appl. Phys.*, 44 (1973) 675.
284. J. C. M. Li, C. A. Pampillo, and L. A. Davis, in 'Deformation and Fracture of High Polymers', (eds. H. H. Kausch, J. A. Hassell and R. I. Jaffe, Plenum, New York (1974)).
285. A. L. Robinson, *Research News; Glassy Metals: No Longer a Laboratory Curiosity*, *Science*, 182 (1973) 908.
286. F. Spaepen and D. Turnbull, *Scripta Met.*, 8 (1974) 563.
287. D. G. Saffman and G. I. Taylor, *Proc. Roy. Soc. London*, A245 (1958) 312.
288. L. A. Davis, in 'Metallic Glasses, p. 191, Metals Park: ASM, Ohio (1978).
289. D. Lee and T. M. Devine, Ref. 38. p. 393.
290. W. C. Leavengood and T. S. Vong, *J. Appl. Phys.*, 31 (1960) 1416.
291. J. C. M. Li, in 'Frontier in Materials Science', p. 527. Dekker, New York (1976).
292. M. F. Ashby and J. Logan, *Scripta Met.*, 7 (1973) 513.
293. F. Spaepen, *Acta Met.*, 25 (1977) 407.
294. P. S. Steif, F. Spaepen, and J. W. Hutchinson, *ibid* 30 (1982) 447
295. A. S. Argon, *ibid* 27 (1979) 47.
296. R. Becker, G. Sepold, and P. L. Ryder, 'Chemistry and Physics of Rapidly Solidified Materials', (ed. B. J. Berkwitz and R. O. Scattergood), TMS-AIME Warrendale (1983).
297. G. A. Jones, S. F. H. Parker, P. J. Grundy, K. J. Overshott, and M. H. Price, *IEEE Trans. Magn. MAG-19*, 5 (1983) 1922.
298. J. A. Leake and A. L. Greer, *J. Non-Cryst. Solids*, 33-39 (1980) 735.
299. J. L. Walter, J. D. Livingstone, and A. M. Davis, *Mater. Sci. Eng.*, 49 (1981) 47.
300. H. N. Ok and A. H. Morrish, *Phy. Rev. B* 23 (1981) 2257.
301. A. L. Greer and J. A. Leake, Ref. 12. p. 299.

302. L. A. Davis, N. DeCristofaro, and C. H. Smith, in Proc. of the Conf. on Metallic Glasses, p. 1, Science and Technology, Budapest (1980).
303. H. N. Ok and A. H. Morrish, J. Phys. F, Metal Phys., 11 (1981) 1495.
304. P. Duwez, Ann. Rev. Mater. Sci., 6 (1976) 83.
305. S. Takayama, J. Mater. Sci., 11 (1976) 164.
306. R. M. White, J. Appl. Phys., 34 (1964) 2123.
307. P. E. Donovan and W. M. Stobbs, Acta Met., 31 (1983) 1.
308. J. L. Walter and F. E. Luborsky, Mater. Sci. Eng., 33 (1981) 91.
309. J. K. Knowles and E. Sternburg, J. Elasticity, 10(1) (1980) 81.
310. Idem, *ibid*, 11(2) (1981) 129.
311. R. Abeyaratne, *ibid* 11(4) (1981) 373.



MICHIGAN STATE UNIVERSITY LIBRARIES



3 1293 03177 8206